

# CANADIAN THESES ON MICROFICHE

## THÈSES CANADIENNES SUR MICROFICHE



National Library of Canada  
Collections Development Branch

Canadian Theses on  
Microfiche Service

Ottawa, Canada  
K1A 0N4

Bibliothèque nationale du Canada  
Direction du développement des collections

Service des thèses canadiennes  
sur microfiche

### NOTICE

The quality of this microfiche is heavily dependent upon the quality of the original thesis submitted for microfilming. Every effort has been made to ensure the highest quality of reproduction possible.

If pages are missing, contact the university which granted the degree.

Some pages may have indistinct print especially if the original pages were typed with a poor typewriter ribbon or if the university sent us an inferior photocopy.

Previously copyrighted materials (journal articles, published tests, etc.) are not filmed.

Reproduction in full or in part of this film is governed by the Canadian Copyright Act, R.S.C. 1970, c. C-30. Please read the authorization forms which accompany this thesis.

THIS DISSERTATION  
HAS BEEN MICROFILMED  
EXACTLY AS RECEIVED

### AVIS

La qualité de cette microfiche dépend grandement de la qualité de la thèse soumise au microfilimage. Nous avons tout fait pour assurer une qualité supérieure de reproduction.

S'il manque des pages, veuillez communiquer avec l'université qui a conféré le grade.

La qualité d'impression de certaines pages peut laisser à désirer, surtout si les pages originales ont été dactylographiées à l'aide d'un ruban usé ou si l'université nous a fait parvenir une photocopie de qualité inférieure.

Les documents qui font déjà l'objet d'un droit d'auteur (articles de revue, examens publiés, etc.) ne sont pas microfilmés.

La reproduction, même partielle, de ce microfilm est soumise à la Loi canadienne sur le droit d'auteur, SRC 1970, c. C-30. Veuillez prendre connaissance des formules d'autorisation qui accompagnent cette thèse.

LA THÈSE A ÉTÉ  
MICROFILMÉE TELLE QUE  
NOUS L'AVONS REÇUE

Canada



National Library of Canada

Bibliothèque nationale du Canada

D-315-19545-2

Canadian Theses Division

Division des thèses canadiennes

Ottawa, Canada  
K1A 0N4

67453

### PERMISSION TO MICROFILM — AUTORISATION DE MICROFILMER

• Please print or type — Écrire en lettres moulées ou dactylographier

Full Name of Author — Nom complet de l'auteur

ADRIANO ZENARI

Date of Birth — Date de naissance

May 2 1943

Country of Birth — Lieu de naissance

ITALY

Permanent Address — Résidence fixe

1144 77 AVE

EDMONTON T6G 0L8

Title of Thesis — Titre de la thèse

NUCLEAR MEDICINE TOMOGRAPHY WITH SPECIAL  
REFERENCE TO THE PHO/CON MULTIPLANE IMAGER

University — Université

UNIVERSITY OF ALBERTA

Degree for which thesis was presented — Grade pour lequel cette thèse fut présentée

DOCTOR OF PHILOSOPHY

Year this degree conferred — Année d'obtention de ce grade

Name of Supervisor — Nom du directeur de thèse

J. W. SCRIMGER

Permission is hereby granted to the NATIONAL LIBRARY OF CANADA to microfilm this thesis and to lend or sell copies of the film.

The author reserves other publication rights, and neither the thesis nor extensive extracts from it may be printed or otherwise reproduced without the author's written permission.

L'autorisation est, par la présente, accordée à la BIBLIOTHÈQUE NATIONALE DU CANADA de microfilmer cette thèse et de prêter ou de vendre des exemplaires du film.

L'auteur se réserve les autres droits de publication; ni la thèse ni de longs extraits de celle-ci ne doivent être imprimés ou autrement reproduits sans l'autorisation écrite de l'auteur.

Date

August 5 1983

Signature

THE UNIVERSITY OF ALBERTA

NUCLEAR MEDICINE TOMOGRAPHY WITH SPECIAL REFERENCE TO THE  
PHO/CON MULTIPLANE IMAGER

by

C

ADRIANO ZENARI

A THESIS

SUBMITTED TO THE FACULTY OF GRADUATE STUDIES AND RESEARCH  
IN PARTIAL FULFILMENT OF THE REQUIREMENTS FOR THE DEGREE  
OF DOCTOR OF PHILOSOPHY

DEPARTMENT OF PHYSICS

EDMONTON, ALBERTA

FALL 1983

THE UNIVERSITY OF ALBERTA

RELEASE FORM

NAME OF AUTHOR ADRIANO ZENARI

TITLE OF THESIS NUCLEAR MEDICINE TOMOGRAPHY WITH SPECIAL  
REFERENCE TO THE PHO/CON MULTIPLANE IMAGER

DEGREE FOR WHICH THESIS WAS PRESENTED DOCTOR OF PHILOSOPHY

YEAR THIS DEGREE GRANTED 1983

Permission is hereby granted to THE UNIVERSITY OF ALBERTA LIBRARY to produce single copies of this thesis and to lend or sell such copies for private, scholarly or scientific research purposes only.

The author reserves other publication rights, and neither the thesis nor extensive extracts from it may be printed or otherwise reproduced without the author's written permission.

(signed)

*Adriano Zenari*

PERMANENT ADDRESS:

11414 77 AVENUE

EDMONTON, ALBERTA

CANADA. T6G 0L8

DATED July 15 1983



THE UNIVERSITY OF ALBERTA  
FACULTY OF GRADUATE STUDIES AND RESEARCH

The undersigned certify that they have read, and  
recommend to the Faculty of Graduate Studies and Research,  
for acceptance, a thesis entitled

NUCLEAR MEDICINE TOMOGRAPHY WITH SPECIAL  
REFERENCE TO THE PHO/CAN MULTIPLANE IMAGER

Submitted by Adriano Zenari

in partial fulfillment of the requirements for the degree of  
Doctor of Philosophy

in Medical Physics

R. F. Egerton

John Scriniger  
Supervisor

Douglas M. Shepard

H. Richard Kays

Tom H. Jamington

Jim Peters

External Examiner

Date: 14 July 1983

to my wife and children

iv

## ABSTRACT

The Pho/Con is a dual Anger camera multiplane tomographic scanner, capable of producing longitudinal tomograms through the subject.

The physical characteristics of the component of this imaging device have been investigated in the operation of the gamma camera from the system. Measurements performed on the detector include the study of uniformity, linearity, intrinsic spatial resolution, energy and temporal resolution. The system characteristics have been studied with a view to establishing the influence of the subcomponents of the detector on the overall performance. Experimental measurements have been made using both analogue and computerized reconstruction techniques.

Techniques which attempt to remove blur artefacts from images produced by limited angle tomographic systems are briefly reviewed. A new iterative approach of deblurring Pho/Con images is also presented. Deblurring studies with a computer simulated noiseless phantom and a simulated phantom with uncorrelated noise are presented. The algorithm was also tested with images of a true phantom obtained by a simple back-projection reconstruction of Pho/Con data. Results for images with three different statistical counts are presented.

## ACKNOWLEDGMENT

I am indebted to a number of persons who assisted and helped me throughout this project.

In particular I would like to thank both my supervisors, Drs. J.W. Scrimger and D. Sheppard for their continuous support and encouragement. Both were always at hand to discuss many aspects of this project. A special thanks to Dr. J.W. Scrimger for the many suggestions made about the experimental work and for the time He spent in discussing and reviewing the manuscript.

I am grateful to Dr. R.H. Hooper who provided me with much needed assistance in the digital acquisition and processing of the Pho/Con data. He also donated his time and expertise in writing the software necessary to display Pho/Con images on the GAMMA-11 system.

I wish to forward my appreciation to Mr. N. Osborne who made available to me the FFT program, hence greatly simplifying the implementation of the deblurring algorithm. I would like to thank also Mr. L. Stenger for the prompt machine work in constructing many of the test phantoms.

## TABLE OF CONTENTS

1.1	An overview of medical imaging . . . . .	21
1.2	Nuclear medical imaging . . . . .	31
1.3	Physics in nuclear medicine . . . . .	38
1.3.1	2-Dimensional imaging devices . . . . .	39
1.3.2	3-Dimensional imaging . . . . .	46
1.3.3	4-Dimensional imaging . . . . .	51
1.4	Summary . . . . .	52
2.1	Tomography in nuclear medicine . . . . .	54
2.2	Pho/Con tomographic scanner . . . . .	57
2.2.1	Scanner: Principle of operation . . . . .	60
2.2.2	Gamma camera . . . . .	61
2.3	Pho/Con: Principle of operation . . . . .	63
3.1	Pho/Con: System components . . . . .	78
3.2	Collimators . . . . .	79
3.2.1	Sensitivity . . . . .	80
3.1.1	Resolution . . . . .	83
3.2	Gamma camera . . . . .	94
3.2.1	Spatial linearity . . . . .	97
3.2.2	Uniformity . . . . .	100
3.2.3	Resolution . . . . .	105
3.3	System performance . . . . .	115
3.3.1	System uniformity . . . . .	117
3.3.2	System linearity . . . . .	117
3.3.3	System resolution . . . . .	121
4.1	Focal plane tomography and the limited-sampling-angle technique. . . . .	131

4.1.1	Pho/Con interface to a Dec .11/70 computer	. 135
4.2	Single back projection: Pho/Con reconstruction algorithm	. . . . . 137
4.2.1	3-Dimensional reconstruction for limited-angle sampling	. . . . . 140
4.3	Iterative deblurring with pixel refinement of a first estimate	. . . . . 151
5.1	Deblurring with a computer simulated noiseless phantom	. . . . . 156
5.2	Performance of the deblurring algorithm in the presence of noise	. . . . . 161
5.2.1	Deblurring of computer simulated phantom with noise	. . . . . 168
5.2.2	Deblurring phantom images with correlated noise	. . . . . 173
6.1	Conclusion And Discussion	. . . . . 179
6.2	Deblurring algorithm: a critique	. . . . . 192

# LIST OF TABLES

Table	Description	Page
I	Electromagnetic Range of Medical Imaging Devices	1
II	Radiopharmaceutical Labelled with Single Photon Emitters	14
III	Radiopharmaceutical Labelled with Positron Emitters	15
IV	Pho/Con collimators: Physical Characteristics	61
V	Tomographic Systems in Nuclear Medicine: A Comparison	161

# LIST OF FIGURES

Figure	Page
1.1 Simplified diagram of a rectilinear scanner. ....	20
1.2 Basic components of an Anger gamma camera. ....	24
2.1 Photograph of Pho/Con system showing the scanning heads, control console and microdot imager. ....	38
2.2 Schematic diagram of one probe of the Pho/Con multiplane longitudinal scanner. ....	39
2.3 Simplified schematic diagram of 7-PM tube Anger camera with positioning signals. ....	42
2.4 Pho/Con upper and lower focussed collimators showing the 12 longitudinal readout planes and the location of the geometrical focal plane. ....	44
2.5 Transmission image of a bar phantom with pattern spacing of 3.18, 4.76, 6.35, 9.52 mm obtained with a) normal collimator, and b) minimum acceptance angle aperture of $48^\circ$ . ...	46
2.6 Schematic diagram of the point source detector configuration showing the Pho/Con principle of operation. The diagram shows the irradiated	



	area of the crystal relative to the detector-	
	source position, .....	48
2.7	One dimensional Pho/Con readout for plane A	
	a source in plane A, .....	53
2.8	Pho/Con Imaging of a source out of plane by	
	applying the plane A arithmetic, .....	54
2.9	Image of a 2 mm diameter Co-57 point source	
	obtained with the system microdet imager, .....	56
3.1	Simplified diagram of a focussed multichannel	
	collimator showing the parameters of interest;	
	the central entrance hole, of diameter $d_1$ , and	
	at exit $d_2$ , the focal length $F$ , and the colli-	
	mator thickness $L$ , .....	62
3.2	Schematic arrangement used to measure the iso-	
	response curve of the Pho/Con collimator.	
	The point source is moved along predetermined	
	longitudinal response lines yielding the	
	lateral response curves, .....	65
3.3	Longitudinal response to a point source, in	
	air, displaced along the collimator axis. The	
	curve is characteristic of the 380 KeV 10 mm	
	resolution focussed collimator, .....	66
3.4	Lateral response to a point source in air for	

the 380 KeV 10 mm resolution Pho/Con collimator.  
These curves were obtained with the source  
positioned within the focal depth. .... 67

3.5 Isocount contour, in air, for the 150 KeV 10 mm  
resolution focussed collimator. The curves,  
starting from the outer one, are: 10, 15, 20,  
30, 40, 50, 60, 70, 80, 90% of the maximum  
count rate measured at the focal point. .... 68

3.6 Isocount contour, in air, for the 380 KeV 10 mm  
resolution focussed collimator. The curves,  
starting from the outer one, are: 10, 15, 20,  
30, 40, 50, 60, 70, 80, 90% of the maximum  
count rate. .... 69

3.7 Isocount contour for 380 KeV, 10 mm resolution  
focussed collimator measured with the source in  
water. The isoresponse curves are 15, 10, 30,  
40, 50, 60, 70, 80, 90% of maximum count. .... 71

3.8 Isocount contour for the 380 KeV, 10 mm  
resolution focussed collimator corrected for  
attenuation. The plotted isoresponse curves  
are 15, 10, 30, 40, 50, 60, 70, 80, 90% of  
maximum count rate. .... 72

3.9 Calculated resolution parameters for the  
Pho/Con medium energy focussed collimator as a

function of source-to-collimator distance.

$R_o^2 = r_c^2 + r_p^2 + r_e^2$  represents the total resolution,  $r_c$  the channel component and  $r_p$  the collimator parallax contribution.  $r_e$  is the resolution component due to the crystal resolving distance. The data points are measured values for  $R_o$ . ..... 75

3.10 Pho/Con probe spatial linearity expressed in MCA channel number and measured at angles varying from  $0^\circ$  to  $180^\circ$ . The curves shown were obtained using the camera x-position signal by moving the source along lines through the camera geometrical center as indicated in the insert. .... 78

3.11 Pho/Con camera spatial linearity measured with the y-position signal adopting the same procedure of Figure 3.10. .... 79

3.12 Linearity of x-position signal measured at angles  $0^\circ$ ,  $30^\circ$ ,  $60^\circ$ ,  $120^\circ$ ,  $150^\circ$  relative to the camera x-coordinate axis. The solid line represents the least square fit to the measured MCA peak position in cm. .... 81

3.13 Linearity of y-position signal measured at angles of  $0^\circ$ ,  $30^\circ$ ,  $60^\circ$ ,  $120^\circ$ ,  $150^\circ$  with respect to the camera y-coordinate axis. .... 82

3.14 Pho/Con detector flood field (a) with collimator, (b) without collimator. ....	84
3.15 x and y count profiles through the center of the Pho/Con Anger camera. ....	86
3.16 Intrinsic resolution profile for a Pho/Con detector calculated from the FWHM of the point spread function. ....	88
3.17 Ratio of the number of events detected in a preset energy window to the total number of count in the energy spectrum. a) T -99 mm (140 KeV) in air, b) Cr-51 (320 KeV) in air. c) and d) are the respective curves in 10 cm of scattering material. ....	91
3.18 Pho/Con count losses measured with the 15 (●) and 25% (+) of the analyzer window. The straight line represents zero count losses. ....	94
3.19 System uniformity obtained by scanning a Co-57 flood source.. Image of the flood obtained with the microdot imager. ....	98
3.20 Analogue images of an orthogonal test pattern obtained by scanning the source with a 25 cm x 25 cm maximum scan area. (a) Image of the pattern in the first focal plane and (b) with the pattern in the third focal	

plane. ....	100
3.21 Computer reconstructed orthogonal test pattern for the first and third readout planes. Circles indicate system reconstructed locations of points. ....	102
3.22 Analogue images of a line source at 45 degrees relative to the detector axis together with the corresponding density profiles of the six readout planes. ....	105
3.23 <del>P</del> resolution as a function of source distance from the collimator for low, medium and high energy collimators. The solid lines are the calculated values for (a) the 550 KeV and (b) the 150 KeV and 380 KeV. ....	106
3.24 Normalized x, y, and z profiles of a Co-57 point source obtained with a simple back projection reconstruction algorithm. ....	108
3.25 Representation of the resolution along the Z axis. ....	109
3.26 System resolution measured with the 150 KeV collimator. (a) calculated resolution with $r_p=0$ , (b) computer data obtained imaging a Co-57 point source, (c) resolution measured using density profiles of analogue images	

of the line at  $45^\circ$ . . . . . 110

4.1 Characteristic blur pattern produced by  
the Pho/Con and obtained by imaging a line  
source at  $45^\circ$  with respect to the collimator  
central axis. . . . . 114

4.2 Spatial localization of an event  
originating at P. Pho/Con detector  
coordinates  $(X_c, Y_c, Z_c = 0)$  and the point  
of interaction in the crystal  $(X, Y, Z = 0)$   
are measured relative to the origin of the  
scan  $(0, 0, 0)$ . D is the vertical distance  
of P from the focal plane, and H represents  
the sum of the collimator thickness and  
focal depth. . . . . 118

4.3 Flow chart of the deblurring algorithm. . . . . 135

5.1 Phantom image planes showing the intensity  
levels 0, 1, and 2. . . . . 138

5.2 Image planes 13 through 20 of the phantom as  
displayed by the Gamma-11 system. . . . . 139

5.3 Blurred image planes 9 to 24 scaled to the  
maximum pixel count in the set of images. . . . . 139

5.4 Change in the DFSQ value showing the convergence  
of the algorithm in the deblurring of noiseless

images.....	140
5.5 Initial estimate of the blurred image for planes 9 through 24.....	142
5.6 Estimate after 5 iterations.....	142
5.7 Estimate after 10 iterations.....	143
5.8 Refined initial estimate after 20 iterations.....	143
5.9 Images of planes 9 through 26 after 10 iterations using an initial estimate with .25 lower level cut off.....	144
5.10 Images of planes 9 through 26 after 10 iterations with a threshold of .35.....	144
5.11 Convergence of the algorithm for the threshold values (•) 0.25, (+) 0.3, and (■) 0.35.....	145
5.12 Simplified diagram of the real phantom used to test the deblurring routine. The graph shows dimensions and relative position of the two cylinders.....	148
5.13 Convergence of the DFSQ value for the blurred images of the computer simulated phantom with statistical count error of (a) 10%, (b) 3%, (c) 1%, and (d) no error.....	150
5.14 Image of plane 17 of the computer simulation of	

phantom with varying uncorrelated statistical noise. 10% count statistics	
a) initial estimate	
b) image after 4 iterations; 3% count statistics,	
c) initial estimate, d) image after 10 iterations;	
1% count statistics, e) initial estimate,	
f) image after 10 iterations. ....	151
 5.15 Change in the DFSQ value for images of the real phantom with maximum pixel count of (a) 1560 counts, (b) 698 counts, and (c) 327 counts. ....	154
 5.16 Images of planes 7 through 22 of the test phantom with maximum pixel count of 327, a) initial estimates b) images after 5 iterations. ....	155
 5.17 Images of planes 7 through 22 of the test phantom with maximum pixel count of 698, a) initial estimates b) images after 6 iterations. ....	156
 5.18 Images of planes 7 through 22 of the test phantom with maximum pixel count of 1560, a) initial estimates b) images after 6 iterations. ....	157
 6.1 Point source response as a function of distance from the collimator (380 KeV), measured with a minimum acceptance angle of $0^\circ$ , $17.8^\circ$ , $27.8^\circ$ , $41.8^\circ$ , $54.6^\circ$ beginning with the outer curve. ....	168



6.2 Gain in the depth resolution obtained by  
confining the acceptance angle to a minimum  
of  $0^\circ$ ,  $17.8^\circ$ ,  $27.8^\circ$ ,  $41.8^\circ$ ,  $54.6^\circ$ . The same  
graph shows the loss of count at the same  
angles. .... 169

## CHAPTER 1

### 1.1 An overview of medical imaging

The main objective of imaging in medicine is a non invasive visualization of the internal structure or function of the human body which would facilitate the diagnosis of disease. The physical principles behind many present imaging techniques involve some portion of the electromagnetic spectrum. The most notable exception is ultrasonic imaging which utilizes transmitted and reflected sound waves to reveal the internal structures. The table shown below attempts to summarize some of the better known imaging modalities and the place which they occupy within the electromagnetic spectrum.

Table I : Electromagnetic Range of Medical Imaging Devices

Electromagnetic Spectrum (meter)	Techniques
$10^{-13}$ - $10^{-10}$ $\gamma$ -rays	a) Planar radioisotope imaging b) Emission tomography (PET, SPECT) c) Focal plane tomography
$10^{-11}$ - $10^{-8}$ x-rays	a) Conventional radiography b) Computed tomography c) Digital radiography
$10^{-6}$ - $10^{-3}$ Infrared	Thermography
$10^{-3}$ - $10^{-1}$ Microwave	Some experimental work (Rao et al 1980, Larsen et al 1980)
$1.0$ - $10^3$ Radio	Nuclear Magnetic Resonance imaging

Since the discovery of x-rays on November 8, 1895 and the attainment of the first image of a living human hand on December 21, 1895 by the German physicist Wilhelm Conrad Rontgen (Glasser O., 1934) the use of penetrating radiation as a means of revealing internal structures of the human body has become a common clinical procedure in the diagnosis of diseases. The realization of the diagnostic and therapeutic potential of x-rays quickly established new disciplines, within the medical practice, which would incorporate techniques employing x-rays for the diagnosis or treatment of diseases.

The application of radioactive indicators for the study of living systems was first proposed by the chemist G. Hevesy in the early twenties (Myers et al 1975). He postulated that the radioactivity would not affect the biological behavior of the tracer. For his early work in biological tracing techniques he received the Nobel prize in 1943.

Following the construction of the first few nuclear reactors (at Oak Ridge and Brookhaven national laboratories) in the early forties the list of radioactive isotopes available for medical purposes grew considerably. Radiology then became the science in medicine which would make use of any form of ionizing radiation for the diagnosis and treatment of diseases. Within such a discipline ionizing radiation became the predominant diagnostic procedure, because of its ability to penetrate the human body allowing one to see deep seated structures. It is for this reason

that x-ray technology became a popular and powerful diagnostic tool.

The use of isotope imaging in medicine was introduced later, following the discovery that certain isotopes of stable nuclei emitted some form of radiation. The use of isotopes was also delayed because of the lack of knowledge about the principle of radiotracer uptake by the various organs in the human body.

The recent discovery of transmission computed tomography has elevated imaging employing ionizing radiation to a level of sophistication never before encountered in any imaging technique. Computed tomography was the result of advances in computer technology and the application of new reconstruction techniques to imaging by the work of Oldendorf (1961), Kuhl and Edwards (1963), and Cormack (1963, 1964). This initial impulse culminated in the development of the first commercial transmission computerized tomographic system by Hounsfield in 1972. For their contribution to the development of computerized tomography Cormack and Hounsfield received the Nobel Prize for Physiology and Medicine in 1979.

Comparison between x-ray and radioisotope imaging techniques reveal both similarities and differences. They are similar in that both methods use ionizing radiation as a means to acquire information about the object under investigation. However both traditional x-ray imaging and transmission CT produce images which describe some morphological patterns of the object under investigation.

On the other hand, radioisotope imaging produces patterns which are physiological, biological and biochemical in nature since it describes a function specific to a given anatomical structure. A more detailed discussion of nuclear medicine imaging techniques is deferred until a later section.

The problem associated with conventional radiography, aside from the superimposition of surrounding structures on the desired image, was the lack of soft tissue differentiation. Transmission CT can successfully provide detailed pictures, for example, of the head by producing clear images of cerebral ventricles and subarachnoidal cavities. In imaging the soft tissue with CT it is now possible to visualize the spinal cord. In the larger section of the body the lungs, heart, kidneys, liver, pancreas, are easily identified, allowing a correlation with a priori knowledge of the anatomy. In addition, it has simplified the diagnostic identification of abnormal morphological and pathological conditions in internal organs replacing more traumatic and costly procedures.

Since its introduction, CT has gone through a considerable technological development in construction of x-ray tubes, detector system and gantry motion. These technical advances were paralleled by the improvement of the algorithms for the tomographic reconstruction (Bracewell et al 1967, Bates et al 1971, Ramachandran et al 1971, Shepp et al 1974). Early CT scanners utilized a highly collimated single pencil beam of x-ray and scintillators and were

57

characterized by the translate and rotate motion. Early limitations associated with these devices were the blurring in the image due to the physical and physiological movement associated with the patients resulting from lengthy imaging time (Ledley, R.S., 1974). The high collimation of source-detector configuration allowed one to measure the absorption in tissue practically uncontaminated by scattered x-rays thus resulting in good tissue discrimination. To speed up the imaging time to a fraction of a second the x-ray beam was later modified to yield a fan beam geometry by employing an array of detectors (Sagel S. 1976). The movement of the source-detector was again translation-rotation. By widening the x-ray fan angle to cover the complete cross section of the patient it became possible to eliminate the translation motion. Rotation over 360 degrees of the fan beam was sufficient for the reconstruction of a CT image. Two possible machine configurations emerged, one in which the x-ray source and detector rotate around 360 degrees as a unit, while in the second case the x-ray source rotates within a ring of stationary detectors (Huang et al, 1979).

While imaging employing ionizing radiation was to undergo such a radical change both in concept and in instrumentation other modalities employing different physical phenomena were being used or investigated. Some of the physical principles, such as thermography, were well known in the practice of medicine. Others such as ultrasound, were struggling to establish themselves as

possible diagnostic tools. Of very recent development (and of great potential) are imaging techniques employing nuclear magnetic resonance. Systems of this type are now being tested in some medical centers.

Medical thermography preceded the development and use of radiation for medical diagnosis. Wunderlich started to monitor the body temperature in hospitalized patients in 1851. As a result of his work, it was recognized that the temperature of the body could be used as a symptom in establishing the presence of disease in the human body. Some early attempts to measure the body surface temperature variation, however, were unsuccessful due to the lack of knowledge of the complex thermodynamic balance in the human body.

Infra-red radiation discovered by Sir William Herschel was then used to produce the first "thermograph". This was achieved by exposing paper coated with soot and impregnated with alcohol to infrared radiation, causing the irradiated area to appear lighter.

The first clinical thermograph was made in 1956 by Lawson, a Canadian surgeon, showing that carcinoma of the breast was characterized by an increase in the breast surface temperature. Although additional reports about the detection and monitoring of disease using thermography were presented, the main application is still confined to the screening of the breast for the early detection of lesions. Although thermography does not expose the patient to the danger of ionizing radiation, it has been unable to

establish itself as an independent diagnostic technique for the detection of breast malignancy. In fact the screening of breast is normally done in conjunction with physical examination and mammography. The nonspecificity and lack of sensitivity of current instrumentation has limited the present application of thermography in medicine. However, current trends which use computer image processing could enhance its usefulness (Cronin 1977).

Microwave imaging has been employed only recently to monitor changes in the water level in the lungs (Bragg et al, 1977). Methods of imaging biological specimens have also been attempted recently (Larsen et al, 1980). In these techniques the images are displayed as a spatial variation of the magnitude of the transmitted scattering parameter, which is a complex quantity representing the loss in amplitude and phase of the signal between the transmitting and receiving antennas. Tomography was also investigated (Rao et al, 1980) using a system equivalent to a rotate translate CT scanner.

The most recent method developed for imaging internal structures of the body is nuclear magnetic resonance (NMR), operating in the radio frequency range of the electromagnetic spectrum. The idea of NMR in imaging medicine was first introduced by Damadian in 1971 for the detection of tumors. Lauterbur in 1973 produced the first 2-dimensional phantom images using a reconstruction technique similar to the back projection reconstruction employed in x-ray CT. The potential of obtaining tomographic images



without any apparent risk (relative to the known risk of ionizing radiation) has made NMR an imaging method of major interest. NMR images describe chemical and metabolic interaction within the reconstructed section, allowing one therefore to monitor changes at the molecular level. The added appeal of NMR is the non-ionizing and non-invasive nature of the technique and the ability to penetrate bone structure without loss of signal.

NMR imaging has been used for many years in physics and particularly in chemistry for the investigation of molecular structure. Aside from more stringent instrumentation requirements in medical imaging, the principles of signal production and detection remain essentially the same.

The common target in the reconstruction process are the atomic nuclei. These exhibit two important physical properties, namely angular momentum (spin) and magnetic moment. The magnetic moment represents the magnitude and direction of the magnetic field surrounding the nuclei, and consequently they can act as small magnets. When the nuclei are placed in a static magnetic field these tiny magnetic dipoles will tend to align themselves, some parallel and some antiparallel, to the applied external field, precessing at a characteristic frequency called the Larmor frequency. If a radiofrequency (RF) field of the same frequency is applied at 90 degrees with respect to the external field, the nuclei will absorb the RF energy causing the magnetic moment to precess in a plane perpendicular or antiparallel to the magnetic field. The precessing by these elemental

dipoles induces in the RF sensing coil an electromotive force which represents the NMR signal. The intensity of the signal depends on the transverse relaxation time  $T_2$  and the time that the dipole takes to decay and return to equilibrium called the spin lattice relaxation time  $T_1$ , (Andrew E. R. 1979, Partain et al, 1981). In order to produce images using the NMR signals it is necessary to apply a linear field gradient along a desired direction. Let us assume, for a moment, that two equal samples are placed in a uniform field. Following the RF pulse, the two samples will decay with the same frequency thus preventing the separation of the signals associated with each sample. However, in a varying field configuration, the two sample volumes placed at different locations in the field will resonate at different frequencies. The signals produced by the two samples as a result of the free induction decay will be the superposition of the frequencies which can then be separated using Fourier techniques.

Ultrasonic imaging has provided a viable alternative to conventional radiography in the imaging of the abdomen where the majority of the organs have approximately the same tissue density. Ultrasonography, as opposed to radiation imaging modalities, uses sound wave propagation in the body to outline various structures. In ultrasonic imaging, the location of objects within a medium are obtained by mapping the time interval between the emitted ultrasound wave and the received echo produced at the object boundaries.

The device generating and receiving the sound wave is a

transducer which exhibits piezoelectric properties. The piezoelectric phenomena, discovered in 1880 by Pierre and Jacques Curie, is the property of some crystals (made of dipoles bound in the crystalline structure) to emit sonic waves. These waves are produced by the vibrating dipole following the application of a pulsed electric field. The detection of the reflected signal operates on the inverse of the piezoelectric effect in which the vibration of the dipole in the lattice creates a voltage difference between the surface of the crystal transforming mechanical energy into an electrical signal. Ultrasonic images are produced using the time separation between the transmitted signal and the backscattered wave. The time delay which depends on the depth of the scattering surface is used to reproduce the information using any of the following methods: amplitude (A-mode), brightness (B-mode), real-time, and motion (M-mode) display modes.

The advantages of the sonographic study involving the two dimensional echo images is that for 99.9% of the study time the transducer is detecting echoes following the sonic pulses (James et al 1981). This reduces the damage caused by isonation. The dose can be considerably higher for those techniques which employ higher pulse repetition rates. At present there is limited information about the biological damage produced by employing these latter methods. In the case of the doppler technique, when applied to measure the fetal heart rate, the exposure to continuous, low intensity insonation can result in fetal abnormalities or morbidity

(James et al 1981).

Of the imaging modalities just described, it appears that for the near future those using ionizing radiation will remain the methods of choice. This is due partly to the limitation of ultrasonic imaging to penetrate bone structures, and in the case of NMR, because of the required development time to achieve resolution comparable to x-ray CT. Nuclear medicine diagnosis remains a viable procedure for many functional studies since, by applying the principle of tracer kinetics, it can assess the physiological and biochemical function of the various body components in isolation from the surrounding anatomical structures.

## 1.2 Nuclear medical imaging

The importance of the nuclear medicine approach to imaging has been recognized since the early tracer work of Hevesy (1948) where isotopes were employed to study biological functions of living systems. Chiewitz and Hevesy in 1935 measured the phosphorus uptake by tissue and organs in rats by feeding the animals a mixture of sodium phosphate labelled with P-32. Hevesy's conclusion that the radioactivity in the tracer will not affect its biological behaviour remains the basis of present nuclear medicine methodology. This concept is now applied to radioisotopes which replace the stable element in the study of biological systems. Modern nuclear medicine became a reality when the

transmutation of elements was made possible following the construction of nuclear reactors. The net result was a large number of isotopes being available for commercial distribution. The improved reactor technology together with particle accelerators such as the cyclotron has increased considerably the list of isotopes presently available for diagnostic and therapeutic use. This list includes cyclotron produced isotopes of elements considered physiologically important such as C-11, O-15, N-13 and F-18.

The most important isotope presently employed in nuclear medicine imaging is Tc-99m which was discovered in 1938 by Seaborg and Segré (Myers et al 1975). Tc-99m is an artificial element and therefore not a component of biological systems. Nevertheless, because of the short half life (6 hr) and the 140 Kev photon energy it has become the most useful isotope in nuclear medicine. Presently, Tc-99m used in a nuclear medicine environment is almost exclusively obtained from commercial generator systems.

Isotopes used in the past in Nuclear Medicine such as P-32, Au-198, Co-57, Fe-55 and others with long biological half lives have been replaced by new isotopes with a shorter half life in order to minimize the radiation damage to the subject. A list of isotopes presently used in Nuclear Medicine together with their pharmaceutical and physiological applications is given in Table II (Kereiakes et al 1980, Robertson J. S. 1982). The list might not exhaust all the labelled pharmaceuticals now in use since the number is constantly increasing in an effort to produce

radiopharmaceuticals with higher differential uptake in the various target organs. In Table III are listed isotopes which are of relatively recent application in nuclear medicine (Bading J. R. 1983). These are cyclotron produced, neutron deficient isotopes (C-11, O-15, N-13) of elements which make up biological matter. Such isotopes are positron emitters and can be used to study brain functions and metabolism at rest and under the influence of external stimuli (Lenzi et al 1978, Alavi et al 1981, Phelps M.E. 1981). Radiopharmaceuticals labelled with these new positron emitters have also opened new areas of research and clinical application in neurology and cardiology (Hoffman et al 1977, Knust et al 1979, Goldstein et al 1980, Budinger et al 1982). The most important decision in selecting a particular type of pharmaceutical can be broadly classified in the following way (Kereiakes et al 1980):

- a) the degree of target to non target uptake and release
- b) the compatibility of the detection system with the particular radiation energy of the labelling isotope.

The obvious outcome of point a) is a better signal to noise ratio (or signal to background ratio) which favors a reduction in the quantity of administered radiopharmaceutical and therefore a decrease in the dose delivered to the subject. Since radiopharmaceuticals with

TABLE II : Radiopharmaceutical Labelled with Single Photon Emitters

isotope	labelled pharmaceutical	study target organ
Cr-51	sodium chromate	whole body
Ga-67	citrate	spleen
		tumor
Se-75	selenomethionine	infection
Tc-99m	pertechnetate  HSA polyphosphates DTPA  HIDA MAA albumine macrosphere glucoheptonate  sulfur colloid  pyrophosphate RBC  MDP iron complex DTPA colloid	pancreas
		brain
		heart
		stomach
		gonad
		thyroid
		blood
		skeleton
		kidney
		bladder
		liver
		lungs
		lungs
		kidney
		brain
		bone marrow
		liver
cardiac infarct		
In-111	colloid	blood pool
		spleen
I-123	sodium iodide	bladder wall
		kidney
I-131	iodohippurate	kidney
		liver
Xe-127	gas	thyroid
		kidney
Xe-133	gas	liver
		lungs
Tl-201	chloride	cerebral blood flow
		lungs
Tl-201	chloride	cardiac infarct

DMSA dimercaptosuccinic acid  
 DTPA diethylene triamine pentaacetic acid  
 HIDA N-(2,6-dimethylphenyl)carbamoymethyl iminodiacetic acid  
 HSA human serum albumin  
 MDP methylene diphosphonate  
 RBC red blood cells

TABLE III : Radiopharmaceutical labelled with Positron Emitters

Isotopes	Labelled agent	Application
C-11	carbon monoxide	blood volume
	carbon dioxide	blood flow, tissue pH
	ethanol	blood-brain barrier permeability
	glucose	brain metabolism
	deoxyglucose	brain metabolism
	palmitate	heart metabolism
	natural amino acids	tumor localization
N-13	ammonia	perfusion, metabolism
	natural amino acids	tumor localization
O-15	carbon monoxide	blood volume
	water	blood flow
	carbon dioxide	blood flow, tissue pH
	molecular oxygen	metabolism
F-18	fluorodeoxyglucose	brain metabolism

high differential uptake tend to leave the surrounding tissue cold, this in part explain why isotope imaging can produce good quality images even with a reduced quantity of radioactive tracer. Another requirement placed on radiopharmaceuticals is a short biological half life, which is influenced by the release time following the administration of the drug. This represents the time during which the labelled compound remains in the body prior to being excreted. If the biological decay is exponential, then the effective half life for a radiopharmaceutical, given by the combined physical ( $T_p$ ) and biological ( $T_b$ ) properties of the labelled compound, is reduced according to the relation (Johns et al 1974):



$$\frac{1}{T_{\text{eff}}} = \frac{1}{T_p} + \frac{1}{T_b}$$

The quality of nuclear medicine images is also related to the type of detection system employed for a given radiopharmaceutical as suggested by point b). The development of new tracers has been paralleled by the development of new detecting materials with higher efficiency to  $\gamma$ -rays than the available Geiger counters. From crystallography came the knowledge that certain crystals of high density could absorb  $\gamma$ -rays, producing a flash of light in the interaction. A number of fluorescent substances, both organic and inorganic have been tried in the past. Examples are crystal naphthalene and calcium tungstate; this last material was used by Cassen and Curtis (1951) in the first rectilinear scanner. Amongst the inorganic crystals, sodium iodide doped with thallium emerged as the scintillator of choice because of its higher density and higher detection efficiency to most gamma ray energies employed in nuclear medicine. Sodium iodide crystals were first used in commercial rectilinear scanners and, because of their ability to be grown to a large size crystal, they soon became the exclusive scintillator in gamma camera construction; a device first developed in 1957 by H.O. Anger.

Special purpose scintillators for x-CT and positron imaging have produced a number of interesting new possibilities. Bismuth germanate, BGO ( $\text{Bi}_4\text{Ge}_3\text{O}_{12}$ ) and

cesium fluoride (CsF) are presently being used in positron imaging because of their higher detection efficiency for 511 KeV, due to the higher density particularly for BGO (Cho et al 1977, Thompson et al 1979, Derenzo et al 1981, Hoffman et al 1981), and for the faster decay time required in time of flight imaging, provided by cesium fluoride (Alleman et al 1980, Mullani et al 1980, Ter-Pogossian et al 1981).

Although nuclear medicine can produce images using a lower amount of tracer than any other technique (Kaufman et al 1982) image contrast is often lost because of the poor spatial resolution of the available instrumentation. Note that contrast is viewed as a measure of the signal as a function of the background intensity (Rose A. 1973). According to Kaufman improvement of instrument resolution, rather than sensitivity, will produce a considerable gain in the image quality. This is in opposition to the widely accepted view that nuclear medicine images are count (statistically) limited (Shosa et al 1981). Some authors claim that spatial resolution not only affects the ability to detect and outline small lesions, but good resolution will also increase the contrast of the output image (Kaufman et al 1982). As a consequence, tomographic techniques will not be sufficient to increase the information content of reconstructed images, but this will only be the result of improved resolution in planar images, yielding the single projections (Kaufman et al 1980). The increased instrument resolution and resulting gain in image contrast could be combined to advantage in nuclear medicine

by producing higher quality diagnostic images with smaller amounts of radiotracer. In addition, this will result in a lower risk for the patient, and particularly for the technical personnel, because of the exposure to lower levels of radiation. In the case of the patient, the radiation dose delivered is related to the activity function which depends on the amount of administered activity, the rate of biological uptake and excretion of the radiotracer and physical characteristics of the radionuclide (Kereiakes et al 1980).

### 1.3 Physics in nuclear medicine

The full potential of nuclear medicine imaging is not being totally exploited mainly because of a lack in the instrumentation resolution. It appears that some evolutionary improvements in today's instrumentation should be adequate to update present technology (Kaufman et al 1982).

Nuclear medicine instrumentation has changed considerably over the last few decades. From tracing techniques, employing geiger counters to measure whole body functions, it has developed into a four dimensional functional mapping technology. The instrumentation has progressed from scanning devices to static instrumentation able to produce two dimensional images following the invention of the gamma camera by H.O. Anger in 1957.

Stimulated by transmission CT popularity and following the addition of computers in nuclear medicine departments, three dimensional emission computed tomography employing single or dual head gamma cameras was a logical development. Single and multiple ring detectors for positron emission tomography are among recent additions to nuclear medicine instrumentation.

### 1.3.1 2-Dimensional imaging devices

#### Rectilinear scanner

The rectilinear scanner represents the first 2-dimensional imaging system employed in nuclear medicine. Developed by Cassen and co-workers in the early 50's, this device was, for a short period of time, the main 2-dimensional imaging system used for clinical imaging in nuclear medicine. The schematic diagram in Figure 1.1 shows a typical scanning system consisting of detector, pulse height electronics and image forming display unit.

Detectors in commercial rectilinear scanners exclusively employ sodium iodide crystals with typical dimensions of 12.7 cm in diameter and 5 cm thick. The detector views the activity through multihole focussing collimators where the size of the holes defines the resolution and sensitivity at a predefined depth. A mechanical system advances the detector by a constant spacing and then tracks across the subject to cover the

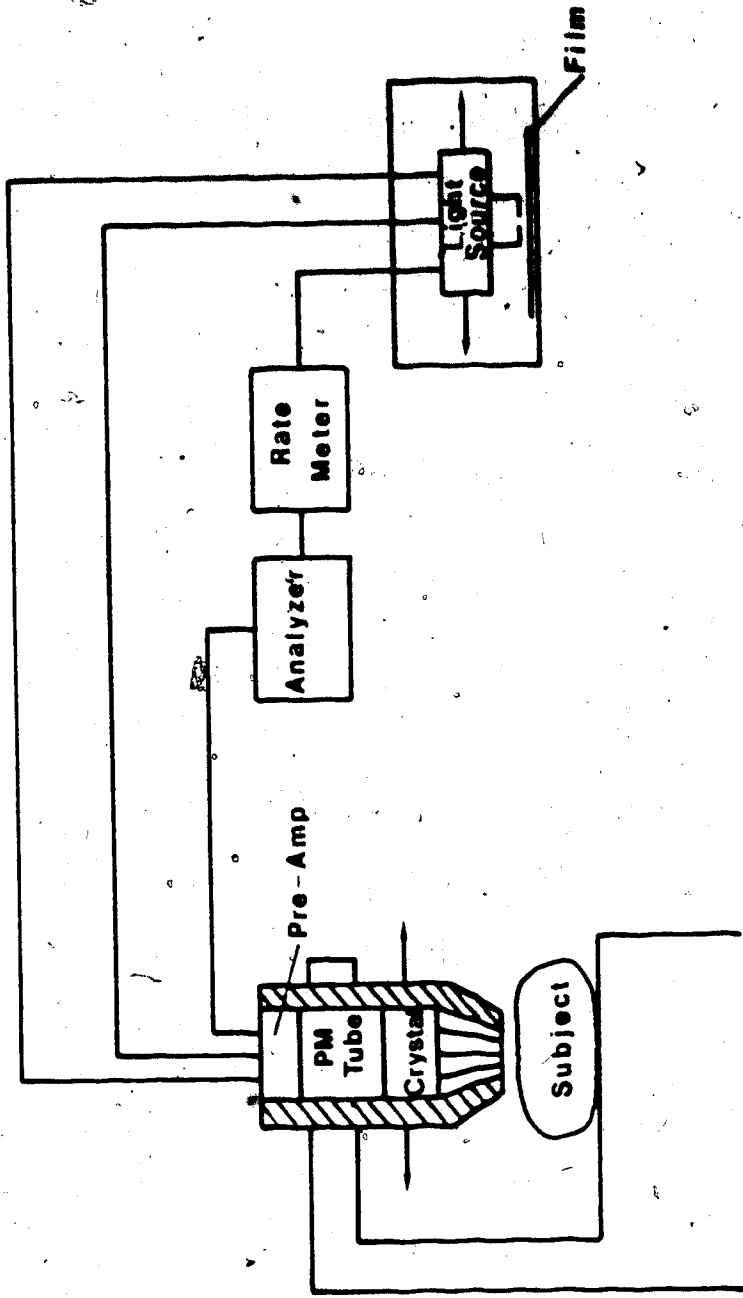


Fig. 1.1 Simplified diagram of a rectilinear scanner.

entire field of interest. A single photo-multiplier (PM) tube provides the first stage amplification of the light signal produced by the crystal. A pulse height analyzer with normal operating window width of 20% discriminates between photopeaks or scattered events. The detected signals which fall within the energy window settings are then recorded by any of a number of display devices, such as paper tapper, oscilloscope or photorecorder. In the most common recording units the measured activity is displayed on photographic film, using a pulsed beam of light. The position of the light source is often a one-to-one representation of the detector position over the scan area. The number of light pulses projected over the film is proportional to the number of detected photopeak events. In the specific case of whole body scanners the images are usually minified to suit the display mode.

Using the same operating principle are multicrystal whole body scanners, such as the Cleon whole body scanners manufactured by Union Carbide. This system incorporates a row of crystals each operating as a single scanner crystal. The advantage of this imaging device is a faster image production, particularly useful in bone scanning (Rollo et al 1981).

#### Scintillation gamma camera

First introduced in nuclear medicine by H.O. Anger in

1957, this instrument remains the most important 2-dimensional imaging system currently employed in nuclear medicine. In contrast to the rectilinear scanner which produces images by sequentially measuring the activity for each point in the image, the gamma camera views simultaneously all point in the subject. The time to produce an image is considerable shorter than the time it takes the rectilinear scanner to produce an equivalent image. Through the years, the construction of the gamma camera has experienced a great deal of technical improvement, while the principle of operation has remained basically the same. Improvements have modified the construction and assembling of collimators, scintillator dimensions, light collection systems and signal handling electronics. Gamma cameras have now progressed from a stationary detector to moving camera head for whole body imaging. The Anger camera remains the most valuable imaging system in nuclear medicine because of the optimal combination of performance parameters. The current trend in camera instrumentation is towards improving the camera intrinsic resolution, uniformity and sensitivity. Examples of gamma cameras with a large number of PM tubes are the GE 400A with 61 tubes and the Siemens Pho/Gamma with 75 tubes. These systems have intrinsic spatial resolutions of approximately 3.5 to 4.0 mm, uniformity of 5-6% together with high detection efficiency to gamma-rays in the range of 100-300 KeV. Microprocessors are now standard support systems, and are used in part, to correct for spatial

distortion and non-uniformity.

Figure 1.2 shows a simplified schematic diagram of a typical scintillation gamma camera circuitry. As indicated in the diagram, the system comprises a collimator placed in front of a large scintillator, which is enclosed in sufficient shielding material and separated from the collimator by a thin aluminium window. An array of PM tubes, optically coupled to the crystal, yield a signal which is proportional to the amount of light produced in the interaction of a  $\gamma$ -ray with the crystal. The output of the photomultiplier tubes are fed into a matrix circuit which produces the four position signals. These will be described in more detail in Chapter 2, in the discussion of the Pho/Con gamma camera. The output of the PM tubes is summed to give the energy signal (Z-pulse) which is routed into the pulse height analyzer (PHA) to determine the energy of the detected event. If the pulse falls within the preselected PHA energy window, the signal is reproduced in the CRT tube, where the image is formed. Permanent display and storage of the image is obtained using photographic film. Parallel to the improvement of camera technology, special purpose devices have been constructed with the intent of substituting them for the gamma camera in specific imaging procedure. These systems are the multicrystal camera, and coded aperture devices used in cardiac imaging.



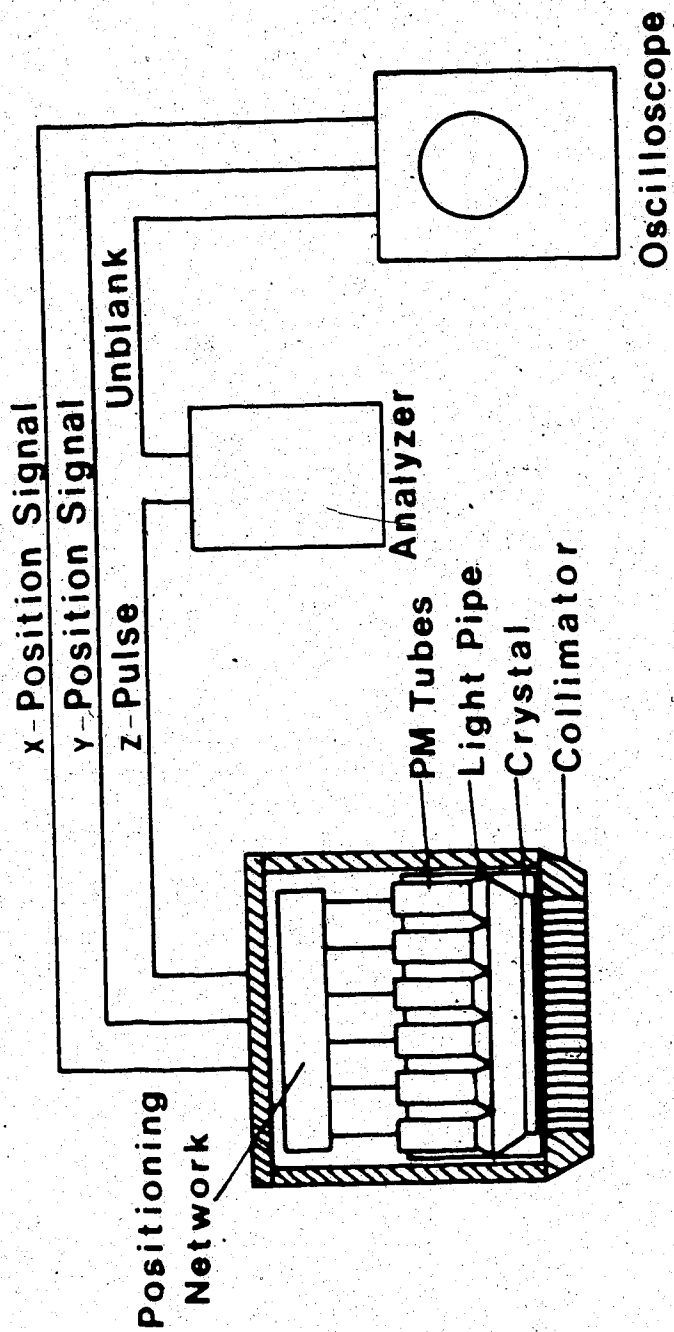


Fig. 1.2 Basic components of an Anger gamma camera.

Devised in 1962 by Bender and Blau this system never received strong support because of lower spatial and energy resolution values compared to those achieved with Anger gamma cameras. These limitations result from the detector design which consists of a large array of NaI(Tl) crystals coupled through a sophisticated network of light pipes to the PM tubes. Presently the only instrument commercially available is the system 77 manufactured by Baird Atomic Corporation. System-77 contains 294 NaI(Tl) crystals of approximate dimensions 0.8 cm x 0.8 cm by 3.8 cm thick. These crystals are assembled in 14 columns and 21 rows with a center-to-center separation between crystals of 1.1 cm. Again collimators must be employed, either multihole types with one hole per detector element, or alternatively pinhole collimators. Events are recorded when only one X and Y address are registered and the sum of the two pulses falls within the analyzer energy window. In addition, both column and row PM tubes must sense the event simultaneously. System-77 finds use in cardiology because it can operate at high count rate without causing spatial distortion.

#### Coded aperture devices

One of the major limitations of the 2-dimensional imaging devices described so far is due to the small number of photons reaching the detector as a result of collimation thus reducing the quality of the images produced. Typically only 0.01% of the radiation emitted by the subject is

detected (Simpson et al, 1980). An increase in the size of collimator holes would undoubtedly increase the number of events reaching the detector causing, however, a loss in the system resolution. Coded aperture imaging systems offer the best compromise between system gain in sensitivity and loss in resolution. This technique varies from traditional nuclear medicine imaging in that the final image must be recovered from collected coded data. In the coding process, the selected aperture is placed between the subject and the detector usually an uncollimated gamma camera. The apertures, which are made of material opaque to x-rays, are selected with respect to the characteristic decoding process. Examples of apertures which have found some use are Fresnel-zone plates, annular apertures and multiple pinhole arrays (Simpson et al, 1980). The coded image consists of an overlapping of shadows projected from each point in the object onto the detector. The image is then recovered by deconvoluting the shadowgram using Fourier techniques..

### 1.3.2 3-Dimensional imaging

The desire to isolate an organ under investigation from the remaining body structure resulted in an imaging modality in which 3-dimensional structures are projected into planar images. The gray scale intensity in the image would normally provide a sense of depth giving the feeling of a

third dimension. Better 3-dimensional visualization occurred with the development of tomographic techniques in which 3-dimensional structures are presented as a series of 2-dimensional slices or cuts. These techniques are now implemented both on systems operating on the principle of focal plane tomography and on reconstruction from projection data. Within the first group of devices we have the Pho/Con tomographic scanner invented by H.O. Anger (1968). Details of this system construction and operating characteristics will be given in a following chapter. Other focal-plane tomographic systems are the multi-wire proportional chambers (MWCP) which have found limited application and are employed in positron imaging on an experimental basis. In addition to the above systems longitudinal tomography performed using the 7-pinhole and slant-hole collimator have found some application in cardiac imaging (Vogel et al, 1977, LeFree et al, 1981, Chang et al, 1981, Lin et al, 1981). Myocardial perfusion tomography using the seven pinhole collimator has shown to be superior to planar imaging by improving the sensitivity for detection of coronary artery diseases from 0.75 to 0.95 (Kirch et al 1980). However, the acceptance of the seven pinhole technique has been limited by the required higher standard of performance of the gamma camera and the extreme care required in patient positioning. This latter is such that the patient left anterior oblique position be modified to render the heart major axis perfectly symmetric to the pinhole system central axis.

### Seven-Pinhole

This technique employs an Anger gamma camera as the front end of the imaging system. The collimator is normally made of lead of sufficient thickness to shield the detector from the emitter used. The pinhole plate is mounted parallel to the gamma camera crystal (Le Free et al, 1981). The size of the pinhole can vary depending on the desirable compromise between resolution and sensitivity. The system is calibrated for uniformity using a flood of the same isotope to be used in the imaging procedure. This will result in the uniformity calibration image. A second image called the reference point projection is obtained by imaging a point source placed at a known distance coaxially with the central pinhole. In coding the image, the pinhole plate is placed between the camera and the radioactive object which casts overlapping shadows of the activity onto the detector through the seven pinholes. In the decoding process, the reconstruction algorithm searches iteratively for a 3-dimensional distribution which would match more closely the shadogram produced by the object.

The main limitation of focal plane tomography is due to the noise in the image caused by the blurring of underlying and overlying structures. This type of instrumentation is most useful in the imaging of a fairly localized activity distribution.

The second approach to emission tomography is typical of x-ray CT where the tomographic slice is constructed using

multiple views. This type of reconstruction employs present nuclear medicine  $\gamma$ -ray emitters performing single photon emission computed tomography (SPECT). Early work on SPECT by Kuhl and Edwards (1963) employed a scanning device. The latest version of their system has produced the Mark IV, which utilises a ring of detectors with variable length focussing collimators (Kuhl et al, 1976). Gamma cameras have also been employed in transverse section imaging by various groups (Freedman, G., 1970, Budinger et al, 1974, Keyes et al, 1977, Jaszczak et al, 1976). A second group of devices perform section imaging using the coincidence detection of two  $\gamma$ -rays produced by the positron-electron annihilation. This technique applies to positron emission tomographic (PET) systems. The coincidence counting establishes what is called electronic collimation (Phelps et al, 1975) thus eliminating the need for conventional collimation. With PET techniques the line joining the two coincidence events determines the annihilation channel. The reconstruction requires a large number of samplings in the linear and angular directions thus allowing to define the annihilation plane. The in-plane resolution depends on the energy of the positron emitter and also on the algorithm used to reconstruct the image plane. In a circular PET system using BGO detectors (Derenzo et al 1981) the resolution at the centre of the ring can vary from 6.5 mm at 0.54 MeV for Na-22 to 7.7 mm at 1.9 MeV for Ge-68. In most recent developments, PET systems employ time of flight discrimination to determine the position along the

coincidence line where the annihilation has taken place. Both positron imaging modalities, however, are most suitable to those institutions which have cyclotron facilities for the production of the required positron emitters.

Many of the SPECT systems presently in use in nuclear medicine employ large-field-of-view gamma cameras with 1 or 2 heads mounted on a rotating gantry (Jaszczak et al, 1977, Jaszczak et al, 1979, Larsson, S.A., 1980). The most immediate advantage of using Anger cameras is the flexibility of employing the same device for planar imaging procedures.

#### Gamma camera SPECT

Reconstruction using a single or dual head gamma camera requires accurate positioning of the detector around the patient. Accurate positioning at equally spaced angles around the subject is achieved by mounting the camera on a rotating gantry. One of the camera coordinate axes is oriented along the motion of rotation of the camera head while along the normal axis the camera can be viewed as a row of probes which will cover the entire area to be imaged, thus producing a series of projection planes to cover a spherical volume with the diameter equal to the camera field of view. The number of planes which can be obtained would depend exclusively on the size of the selected matrix in the gamma camera. This is effectively dictated by the acceptable statistical fluctuation in the reconstructed

image and by the required resolution; these two parameters are interdependent. The quality of the image is a function of the size of the matrix, the acquisition time, and the number of sampling angles. While poor resolution of the gamma camera precludes the need for high frequency sampling (number of matrix elements) angular sampling is restricted by the number of projections required to produce good quality images and by the examination and reconstruction time. SPECT reconstruction algorithms are adversely affected by variation in the depth response because of the collimator, by the attenuation of photons in traversing the body and by scattered photons. An example of algorithms presently in use in single photon tomography is given in a review paper by S.A. Larsson (1980).

#### 1.3.3 4-Dimensional imaging

The dynamic measurement of the change in shape and dimensions of anatomical structures require the addition of time, as the fourth dimension, to 3-dimensional spatial imaging. This allows one to resolve or characterize in space and time the dimension of moving organs, such as heart and lungs, within the time frame of their physiological activity. The instrumentation requirements for this 4-dimensional imaging is high temporal resolution capable of freezing the motion of the organ in much the same way as a photograph of a child captures one instant of his busy daily



activity.

Efforts are presently being made in x-ray CT to produce scanners able to yield volume scans in one second or less, with the spatial and density resolution of current scanners (Wood et al, 1979, Boyd et al, 1982).

In nuclear medicine the 4-dimensional imaging is presently limited to cardiac studies. In such procedures gated blood pool images can be displayed to show the heart volume changes with time. This is achieved by collecting a series of functional images of the relative ejection fraction. The usual approach is to acquire the data gated with the patient's ECG thus obtaining a series of images which divides the cardiac cycle into a suitable time frame (King et al, 1981, Byrom et al, 1981).

#### 1.4 Summary

In this chapter an attempt has been made to identify past and present imaging methods employed in medicine. A classification of these methods has been made according to the physical principles employed by the various imaging modalities at the same time indicating some of the advantages and disadvantages of each modality. Nuclear medicine has been isolated from the remaining techniques because of its ability to convey physiological as well as pathological information through the images it produces. Higher dimensional imaging methods which are possible with

radioisotopes has also been presented. In describing the various modalities and with the intent to preserve continuity in the chapter, whenever the need arose for the physical formulation of the principle under discussion, reference was made to recent review articles.

The remaining parts of this thesis are devoted to the study of the Pho/Con: one of many instruments currently in use in nuclear medicine. The Pho/Con is the only commercial system which can perform longitudinal tomography without the aid of a computer. It can perform whole body imaging, which is a very useful imaging procedure in monitoring the metastatic spread of malignant disease using bone or tumor seeking agents. Chapter 2 deals mainly with the principle of operation of this device. Chapter 3 contains some measured performance parameters for the Pho/Con collimator and gamma camera. The end of Chapter 3 deals mainly with the system performance measured using analogue and digital processing of the data. Chapter 4 deals with focal-plane tomography which is the reconstruction technique employed by the Pho/Con. In the same chapter a technique is presented which attempts to deblur Pho/Con images using iterative refinement of an initial estimate of the activity distribution. Results using a mathematical phantom will be presented. Chapter 6 will attempt to summarize the results obtained in both Chapter 3 and Chapter 5 with a view to increasing, the Pho/Con usefulness.

## CHAPTER 2-

### 2.1 Tomography in nuclear medicine

Emission computed tomography (ECT), was first developed by Kuhl and Edwards in 1963. This tomographic technique preceded the development of transmission computed tomography (CT). Despite initial optimistic reports, ECT techniques received little acceptance in nuclear medicine mainly because of limited computer facilities then available. Emission computed tomography lost, temporarily, some of its original appeal, while developments in medical imaging were centered around transmission CT.

The neglect which surrounded ECT was due in part to the greater complexity of the reconstruction problem associated with single photon tomography. With this technique one attempts to measure either the relative or absolute regional concentration of radioactivity in living tissue. This in turn describes a number of physiological quantities which determine the presence or absence of uptake. Thus, the measure of the activity concentration is affected not only by the instrumentation but also by the type of radiopharmaceutical employed. In the case of transmission CT one measures the attenuation of a known source of x-rays while traversing a specific region of the human body. What CT was able to produce was the mathematical tool necessary in the tomographic reconstruction based on Fourier's

techniques (Cormack A.Y. 1963, 1964, Bracewell et al 1967, Bates et al 1971, Shepp et al 1974) and on an iterative approach (Goitein 1972). The technological development which surrounded CT, however, provided the necessary knowledge and computer facilities for emission CT to become an alternate imaging modality in nuclear medicine.

Early work on emission tomography was mainly confined to imaging of the brain, since this organ was more suitable for modeling in computer simulated studies. In addition, the production of radiopharmaceuticals labelled with a "physiologic" short lived positron emitter (C-11, O-15, N-13, F-18) further concentrated the efforts with respect to the quantitative studies of brain function (Thompson et al 1979, Hoffman et al 1981, Phelps M.E. 1981). A better understanding of the reconstruction algorithm and improved detector technology has in the end contributed to the development of both single photon ECT (SPECT) (Anger H.O. 1968, Kuhl et al 1976, Keyes et al 1977, Chang et al 1980) and positron tomography (PET) systems, both capable of performing whole body imaging (Hoffman et al 1976, Cho et al 1976). The advantage of positron emission tomography over single photon ECT are high resolution and high sensitivity; areas in which present SPECT systems are lacking most. The use of PET imaging techniques, however, have been confined to those institutions with suitable cyclotron facilities which are necessary for the production of positron emitting isotopes. Although SPECT techniques have been employed for some time in nuclear medicine, the wider use of such

techniques has been limited by the lack of suitable commercial instrumentation which would combine good sensitivity with spatial resolution finer than the present 15 mm full width at half maximum (FWHM) of the point spread function (PSF) (Budinger T.F. 1982). The renewed interest in single photon tomography can be attributed to improved instrumentation along with the development of radiopharmaceuticals with higher affinity for the organ under investigation. Recent application of planar imaging devices, such as gamma cameras, to section imaging, has contributed to the spreading of tomographic techniques to many nuclear medicine departments. The main advantage of this latter approach is the flexibility of switching from conventional planar imaging modality to tomographic examination whenever required by the particular investigation. The ability to use gamma cameras to do tomography has now limited the usefulness of some earlier systems performing focal plane tomography (Anger 1968, Muehllehner 1970, Barret et al 1973, Vogel et al 1978) and section imaging from projection (Keyes W.I. 1976, Bowley et al 1973, Stoddart et al 1979).

The Pho/Con represents an early multiplane tomographic device employed in nuclear medicine which has been used on account of its ability to produce simultaneously 12 longitudinal tomographic cuts at various depths in the subject. Some of its early popularity resulted from the ability to produce whole body images of significant diagnostic value particularly in bone imaging with  $^{99m}\text{Tc}$ .

and in tumor uptake imaging with Ga-67. For these two clinical applications the limitation associated with plane tomography, that is of unwanted out-of-plane blurring in the image, is considerably reduced because of the very localized concentration of the labelled pharmaceutical.

## 2.2 Pho/Con tomographic scanner

The Pho/Con is a dual head, multiplane tomographic scanner which provides twelve longitudinal images of the activity distribution in a subject; six for each detector. The system is characterized by two Anger scintillation gamma cameras equipped with focussed collimators. The two detectors are mounted coaxially on a frame which moves with respect to a stationary bed. The two detectors, one above and one below the bed, move in a conventional rectilinear scan mode.

Figure 2.1 shows a photograph of an early Pho/Con model manufactured by Searle radiographics (now Siemens Gammasonic) which is presently in use in the Nuclear Medicine Department at the Cross Cancer Institute. Recognizable, in the photograph, are the two detectors, the control console and the microdot imager situated at the far right. A block diagram of the scanner detector is shown in Figure 2.2. The system operates in part as a traditional rectilinear scanner in which the position of the detector normally determines the location of a detected event. The



Fig. 2.1 Photograph of Pho/Con system showing the scanning heads, control console and microdot imager.

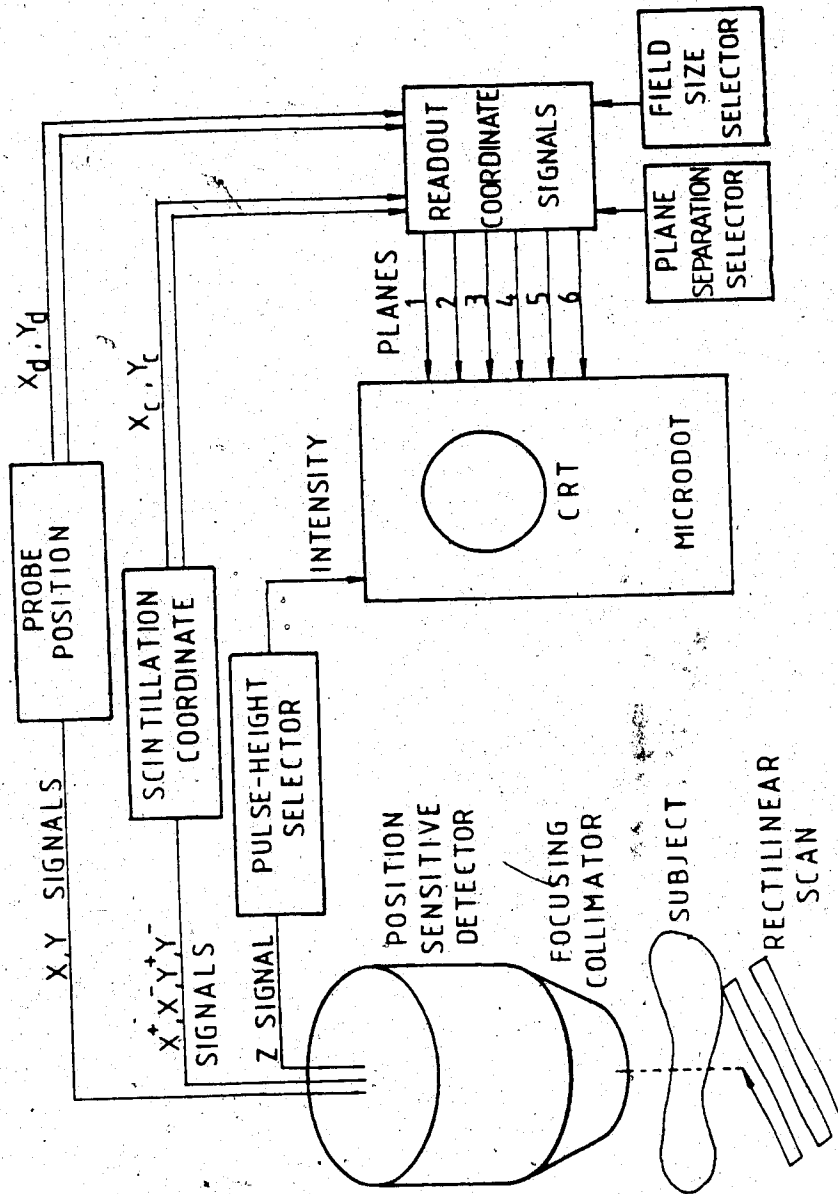


Fig 2.2 Schematic diagram of one probe of the Pho/Con multiplane longitudinal scanner. (After L.S. Graham, V. Perez-Mendez : In Nuclear Medicine Physics, Instrumentation, and Agents. Edited by F.D. Rollo p.275, 1977)



departure from a simple scanning device is due to the addition of a position sensitive detector, namely an Anger gamma camera, which replace the traditional detector. With the Pho/Con, the detector position signal and event position signal in the gamma camera are combined to yield an event position signal relative to the scan area. The combined properties of the camera focussed collimator, together with the scan motion of the detectors allows the system to reproduce simultaneously, for each detector, six longitudinal views of the activity distribution at pre-selectable depths in the subject.

#### 2.2.1 Scanner: Principle of operation

Scanning devices developed in the early 1950's represent early automated imaging devices employed in nuclear medicine. In its present form, the rectilinear scanner consists of a collimated sodium iodide NaI(Tl) crystal coupled to a photomultiplier tube. The PM tube signal is analyzed using conventional pulse height discrimination. The motion of the detector over the patient is followed throughout by electrical or mechanical means by a readout device which produces an image of the activity distribution in the region of interest.

In the Pho/Con system, the position of the detector and coaxial frame is determined through digital signals which

control the motion of the coaxial frame and detector. These signals are converted into "up" and "down" clock pulses for the detector position counter (Pho/Con Service Manual). The X and Y output of the detector position counters are continuously converted into analogue signals and routed into the Pho/Con imager where together with the camera signals they are converted into event position signals.

### 2.2.2 Gamma camera

The gamma camera employed in the Pho/Con consists of a sodium iodide crystal 2.5 cm thick by 24 cm in diameter, viewed by seven photomultiplier (PM) tubes positioned next to the crystal and arranged in a hexagonal configuration as shown in Figure 2.3. The scintillation produced in the crystal is observed by all the PM tubes via a light pipe coupling. The charge pulse produced by each of the PM tubes, which is proportional to the solid angle subtended by the PM tubes, is fed into separate linear preamplifiers and the resulting signal is then directed into a resistive electronic network. This network is designed to produce voltage pulses ( $\pm X$  and  $\pm Y$ ) which give the location of the interaction as well as determine the energy of the event. The energy of the  $\gamma$ -ray is linearly related to the sum of the four output voltage pulses, while the event coordinates are obtained by the differential sum between pairs of pulses ( $+X, -X$  and  $+Y, -Y$ ) after correction is made for the signals

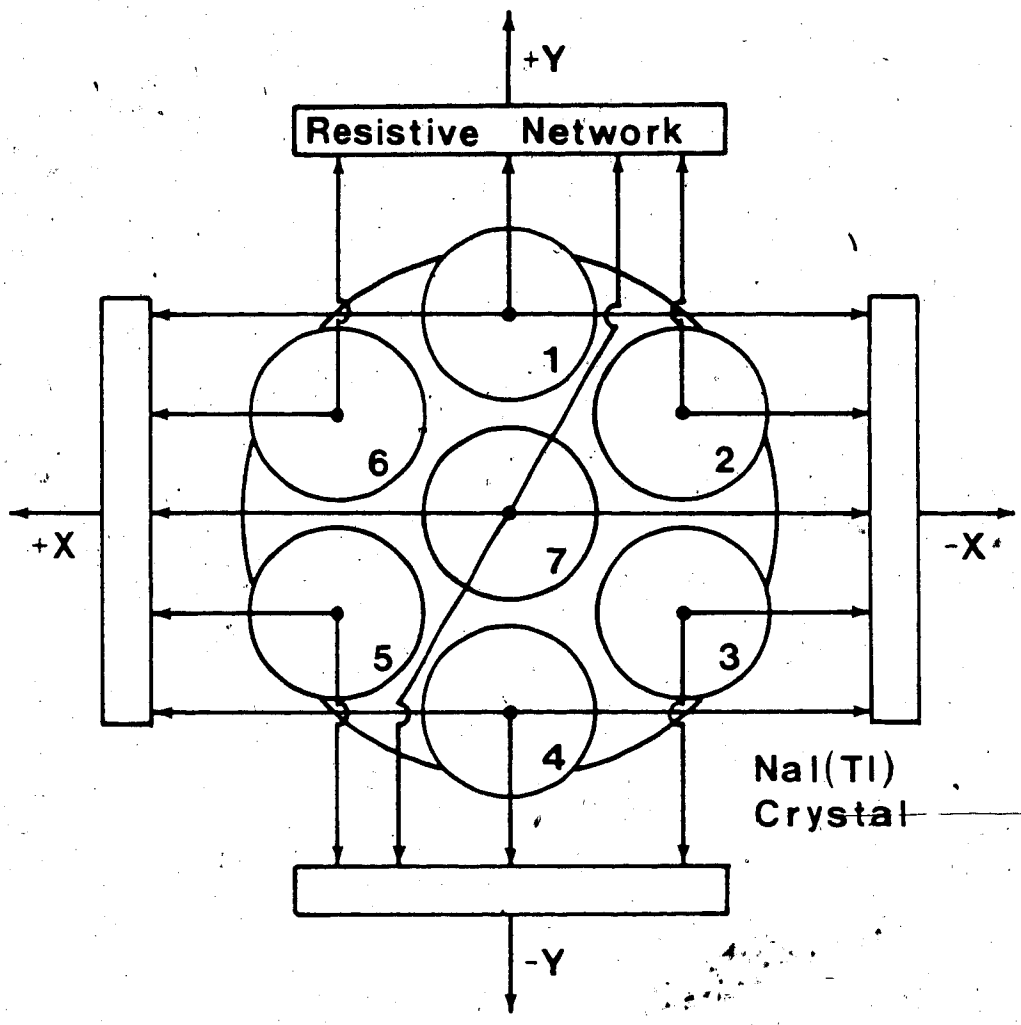


Fig. 2.3 Simplified schematic diagram of 7-PM tubes Anger camera with positioning signals.

energy dependence. These signals are routed into the imager console where they are combined with the detector position signals (Pho/Con Service Manual).

### 2.3 Pho/Con: Principle of operation.

The scintillation resulting from the interaction of a photon with the crystal is analyzed in the usual Anger gamma camera mode, by assigning to each event, position and energy information. The scintillation position in the crystal (X,Y) and the detector position in space (X,Y) are combined in the readout electronics which produces the event position in the cathode ray tube (CRT) of the microdot imager. Each event is reproduced on all six readout planes according to a pre-defined arithmetic. The six position information data points, are projected on the CRT screen into one of the six dedicated areas, on the face of the CRT, which are reserved for the upper detector. An additional six areas are reserved for the lower detector. During the scan the magnified image of the CRT screen is recorded onto photographic film for final display of the image. The twelve images constructed by the microdot imager yield the activity distribution at different focal depths in the subject. This depth discrimination has been described as "focal-plane tomography with a disc shaped blur pattern" (Anger H. O. 1969).

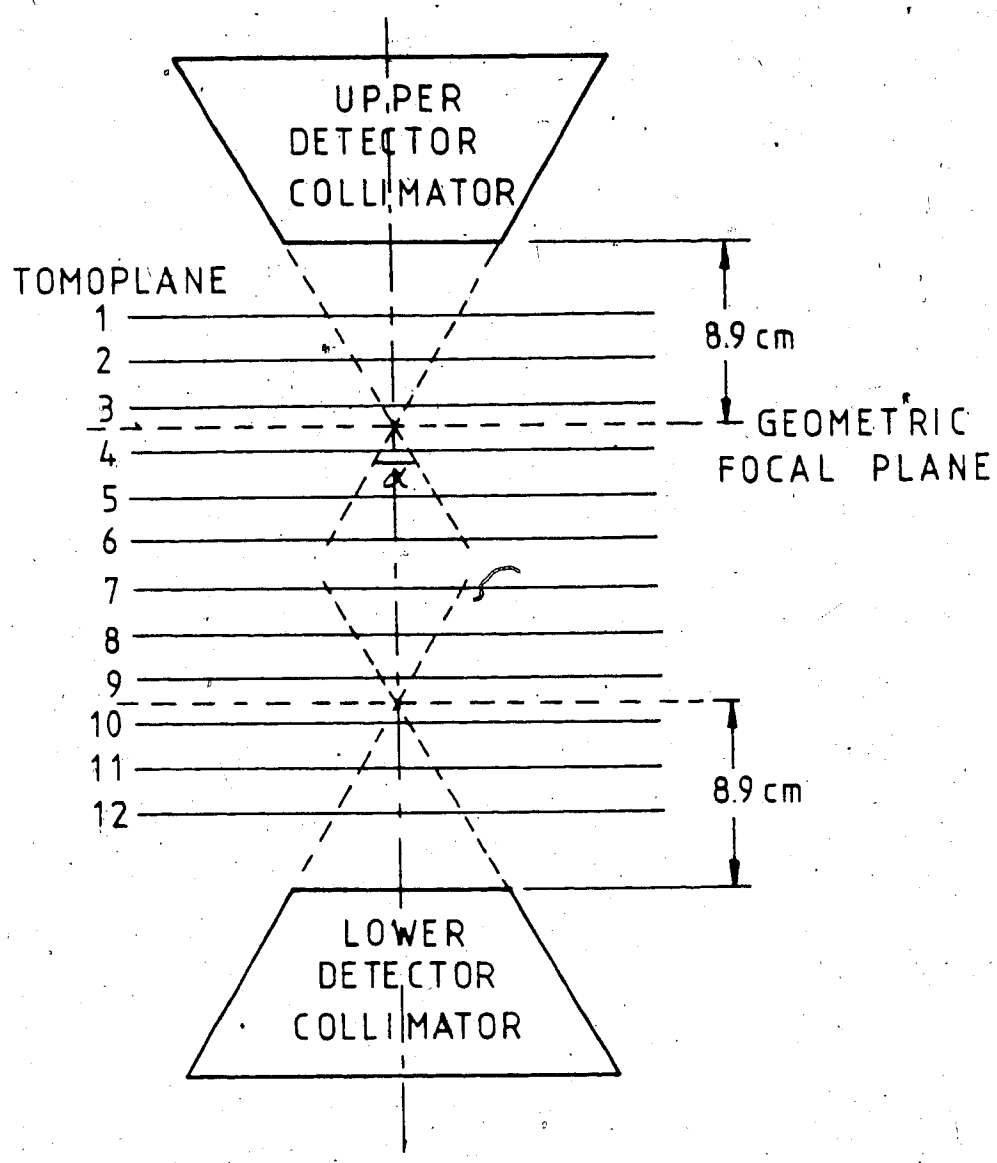


Fig. 2.4 Pho/Con upper and lower focussed collimators showing the 12 longitudinal readout planes and the location of the geometrical focal plane.

Figure 2.4 is a simple representation of upper and lower converging collimators with the twelve longitudinal cuts. As shown, the geometrical focal plane for the upper collimator, at a fixed distance of 8.9cm from the collimator face, falls halfway between the third and fourth plane. The angle of acceptance  $\alpha$  is defined by the intersection of the central lines of the two outer collimator holes. The separation between the discrete longitudinal focal planes is controlled by the physical characteristics of the collimator, the maximum scan area and the tomo-separation switch position. The maximum scan area is the area covered by the center of the collimator while the tomo-separation switch defines the distance between planes of focus for a given scan area. In our system for fixed Pho/Con settings, the distance between consecutive planes is constant and measured from the collimator face.

The tomographic effect is achieved by the interdependence of event positional information created by the characteristics of the focussing collimators, which define the event line-of-flight, and the detector scanning motion. The combined effect is similar to classical linear blur tomography in radiology. This is such that activity distribution near the plane in focus is sharply resolved while off plane activity is blurred. For any readout plane the amount of dispersion of underlying or overlying activity increases with increasing distance from the plane of interest and also on the collimator physical

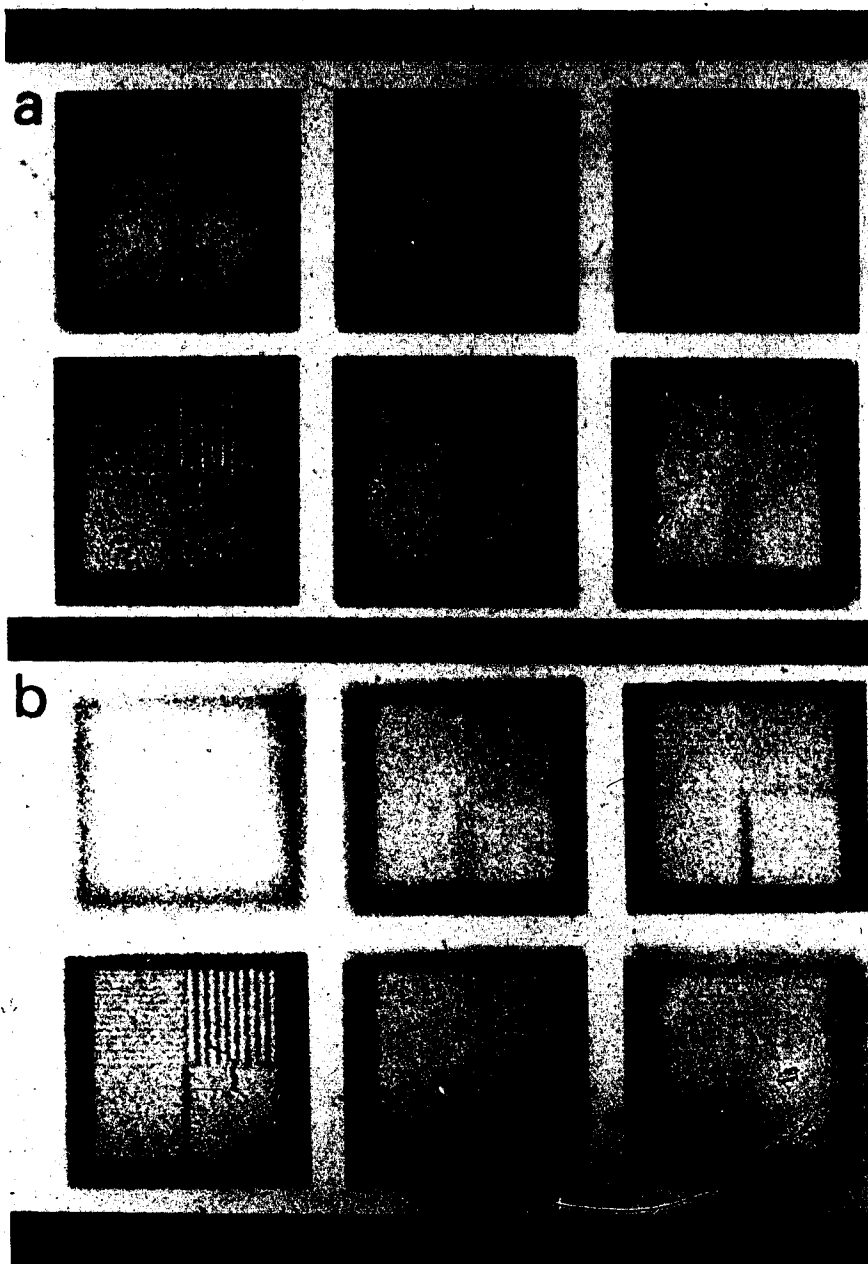


Fig. 2.5 Transmission image of a bar phantom with pattern spacing of 3.18, 4.76, 6.35, 9.52 mm obtained with a) normal collimator, and b) minimum acceptance angle aperture of  $48^\circ$ .

characteristics, (in particular, on the angle of acceptance  $\alpha$ ). The larger the angle, the greater is the tomographic effect. A simple demonstration of the focussing property of the collimator is shown in Figure 2.5 which represents the contrast images of a lead bar phantom obtained with the Pho/Con lower detector. The bar phantom was placed on the table with a uniform source of Tc-99m extending over the phantom at approximately the collimator focal depth. The images were obtained using a maximum scan area of  $45 \times 45$  cm at a speed of 180 cm/min. with the analyzer window set at 15% of the photopeak energy. The scanning configuration was kept constant with the exception of the angle of acceptance which was changed by shielding part of the collimator holes at the entrance side with lead. The image of Figure 2.5a is a normal representation of the bar phantom while Figure 2.5b was obtained by masking the collimator entrance holes with the exception of the outer two row of the hexagonal array of holes. In Figure 2.5b the reduced film contrast is related to the loss in count rate resulting from the partial screening of the collimator holes. Although the adopted procedure is purely qualitative, Figure 2.5 demonstrates how the details in the bar pattern are visible in the adjacent tomo-planes more in Figure 2.5a than in Figure 2.5b obtained by restricting the acceptance angle to a minimum of approximately 48 degrees.

As stated earlier the tomographic effect is achieved by combining the motion of the detector, the characteristic of



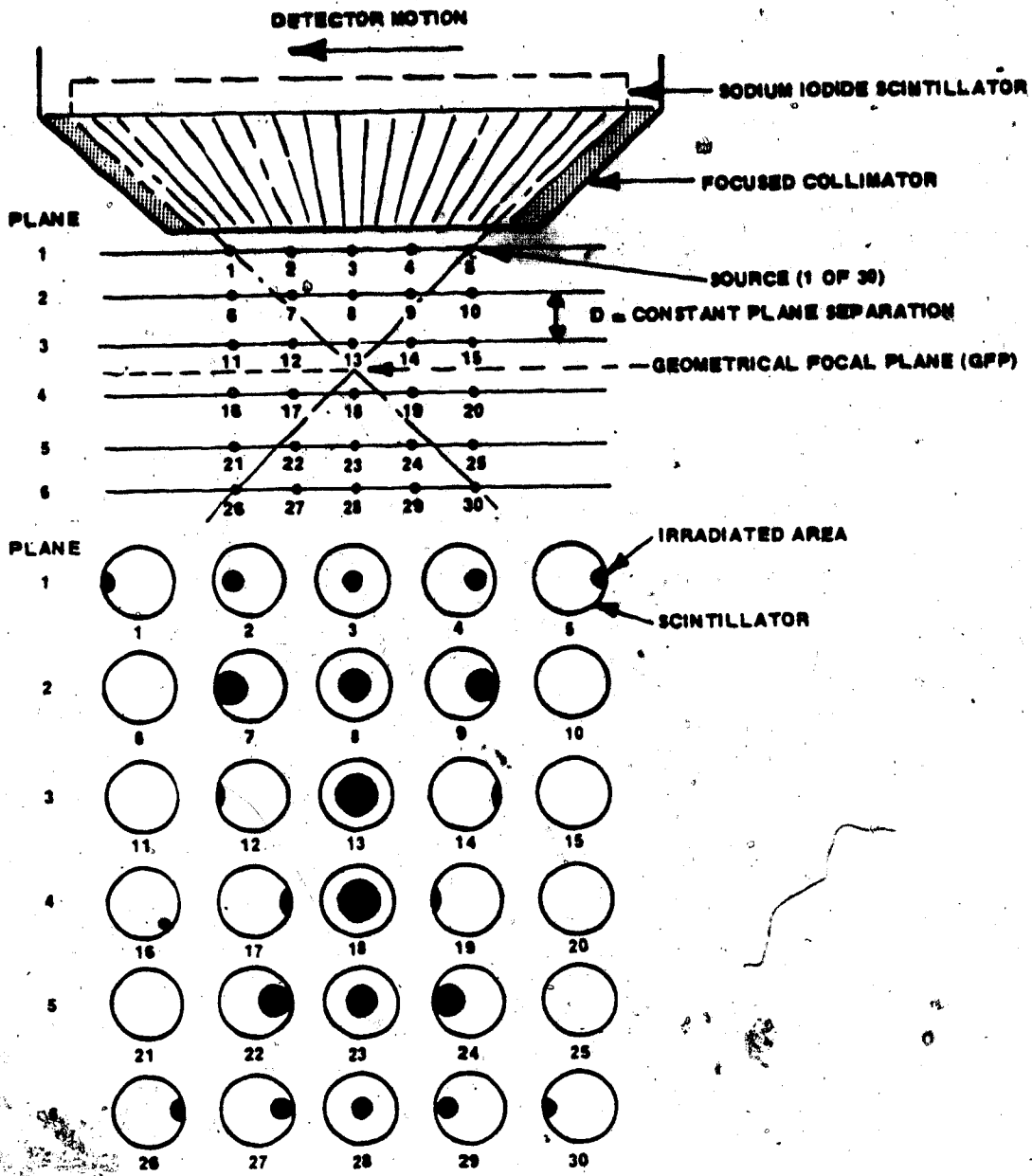


Fig. 2.6 Schematic diagram of the point source detector configuration showing the Pho/Con principle of operation. The diagram shows the irradiated area of the crystal relative to the detector-source position.

the focussing collimator, and the X and Y coordinates of the detected event. The mechanism of image formation begins when a detected  $\gamma$ -ray with the appropriate energy is replicated as a flash of light over six distinct areas of the imager cathode ray tube (CRT). The relative event position within these areas is different and is related to the speed of the detector and the distance of the source of activity from the collimator face. Figure 2.6 is a schematic representation of the Pho/Con operation depicting the detector response to a source positioned at various points in the longitudinal planes (Anger H. O 1968, Searle Manual). The spatial separation between two consecutive positions in the source plane (e.g. from position 1 to 2 in Figure 2.6), for a given scan speed, can be covered by the detector in a time interval  $t$ . The position in which the source first falls onto the detector field of view and irradiates the scintillator depends on the distance of the plane from the collimator face. For example, the source lying in plane two will illuminate the crystal between the positions seven through nine. As shown in Figure 2.6, the irradiated area will, in such case, move across the scintillator in a direction opposite to the indicated detector motion. The speed at which the irradiated area travels across the scintillator is a function of the duration of crystal exposure. In the example given, the irradiated area must travel the diameter of the crystal,  $D$  at a speed of  $D/2t$ . In the case of plane five the speed is

the same, but, the direction of motion is reversed. The speed and direction of motion of the irradiated area are fixed characteristics which allow one to discriminate between the six planes of focus. In the original system described by H.O. Anger (1968) the images were displayed on an oscilloscope and were viewed by a set of fixed lenses. Such lenses would project the image on a film that moved in synchrony with the detector much like the technique used in radiography for body section tomography. If the film movement exactly compensated for the motion of the source image in the cathode ray tube, then it would appear stationary and in focus on film. The synchrony of image motion with the speed and direction of the detector motion resulted in the focal-plane tomographic effect first devised for nuclear medicine by H.O. Anger (1968). In the Pho/Con oscilloscope, lenses and moving film have been replaced by appropriate electronic circuits which display the information on separate sections of the CRT within the microdot imager. The same tomographic effect is achieved by the creation of electrical signals according to a specific arithmetic to be described below. These electrical signals provide the current drive for the magnet deflection coils on the CRT.

The focal-plane tomographic effect can be described in a more comprehensive way by considering the expressions which determine the final readout coordinates  $(X, Y)$  by combining three units of information. These are the scintillation positions  $(X_i, Y_i)$  relative to the center of

the crystal, the detector position ( $X_c, Y_c$ ) with reference to the center of the scan area and the product  $kN$  which defines the fraction of crystal signal to be added to the detector position signals.  $k$  and  $N$  are parameters defined by the particular Pho/Con settings, namely the tomo-separation and the maximum scan area. The expression for the  $X$  and  $Y$  coordinate signals are:

$$X = X_c + kNX_i$$

$$Y = Y_c + kNY_i$$

In these relationships  $k$  reduces  $NX_i$  and  $NY_i$  so that the total scan area and the crystal dimensions are in the correct proportions.  $N$ , which can be positive and negative, varies the size of the event imaging area of the crystal as displayed in each of the six plane areas of the CRT. In particular, the product  $kN$  determines the fraction of crystal signal which must be added to the detector position. This fraction is fixed for a specific plane and will not apply to any other plane because of the different relationship between source, detector and scintillator positions for the six planes. As an example, let us consider two separate cases in which the same arithmetic for locating the activity distribution in one plane is first applied to a point source lying in the plane of interest and then to an adjacent plane. As shown in Figure 2.7 the scanning head is illustrated moving from left to right and

the six focal planes designated A-F. At the initial position the camera brings the center of the collimator to the edge of the scanned area. The source, indicated by the dot, will be imaged at one side of the crystal, due to the focussing holes, producing a maximum  $X_c$  signal which will be arbitrarily designated as +10. As viewed from the top, the event will illuminate the extreme right edge of the crystal. Some time later the detector will move relative to the source and the scintillation will occur in the crystal closer to its center, reducing for example the signal to +5. By appropriate arithmetic manipulation, the camera and detector movement positional signals can be combined to give the same net result  $X$  in the readout. In the arithmetic manipulation shown in Figure 2.7 a constant final positional signal of 5 units is obtained for varying camera and detector head signals. In the equations the fixed fraction  $kN$  of the camera signal, in this case  $1/2$ , was added to the detector signal  $X_d$ . Further movement of the detector relative to the point source will bring the collimator axis directly over the source ( $X_d=5$ ) then the displacement signal  $X_c$  is zero. The relevant arithmetic for each stage is shown at the bottom of Figure 2.7.

Figure 2.8 illustrates the situation when the same arithmetic for locating activity in plane A is applied to a source located in plane B vertically below the former position. Initially the source is not visualized at all, and throughout the scan the value of  $X$  is different depending upon the position of the detector relative to the

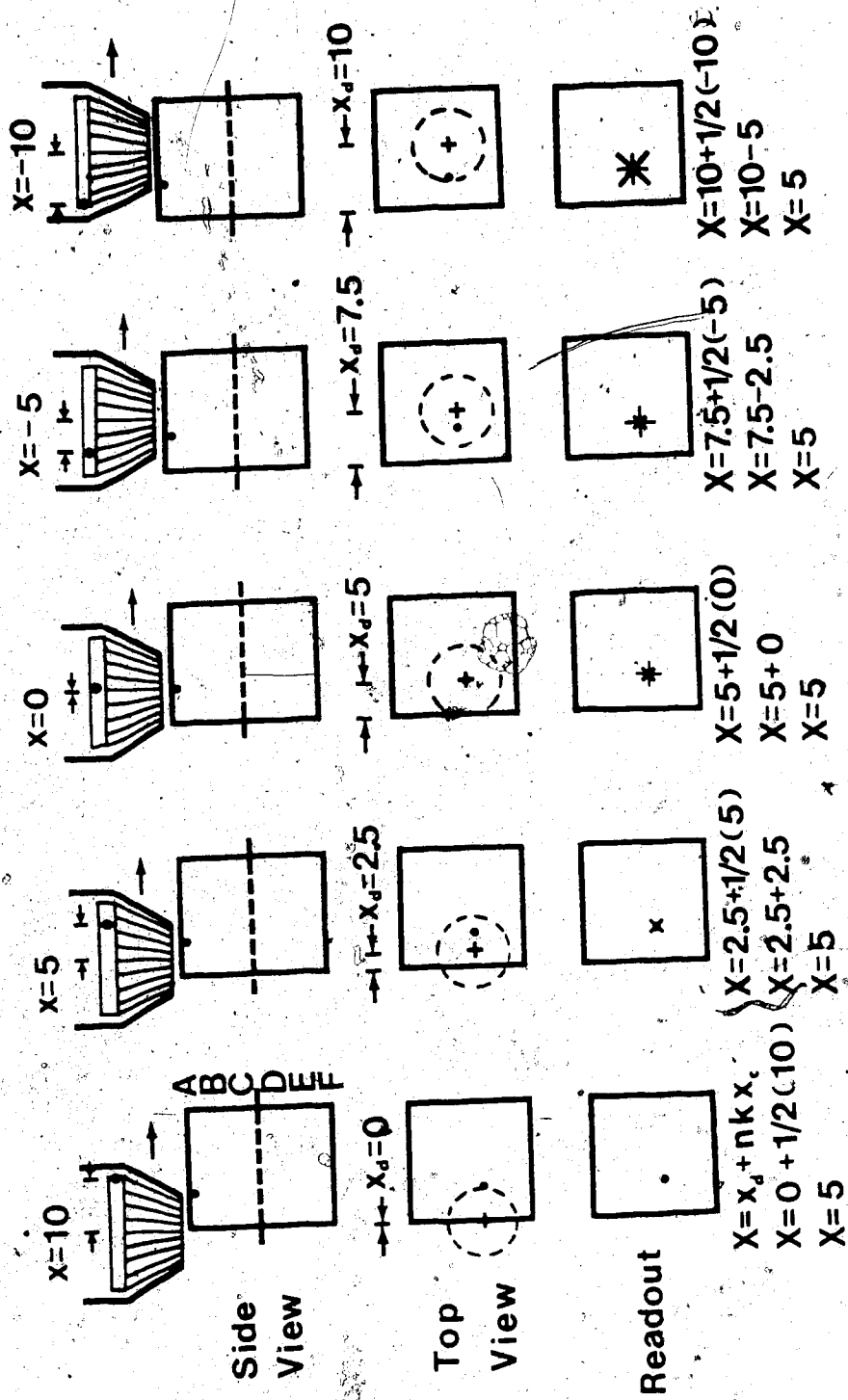


Fig. 2.7 One dimensional Pho/Con readout for plane A with a source in

plane A. (After L.S. Graham, V. Perez-Mendez, Nuclear Medicine

Physics, Instrumentation and Agents. Edited by F.R. Rollo

p. 277 (1977))

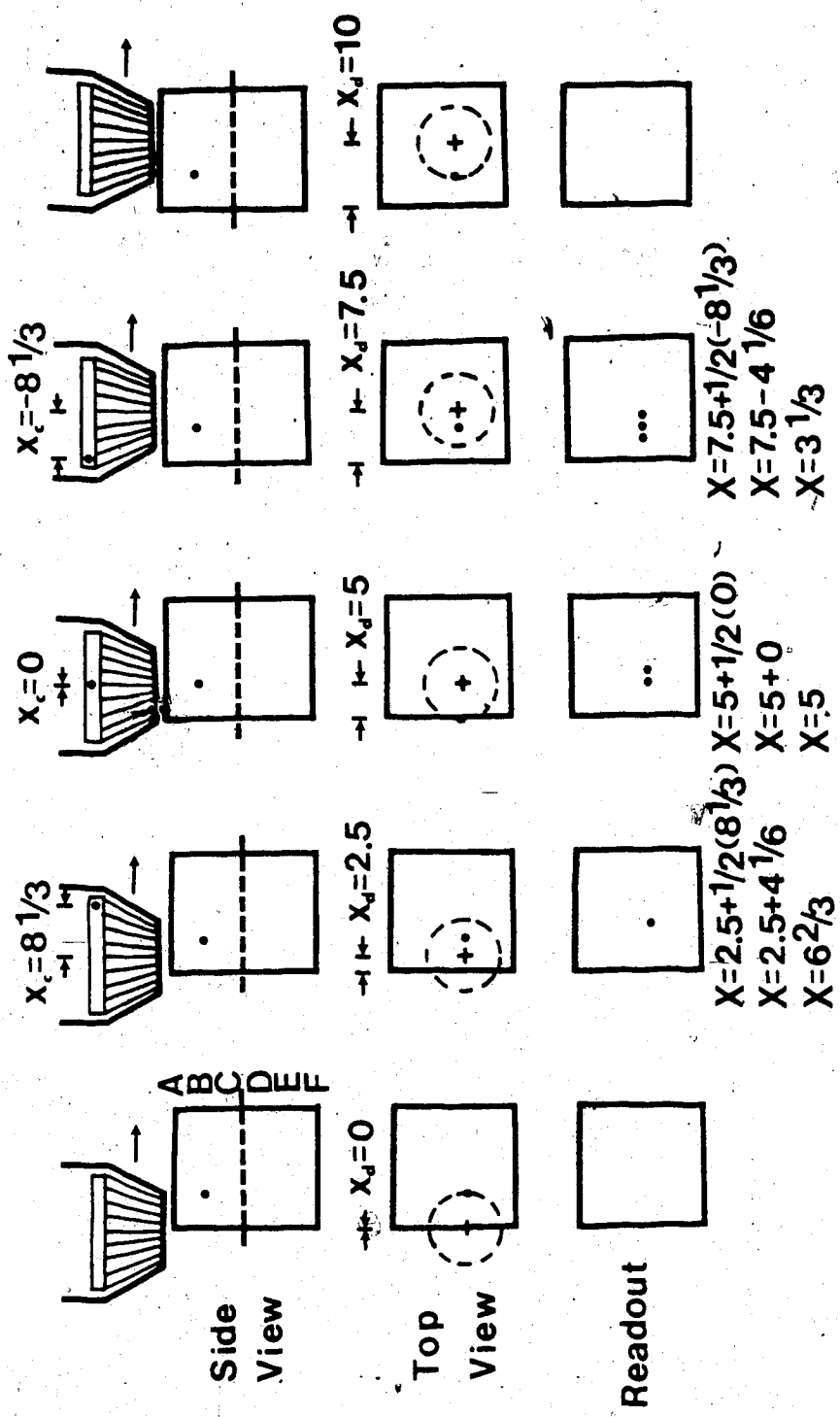


Fig. 2.8 Pho/Con imaging of a source out of plane by applying the

plane A arithmetic. (After L.S. Graham, V. Perez-Mendez, Nuclear Medicine Physics, Instrumentation and Agents. Edited by F.D. Rollo p. 278 (1977))

source. This variation in  $X$  gives rise to a blurring of all but those sources in plane A, and consequently only plane A is correctly imaged for that arithmetic. Figures 2.7 and 2.8 portray the process of image formation in one dimension, although the actual process is two dimensional. This so called blurring effect is demonstrated in Figure 2.9, obtained by scanning a point source in air. The six images shown represent the six focal planes of the Pho/Con lower detector which for displaying purposes have been cut from the original film and reassembled to demonstrate their depth dependence. Only the second image appears to be sharply in focus while the remaining are smeared over an area which increases in proportion to the distance from the plane of interest. The finite size of the point source image is due to the finite system resolution and smearing introduced by the microdot imager. The hexagonal pattern noticeable in the blurred images results from the characteristic detector position matrix and the reconstruction properties of the Pho/Con.

The total system operation is considerably more complex than it appears in this brief preliminary discussion, intended only to clarify some aspects of the Pho/Con operation. An understanding of the basic principles of focal plane tomography is essential for the study of the Pho/Con physical characteristics. In describing the basic operation of the system we often use terms such as detection of  $\gamma$ -rays, energy window, pulse height analyzer, depth



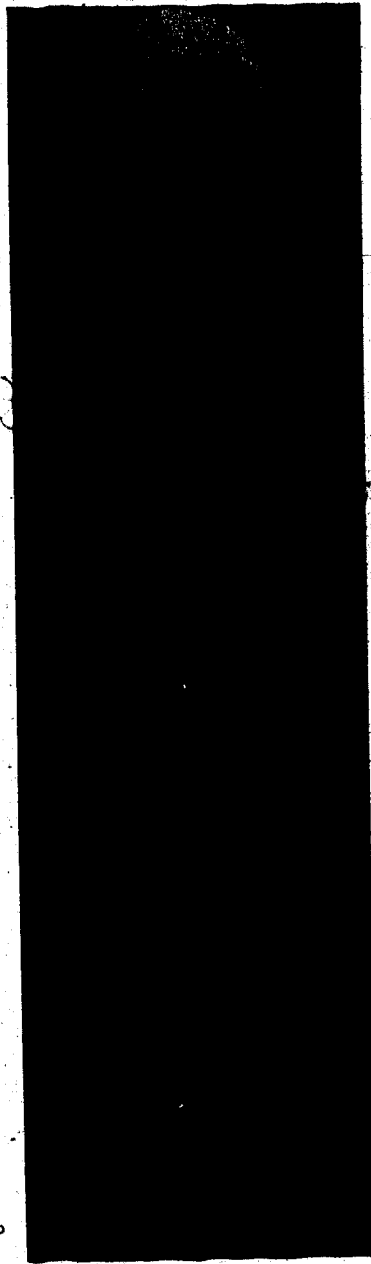


Fig. 2.9 Image of a 2 mm diameter Co-57 point source  
obtained with the system microdot imager.

response, sensitivity, resolving distance etc.. These quantities determine a set of measurable physical parameters which in turn establish the quality and the limitation of the system. In the following chapter an attempt will be made to quantitatively define these parameters, differentiating between physical properties affecting the detector and those which affect the system as a whole.

These parameters are summarized as follows:

1. Uniformity (detector)
2. Sensitivity (detector)
3. Linearity (detector and system)
4. Resolution
  - a. spatial (detector and system)
  - b. energy
  - c. temporal

## CHAPTER 3

### 3.1 Pho/Con: System components

The main components in the Anger tomographic scanner are the collimator, gamma camera and image display console (Microdot Imager). As discussed in Chapter 2, the combination of the properties of the collimator and gamma camera allows the Pho/Con to perform single photon tomography using the system analogue signals. In the following few sections, the investigation of the Pho/Con components will be confined to the collimator and the gamma camera. In the case of the microdot imager which produces the final analogue images, the difficulty in accessing the required signals prevents a detailed analysis of the device with a view to establishing the effect that this device has on the Pho/Con output. The Microdot consists of a CRT tube in which the electron beam is controlled using electromagnetic deflection coils. An intensity switch allows control of the film exposure, which can be balanced with a potentiometer, therefore normalizing the CRT output to a reference voltage. For each dial setting the light output of the CRT is constant. The images can accept two cassette sizes, 8cmx10cm and 11cmx14cm.

From the brief discussion about the Pho/Con analogue reconstruction algorithm, in Chapter 2, it is evident that both the intrinsic properties of the collimator and gamma

camera play a role in the reconstruction of the tomographic images, in that their combined properties affect the system response to a point source which is used to describe the algorithm. The point source response function can be used to predict the system response to any type of input function. Clearly, the system response to an impulse input depends on the collimator and position sensitive detector of the device. Thus, it appears that an understanding of these two basic components is important in establishing the potential and limitations of the Pho/Con for digital work.

### 3.2 Collimators

The Pho/Con employs a variety of multi-hole focussed collimators which can accommodate photon energies up to 550 KeV. The geometric characteristics of the collimators vary according to the energy rating. This in turn determines the septal thickness and consequently the size and number of holes. Optimal sensitivity and resolution are achieved with circular holes by distributing them in an hexagonal array.

In addition to their physical dimensions, focussed collimators can be characterized by their sensitivity and resolution; parameters which affect the imaging time and the quality of the image. Table IV summarizes the physical characteristics together with measured sensitivity and resolution values for the three collimators provided with the early Pho/Con models.

TABLE IV: Pho/Con collimators: Physical Characteristics

Collimator	Focal Depth (cm)	No. of Holes	Coronal Resolut'n at focal depth (cm)	Relative Sens'ity	Geometric Efficiency (cm <sup>2</sup> )
Low Energy (150 Kev)	8.9	397	1.0	1	0.0148
Med. Energy (380 Kev)	8.9	253	1.0	0.58	0.0096
High Energy	8.9	55	1.5	-	0.0106

### 3.2.1 Sensitivity

The collimator sensitivity can be defined as the ratio of the number of counts reaching the detector per unit time to the number of events per unit time emitted by the source. Collimator sensitivity values can be obtained from measurements using a known amount of activity in the point source or by measurements using a plane source with a known specific activity. The collimator response to a point source is a position sensitive measurement which depends on the solid angle subtended by the collimator at the location of the source. In the case of multichannel focussed collimators, measurements of plane sensitivity are preferable since these are related to the geometric characteristics of the collimator itself. Plane source efficiency represents the number of events emitted from an infinite plane source lying perpendicular to the collimator

axis and interacting with the crystal after passing through the collimator holes. For the focussed collimator shown in Figure 3.1 the geometrical efficiency G is given by (Beck R. N.1968)

$$G = \frac{N d_1^4}{64 F^2} \left(1 + \frac{F}{L}\right)^2 \quad [\text{cm}^2]$$

where F is the focal length, L the collimator thickness,  $d_1$  the diameter of the central hole at the entrance, and N the number of collimator holes. G is independent of the distance between the collimator and the plane of activity provided that the source covers the entire field of view of the collimator. Under this condition, the solid angle subtended by the collimator remains constant. The plane sensitivity of the Pho/Con detector is obtained by combining the collimator efficiency G with crystal detection efficiency E, a term which is affected by the photon energy and crystal thickness.

The plane-source sensitivity, expressed in Becquerels per square centimeter (Bq/cm<sup>2</sup>), represents the mean count density averaged over the detector field of view (Hine et al 1978). A depth dependent quantity, the field of view represents the maximum source area viewed by the detector at a predefined distance from the collimator.

The expected count rate R, at the focal distance, can be estimated from the following expression,

$$R = 3.7 \times 10 \text{ SWEG (cps)}$$

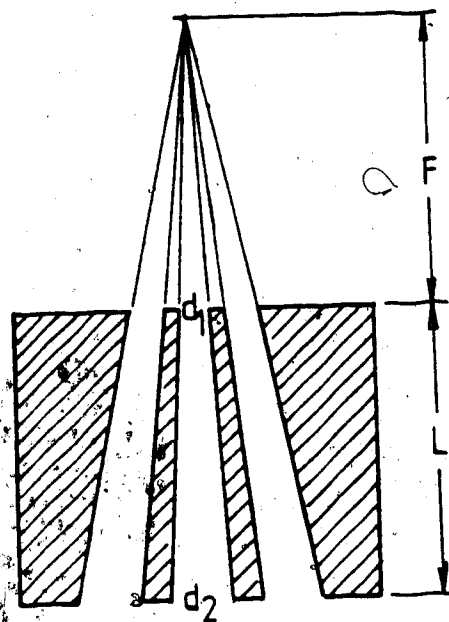


Fig. 3.1 Simplified diagram of a focussed multichannel collimator showing the parameters of interest; the central entrance hole, of diameter  $d_1$  and at exit  $d_2$ , the focal length  $F$ , and the collimator thickness  $L$ .

In this expression,  $S$  is the source specific activity in Bq/cm<sup>2</sup>,  $W$  is the window count-to-total count ratio,  $E$  the crystal intrinsic detection efficiency at a given energy and  $G$  the collimator geometrical efficiency. The calculated values of  $G$  for the low and medium energy collimators were then compared to measured count rates using a Co-57 flood source of known specific activity  $S$ . Values of  $W$  were measured for various energy window widths while crystal efficiency  $E$  was estimated from existing data (Anger et al 1964). For two of the Pho/Con collimators, the geometrical efficiency at the focal depth with the analyzer window at 15% was calculated at approximately 0.024 cm for the 150 KeV collimator and 0.014 cm for the 380 KeV. The discrepancy which exists between the calculated and measured value of  $G$  shown in Table IV can be attributed to the uncertainty in some of the parameters used in the calculation and to neglected secondary effects such as septal penetration, and scattered radiation.

### 3.1.1 Resolution

The resolution of a multichannel focussed collimator was determined from the point source response function which describes the change of the solid angle as a function of the relative source-collimator position. The point source response and collimator resolution are best displayed in the isocount plots which represent maps of equal detection



probability, or, more specifically, the probability that a photon will pass through the collimator holes and interact with the crystal. The width and depth of the isocontour at 50% of the maximum count defines the lateral and longitudinal resolution diameter (Popovic et al 1968).

The longitudinal response curves for the low and medium energy collimators were initially measured using a source detector configuration as indicated in Figure 3.2. The count profile shown in Figure 3.3 was obtained by moving the point source along the collimator axis and recording the number of detected events with a digital ratemeter. The profile shown displays a maximum peak value at the geometrical focal point. From this curve it was possible to determine the position, with respect to the collimators, of the various sensitivity levels with the 100% level at the focal depth. Lateral response curves for a point source position on either side of the focal depth were obtained by moving the source normally to the collimator axis. Figure 3.4 shows the lateral response curves of the PMO/Con upper detector obtained using the medium energy collimator and a Co-57 point source positioned at various distances beyond the focal depth. These curves were then used to determine the region in space of equal photon detection probability. Figures 3.5 and 3.6 show the isoresponse curves in air obtained with the 150 KeV and 380 KeV collimators with a reported resolution at the focal depth of 1.0 cm. The lateral resolution diameter at the focal distance is given by the width of the 50% isoresponse curve.

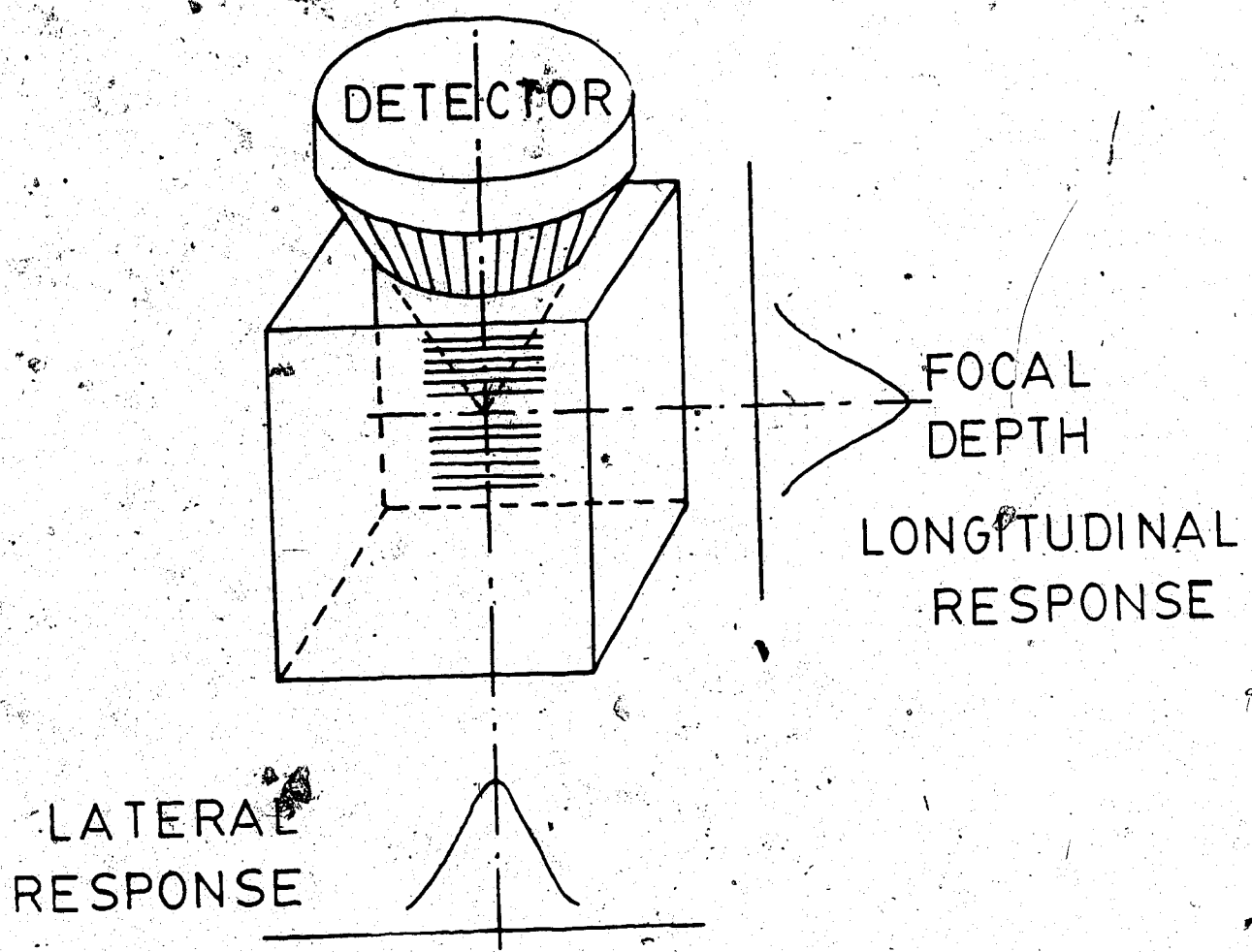


Fig. 3.2 Schematic arrangement used to measure the isoresponse curve of the Pho/Con collimator. The point source is moved along predetermined longitudinal response lines yielding the lateral response curves.

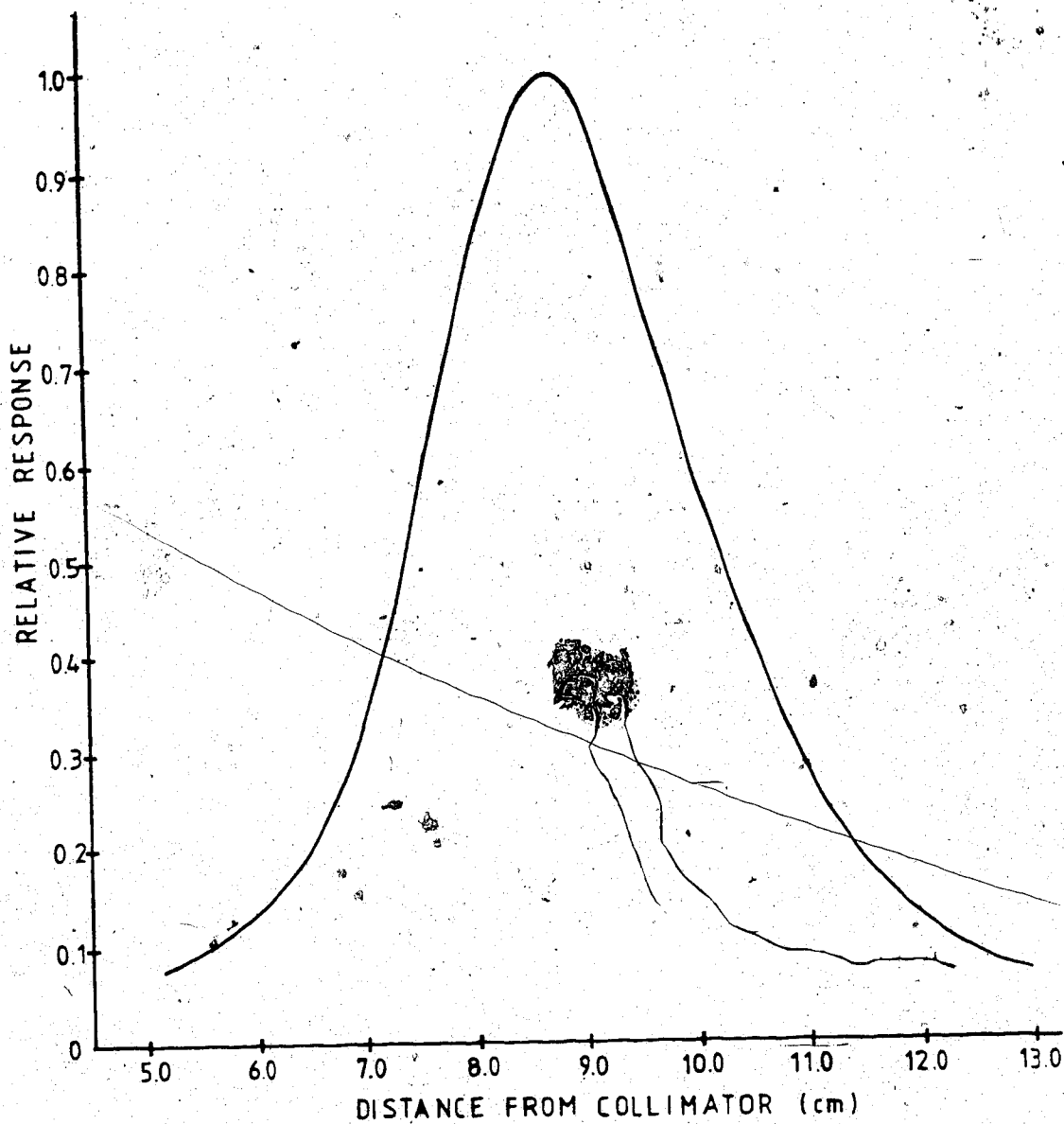


Fig. 3.3 Longitudinal response to a point source, in air, displaced along the collimator axis. The curve is characteristic of the 380 KeV 10 mm resolution focussed collimator.

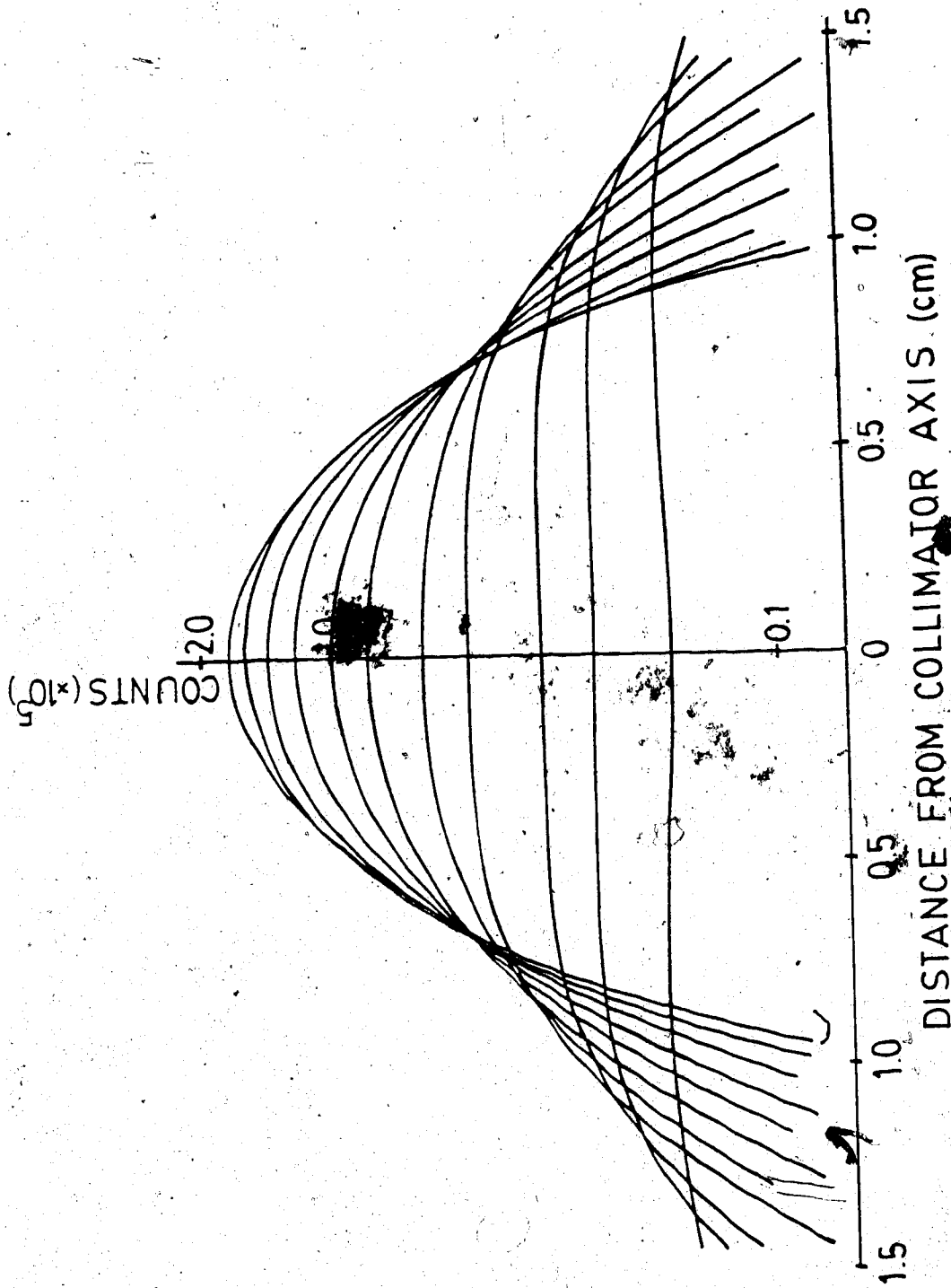


Fig. 3.4 Lateral response to a point source in air for the 380 KeV 10 mm resolution Pho/Con Collimator. These curves were obtained with the source positioned within the focal depth.

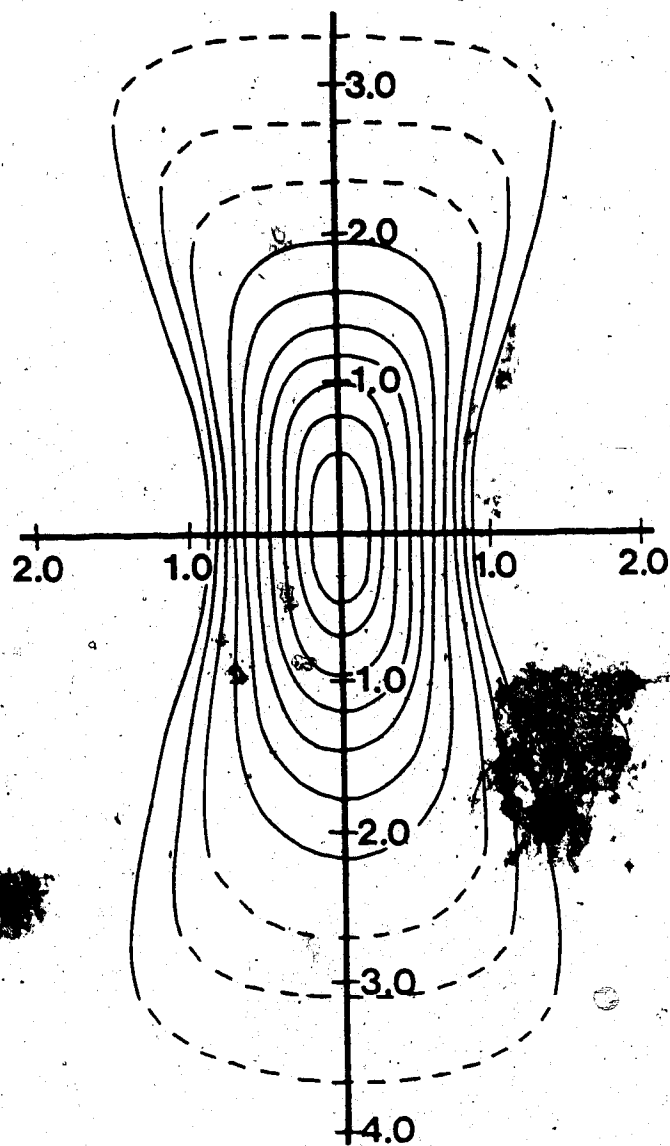


Fig. 3.5 Isocount contour, in air, for the 150 KeV 10 mm resolution focussed collimator. The curves, starting from the outer one, are: 10, 15, 20, 30, 40, 50, 60, 70, 80, 90% of the maximum count rate measured at the focal point.

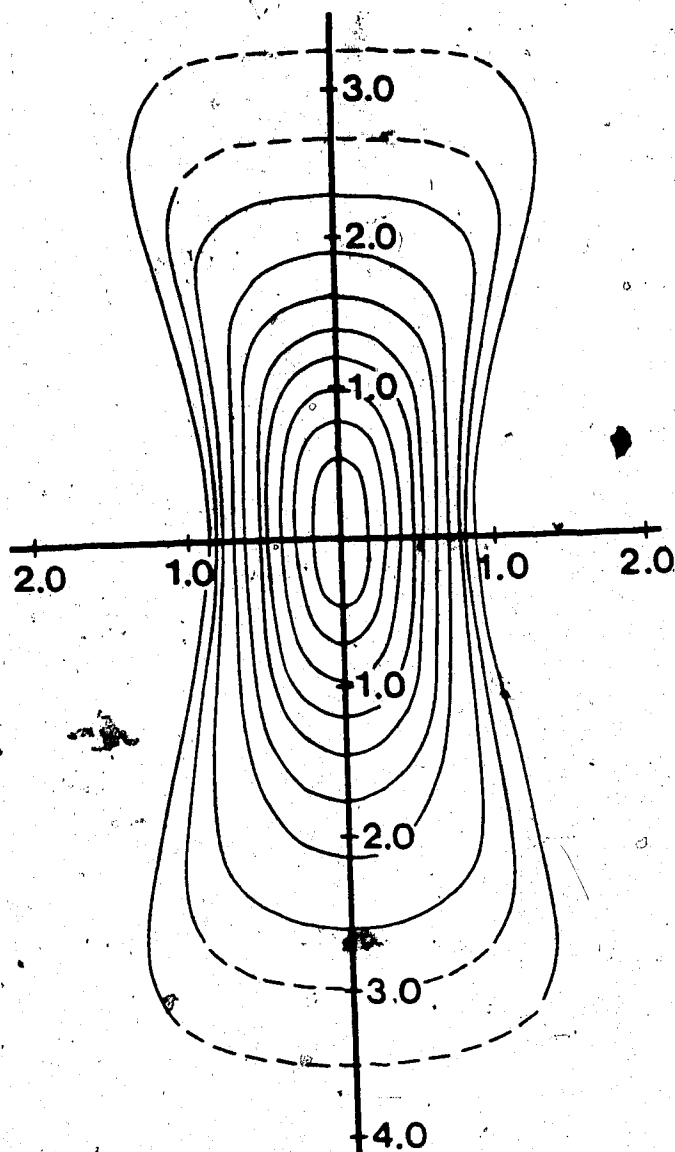


Fig. 5.6 Isocount contour, in air, for the 380 KeV 10 mm resolution focussed collimator. The isoreponse curves, starting from the outer one, are: 10, 15, 20, 30, 40, 50, 60, 70, 80, 90% of the maximum count rate.

The measured resolution values for the low and medium energy collimators were 1.1 and 1.0 cm respectively. The depth resolution was measured at 2.8 cm with a slightly poorer value for the low energy collimator possibly due to septal penetration. In the above curves, the dotted portion of the lines represents the estimated segment of the contour due to lack of data points. The isoresponse curves for the 380 KeV collimator are shown in Figure 3.7 with the source placed within a tank of water. The collimator focal point was located at a depth of 8 cm in water. Measurements of the isoresponse curves performed using the above procedure yield plots which are distorted compared to the equivalent curves measured in air. These distortions are due to the loss of photons caused by attenuation, and the resulting increased detection of scattered events. Attenuation tends to remove events from the lower portion of the curves thus causing a displacement of the lines upwards while the scattered component tend to widen the curves in regions near the collimator. Figure 3.8 represents the same data corrected only for attenuation. As shown, the scattered photons degrade the lateral and longitudinal resolution diameters to 1.3 and 3.3 cm respectively.

The theoretical expression of the resolution of a focussed collimator, as given by Anger (1968), represents the vector sum of two components

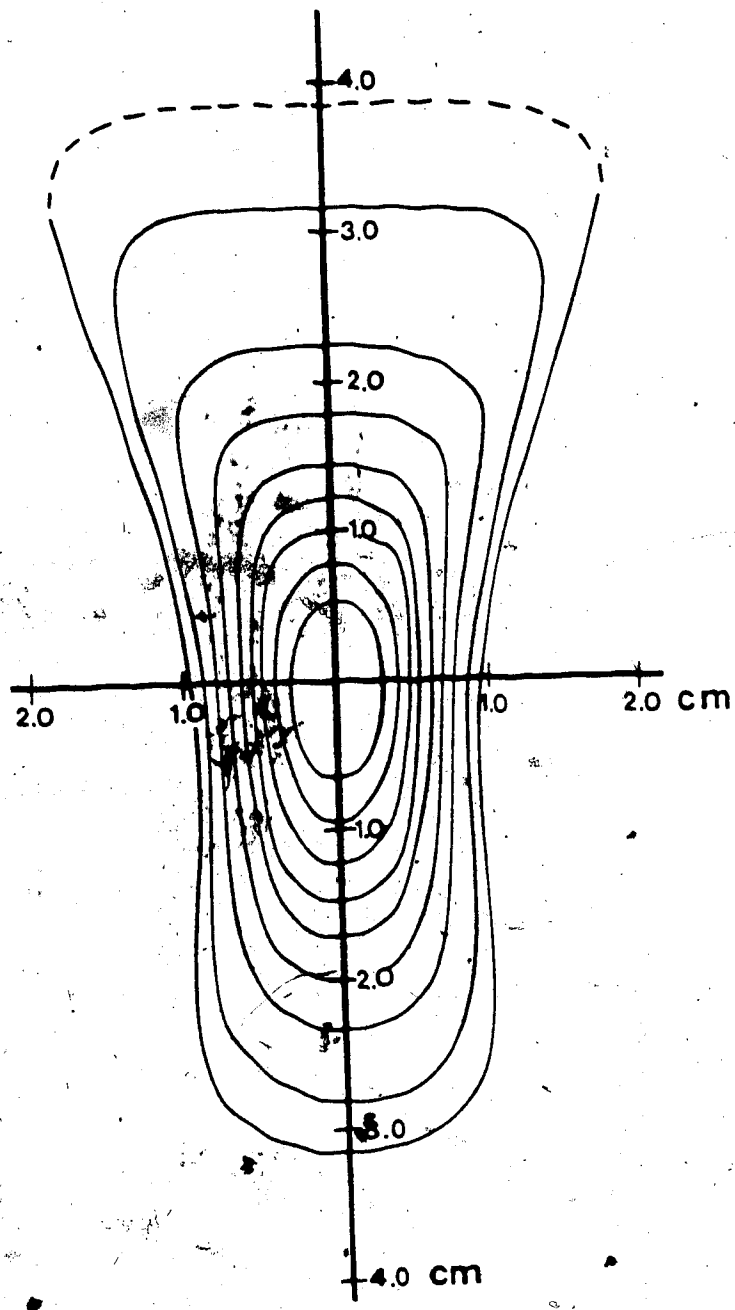


Fig. 3.7 Isocount contour for 380 KeV, 10 mm resolution focussed collimator measured with the source in water. The isoresponse curves are 15, 10, 30, 40, 50, 60, 70, 80, 90% of maximum count.



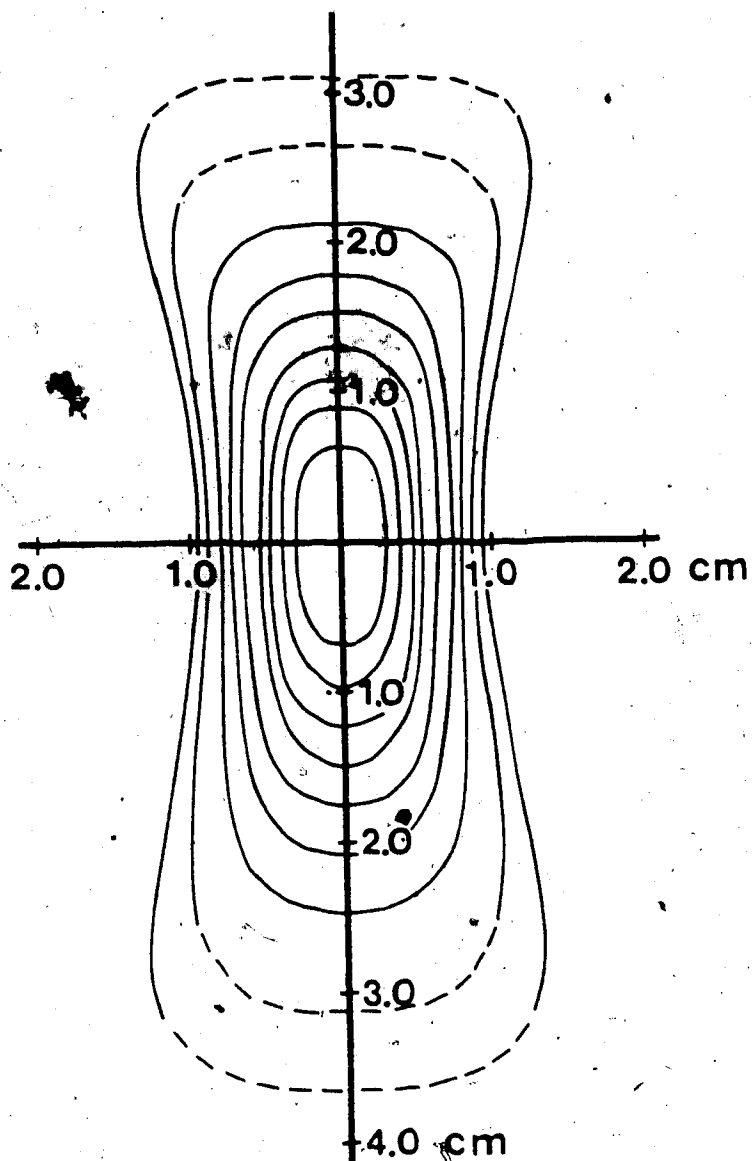


Fig. 3.8 Isocount contour for the 380 keV 10 mm resolution focussed collimator corrected for attenuation. The plotted isocount curves are 15, 20, 30, 40, 50, 60, 70, 80, 90% of maximum count rate.

$$r_{\text{coll}}^2 = r_c^2 + r_p^2$$

where  $r_c$  represents the resolution component associated the collimator central hole and  $r_p$  the parallax fraction due to all the collimator holes. For the central hole with diameters  $d_1$  and  $d_2$  at the source and crystal sides respectively, the resolution is given by

$$r_c = d_1 + b \frac{d_1}{L} \quad b \leq f$$

$$r_c = b \frac{d_2}{L} \quad b \geq f$$

where  $f$  represents the focal distance of the central hole, which in this case is equal to the collimator focal distance  $F$ , and  $b$  is the collimator to source separation. parallax component is given by the following expression:

$$r_p = \sqrt{2} |F - b| \tan \frac{\alpha}{2}$$

where  $\alpha$  is the acceptance angle defined by the intersection of the outer collimator hole axis as indicated in Figure 3.2. The experimental measurement of collimator resolution includes the degradation due to the intrinsic resolution of the scintillation detector, thus yielding the total resolution of the gamma camera and collimator. The intrinsic resolution  $r_i$  of the gamma camera adds to the

total resolution according to the following expression,

$$R_o^2 = r_c^2 + r_p^2 + r_e^2$$

The value of  $r_e$  is related to the camera intrinsic resolution by the relation (Anger H.O. 1968)

$$r_e = r_i \frac{|F-b|}{F + L + c}$$

where  $c$  represents the distance between the exit side of the collimator to the plane of interaction in the crystal and  $L$  represents the height of the collimator.

Figure 3.9 shows the resolving distance for the low and medium energy collimator as calculated using the above expressions, compared to the measured collimator characteristics. The data points are values of the resolution for the medium energy collimator obtained from the FWHM of the lateral response curves measured at various distances from the focal plane. The deviation from the calculated total resolution  $R_o$ , appears to increase with increasing source-to-focal plane separation.

### 3.2 Gamma camera

The Pho/Con scintillation camera consists of a NaI(Tl) crystal of 21.6 cm diameter and a thickness of 2.5 cm. In the Pho/Con presently used at the Cross Cancer Institute the

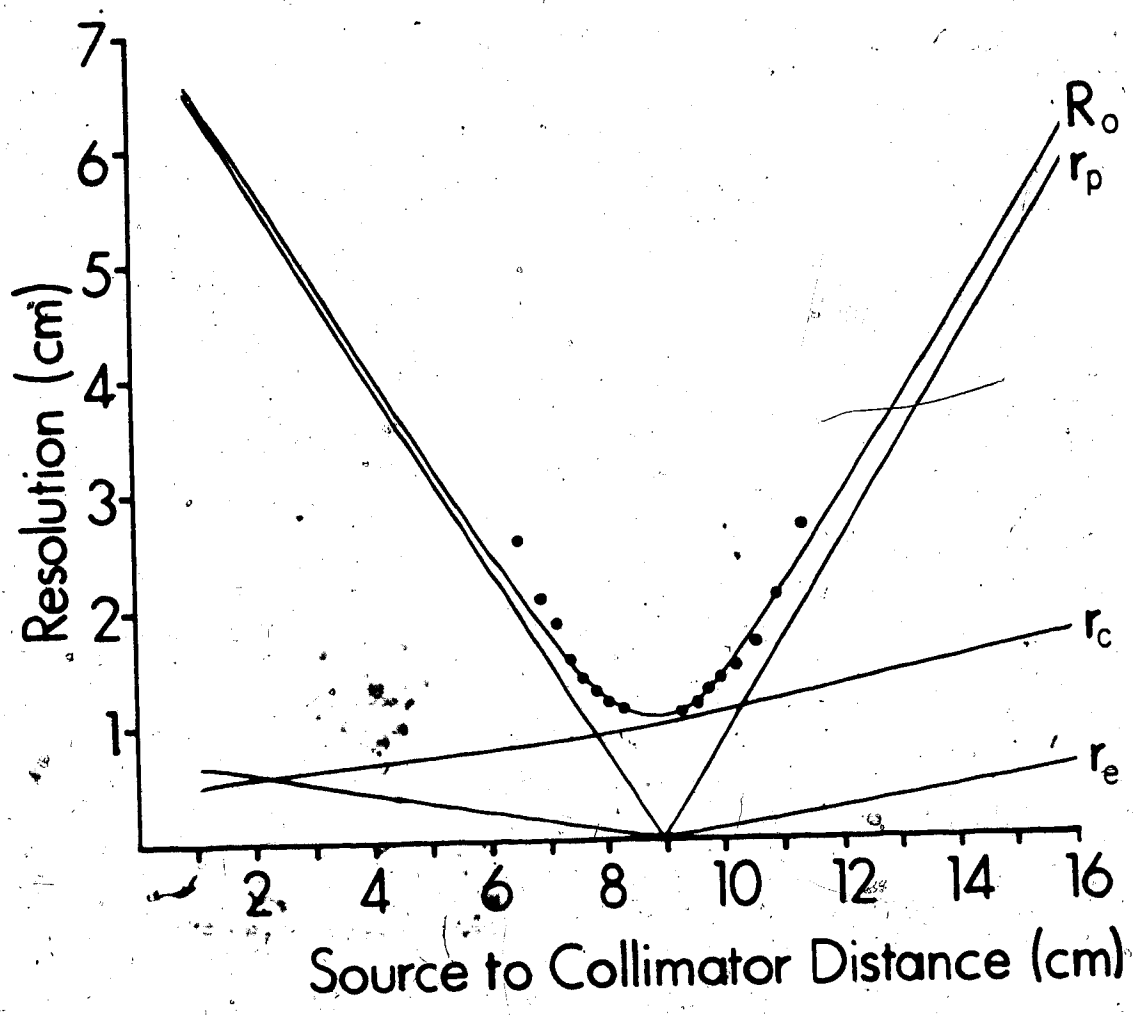


Fig. 3.9 Calculated resolution parameters for the Pho/Con medium energy focussed collimator as a function of source-to-collimator distance.  $R_o^2 = r_c^2 + r_p^2 + r_e^2$  represents the total resolution,  $r_c$  the channel component and  $r_p$  the collimator parallax contribution,  $r_e$  is the resolution component due to the crystal resolving distance. The data points are measured values for  $R_o$ .

crystal is viewed by seven photomultiplier (PM) tubes arranged in a hexagonal configuration, identical to the one shown in Chapter 2. The signal from the PM tubes is processed by standard camera electronics to give position and energy information for each detected event. In the Pho/Con operation, the scintillation position, in the crystal  $(X_i, Y_i)$  is combined to the detector position  $(X_e, Y_e)$  to produce the twelve tomographic images, six for each detector, by a simple back-projection reconstruction algorithm implemented by the system, using analogue signals. Each image represents the plane of activity at a predefined depth  $D$ , and identified by the coordinate equations defined earlier. The quality of the output images depends on the ability of the system to accurately identify and reproduce the location of each event. The fraction of the camera signal that contributes to the positioning of an event is determined by the ratio  $D/F$ , where  $F$  represents the collimator focal distance. Another parameter which affects the quality of the image is the energy resolution, which depends on the crystal thickness and the efficiency of light collection by the PM tubes following the interaction of a photon with the crystal. Good energy discrimination allows rejection of unwanted scattered radiation which tends to degrade the spatial resolution of the system. Thus, knowledge of the camera performance can help to identify system limitations which can be attributed to the scintillation detector.

### 3.2.1 Spatial linearity

Spatial linearity defines the ability of an imaging device to accurately reproduce the geometrical dimensions of a line source or an array of linear sources of activity (Hine et al 1978). In general, images obtained with rectilinear scanners are less likely to be affected by spatial distortion than their counterparts obtained with gamma cameras. In the case of the Pho/Con multiplane tomographic scanner, distortion might be expected to be associated with the detector gamma camera. This distortion could affect not only the linearity of the system, but also affect the reconstruction algorithm and for this reason should be investigated.

Experimentally, the spatial linearity of the detectors was measured with the collimator removed. A well collimated source was moved in front of the detector through a grid with 2.5 cm spacing, and adjustable orientation from 0 - 180 degrees. Figures 3.10 and 3.11 represent the calibration curves obtained for the Pho/Con using the X- and Y-position signals. Each graph was obtained by routing the camera signal into a multichannel analyzer (MCA), where the peak, constituting a voltage amplitude distribution, represents the location of the radioactive source. As shown in both figures a loss of linearity occurs towards the outer part of the crystal. The central region of the various curves were used to convert the peak position, from MCA channels, into centimeters. A plot of measured peak

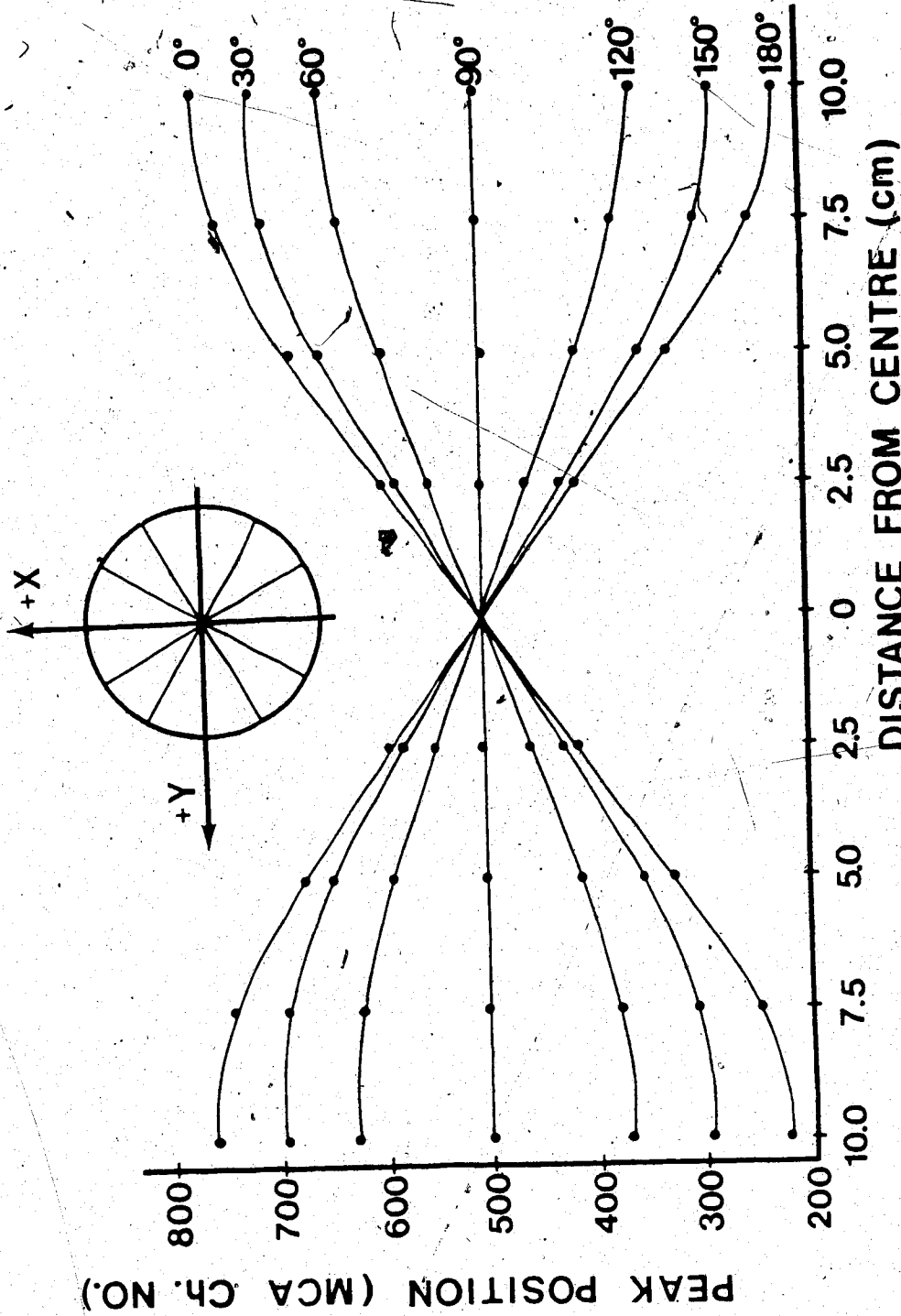


Fig. 3.10 Pho/Con probe spatial linearity expressed in MCA channel number and measured at angles varying from  $0^\circ$  to  $180^\circ$ . The curves shown were obtained using the camera x-position signal by moving the source along lines passing through the camera geometrical center as indicated in the insert.

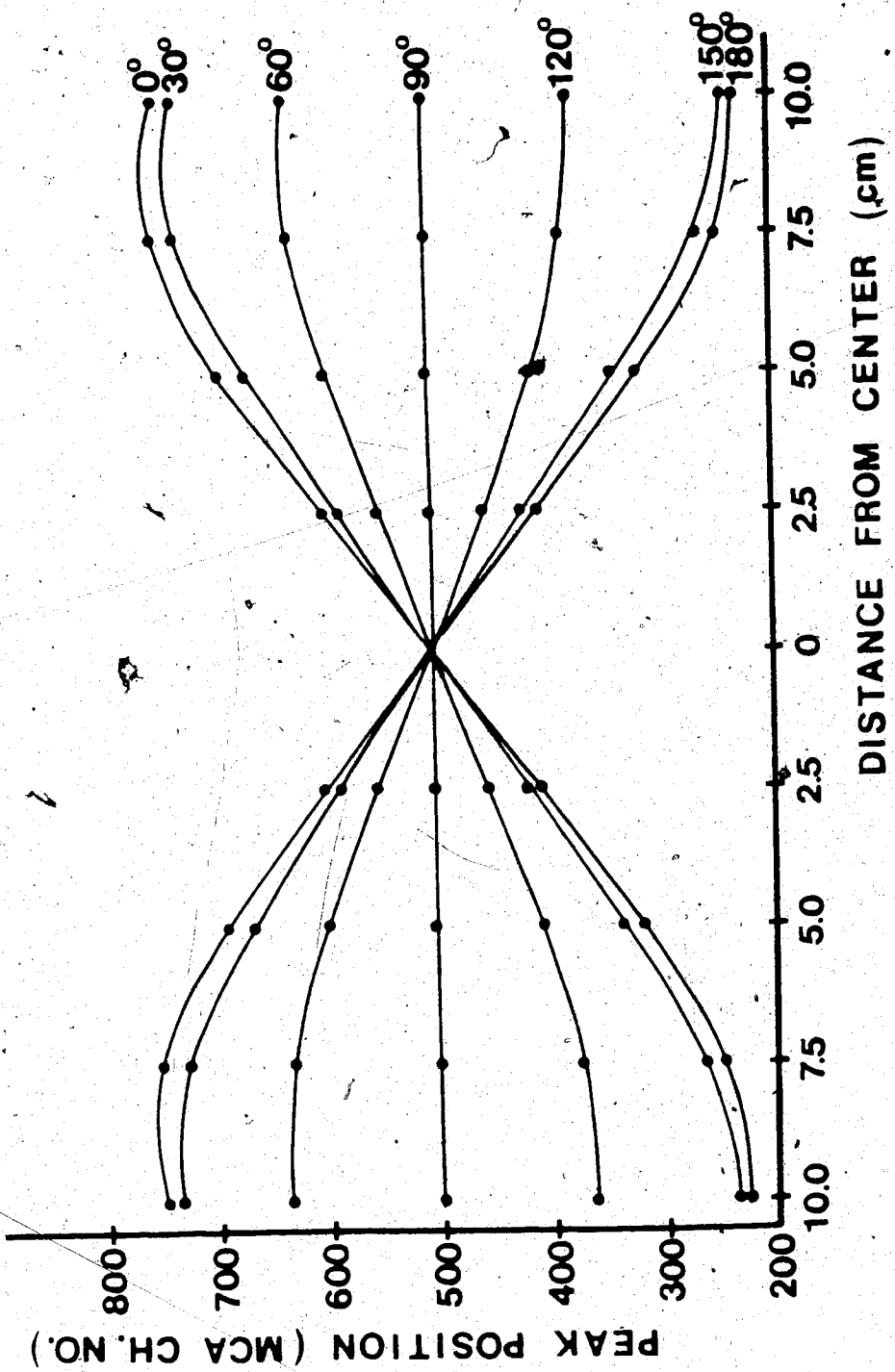


Fig. 3.11 Pho/Con camera spatial linearity measured with the y-position signal adopting the same procedure of Fig. 10.



position versus the true location of the source gives the detector spatial linearity. Figures 3.12 and 3.13 show the linearity profile for the upper detector coordinate signal. The line represents the least squares fit to the data points measured at 10.0 cm distance from the centre of the crystal. The linear fit is remarkably good over the central 15 cm with a correlation coefficient close to unity. The distortion occurring at the edges of the crystal, as shown in both Figures 3.12 and 3.13, tends to displace events falling near the edges of the crystal towards the center of the detector. This spatial distortion, due mainly to the crystal edge packing, results in large camera non-uniformities.

### 3.2.2 Uniformity

Uniformity is normally defined as the ability of an imaging device to reproduce accurately a uniform distribution of activity (Hine et al 1979). Camera head uniformity is traditionally determined from static images of a flood source by inspecting such images for changes in the film optical density; a method which gives only a qualitative measure of detector nonuniformity. It is, however, a common standard procedure in conventional gamma camera imaging used to monitor changes in system performance. For the Pho/Con this method of measuring

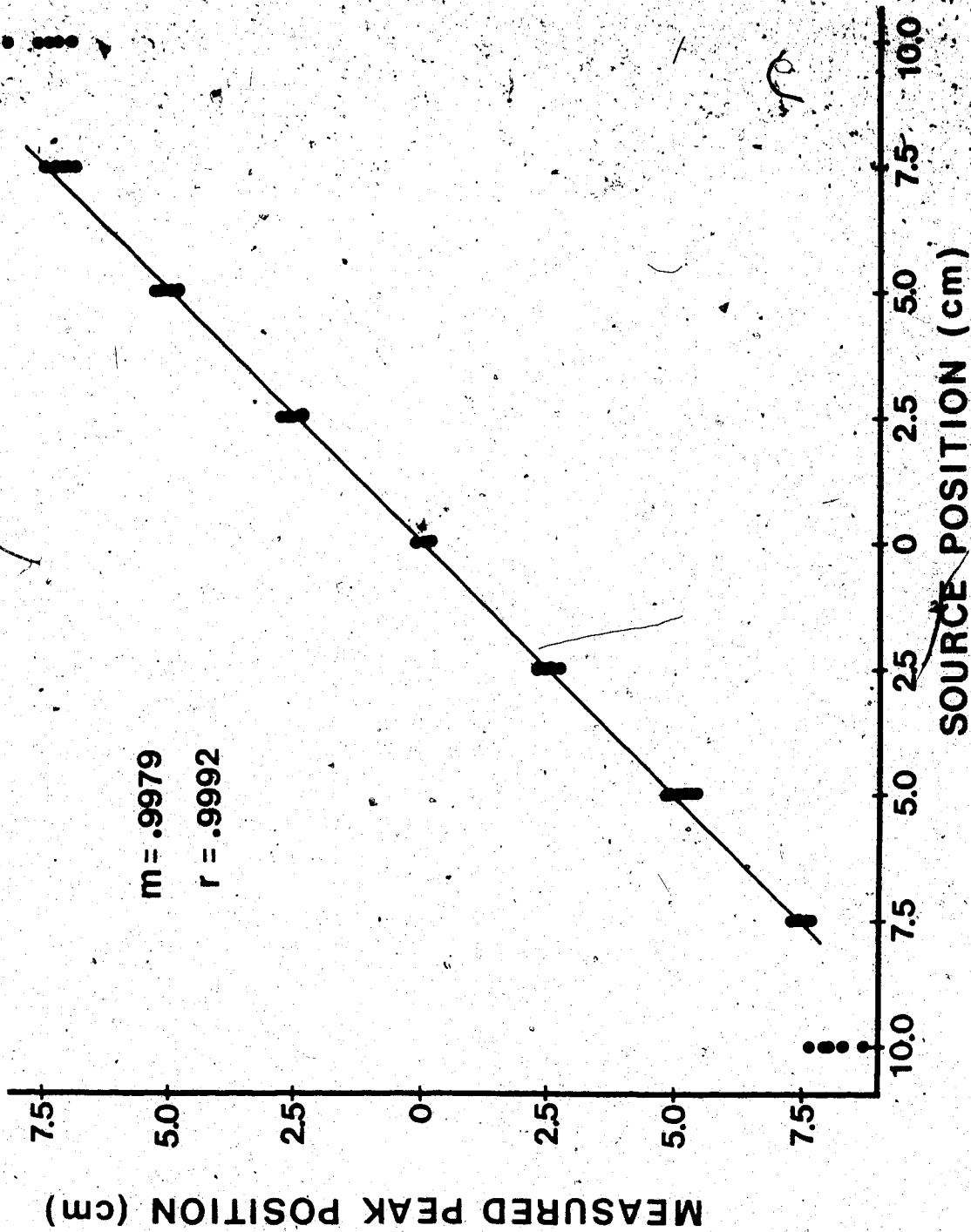


Fig. 3.12 Linearity of x-position signal measured at angles 0°, 30°, 60°, 120°, 150° relative to the camera x-coordinate axis. The solid line represents the least square fit to the measured MCA peak position in cm.

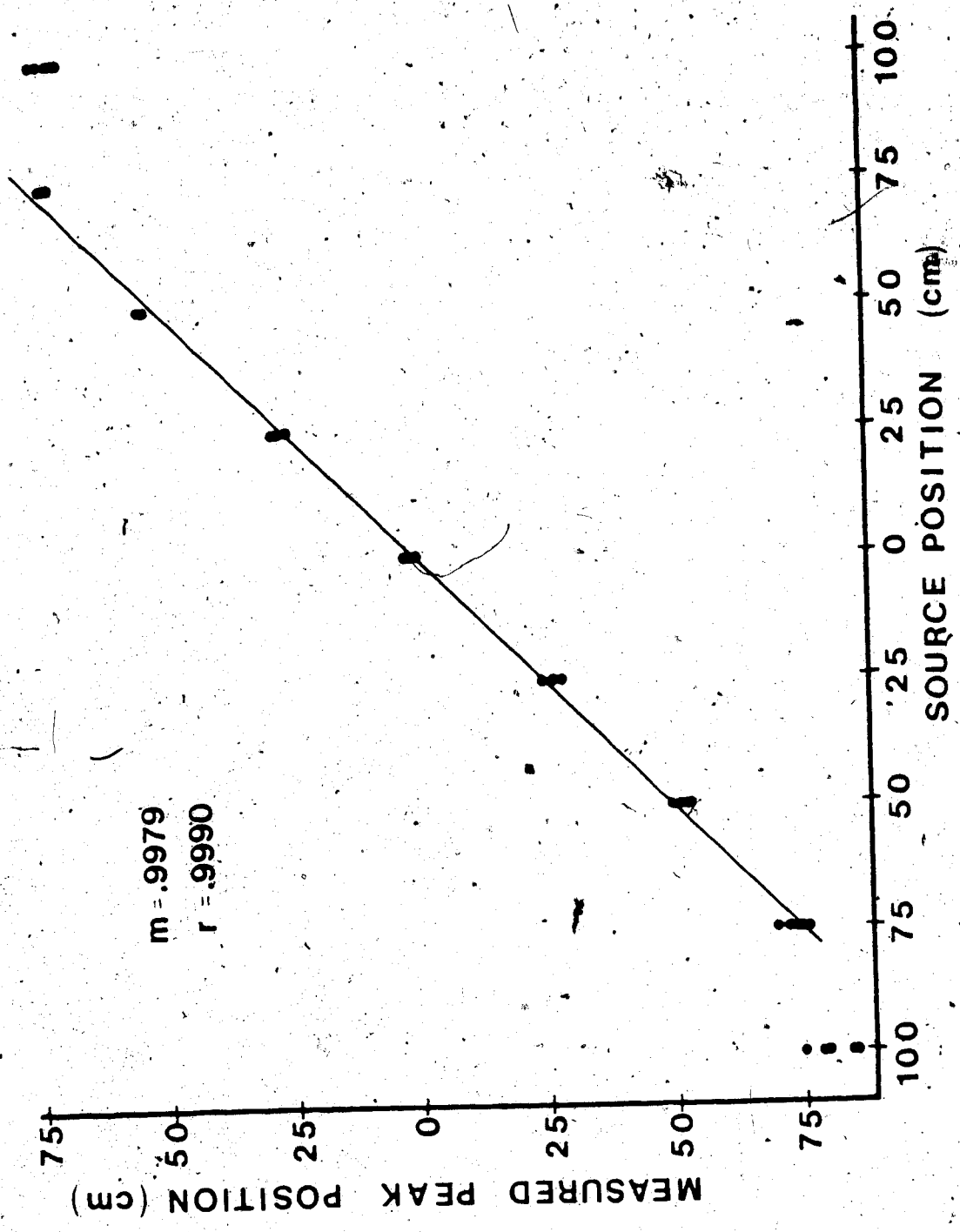


Fig. 3.15 Linearity of y-position signal measured at angles of  $0^\circ$ ,  $30^\circ$ ,  $60^\circ$ ,  $120^\circ$ ,  $150^\circ$  with respect to the camera y-coordinate axis.

non-uniformity is particularly subjective because of the minified images obtained from the microdot imager. Figure 3.14 shows flood images for one of the Pho/Con gamma cameras with and without collimator. In both cases the flood was obtained under normal scanning conditions with the detector motion disabled. As shown in Figure 3.14, there are easily identifiable regions of nonuniformity which result from the light reflector which surrounds the crystal edge. The hexagonal distortions appear to be particularly pronounced in the proximity of the photomultiplier tubes. As indicated from the linearity plots, lack of uniformity could be attributed to the spatial distortion due to the camera position matrix circuitry rather than local changes in sensitivity. The shape and size of the six images shown in Figure 3.14 are the result of both the position matrix and the reconstruction algorithm which reproduce the coordinate position (X, Y). The size of the six flood images represents the amount of crystal signal contributing to the event coordinate signal in the six focal planes.

Quantitatively, the crystal uniformity was evaluated using the detector position signals and obtaining profiles through the center of the crystal along the X and Y coordinate signals. Figure 3.15 shows the two profiles for the Pho/Con gamma camera with the collimator removed. These profiles were obtained by exposing the detector to a standard flood source, after shielding the detector with a lead mask with a 3mm wide aperture running parallel to the

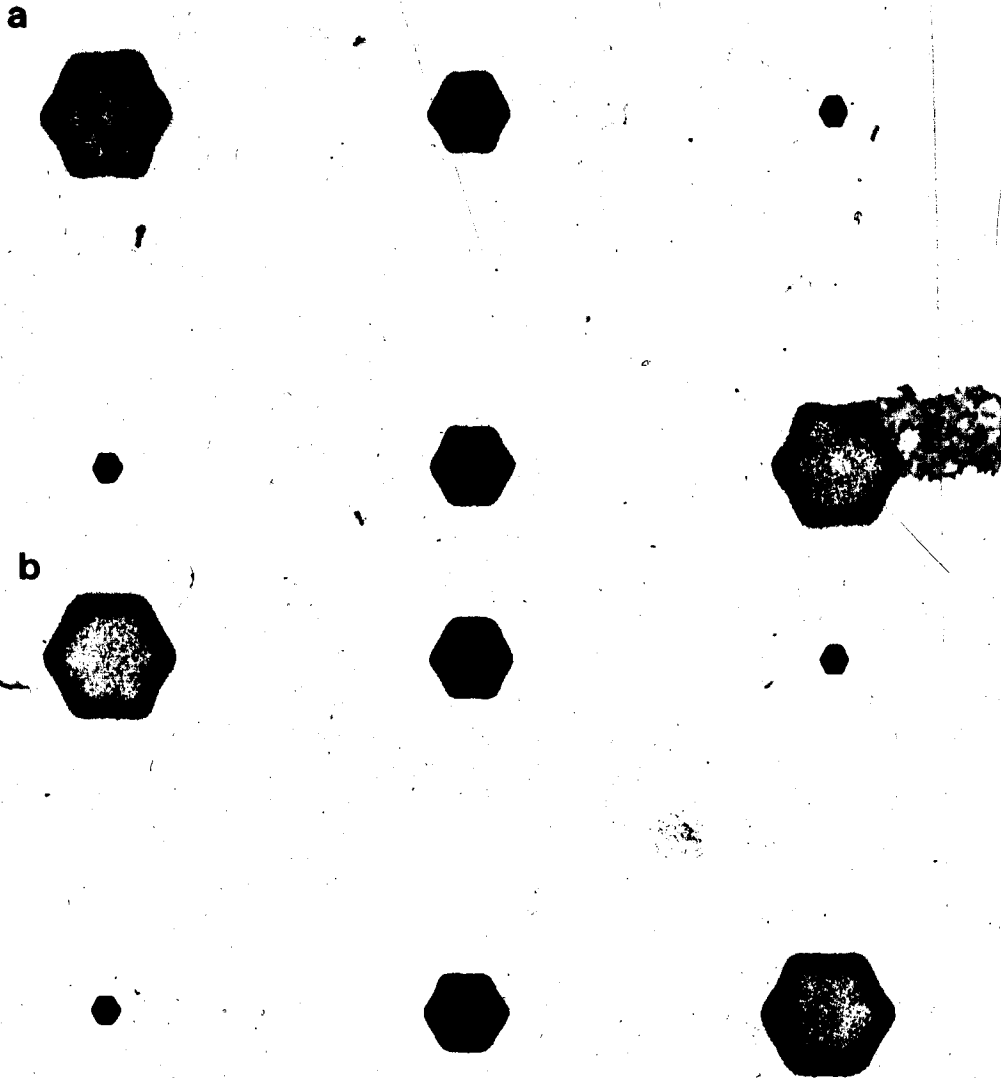


Fig. 3.14 Pho/Con detector flood field (a) with collimator,  
(b) without collimator.

crystal X and Y coordinates. Each of the profiles shown in Figure 3.15 represents a plot of a narrow slice of the two position-signals stored in the multichannel analyzer. As shown, the profiles confirm a strong edge packing effect, which results from the light reflector and PM tube arrangement with respect to the camera crystal. In both cases, the maximum count difference between the edges and the central area of the crystal is approximately 100%, which was calculated using the average count per MCA channel in the profile. The slight asymmetry in the profiles results from the inaccurate alignment of the 3 mm aperture along the two axis. The distortions in the gamma camera position signals have little effect on the intrinsic resolution of the gamma camera as shown below. The variation in uniformity and linearity applies only to the Pho/Con camera head and, as discussed later, has no effect on the system uniformity. The latter is characteristic of a scanning device.

### 3.2.3 Resolution

The gamma camera resolution parameters describe the intrinsic characteristics of the crystal, photomultiplier tubes and the electronic circuit; these are detector components which yield position and energy information. The combined performance of these elements within the gamma camera yields the following:

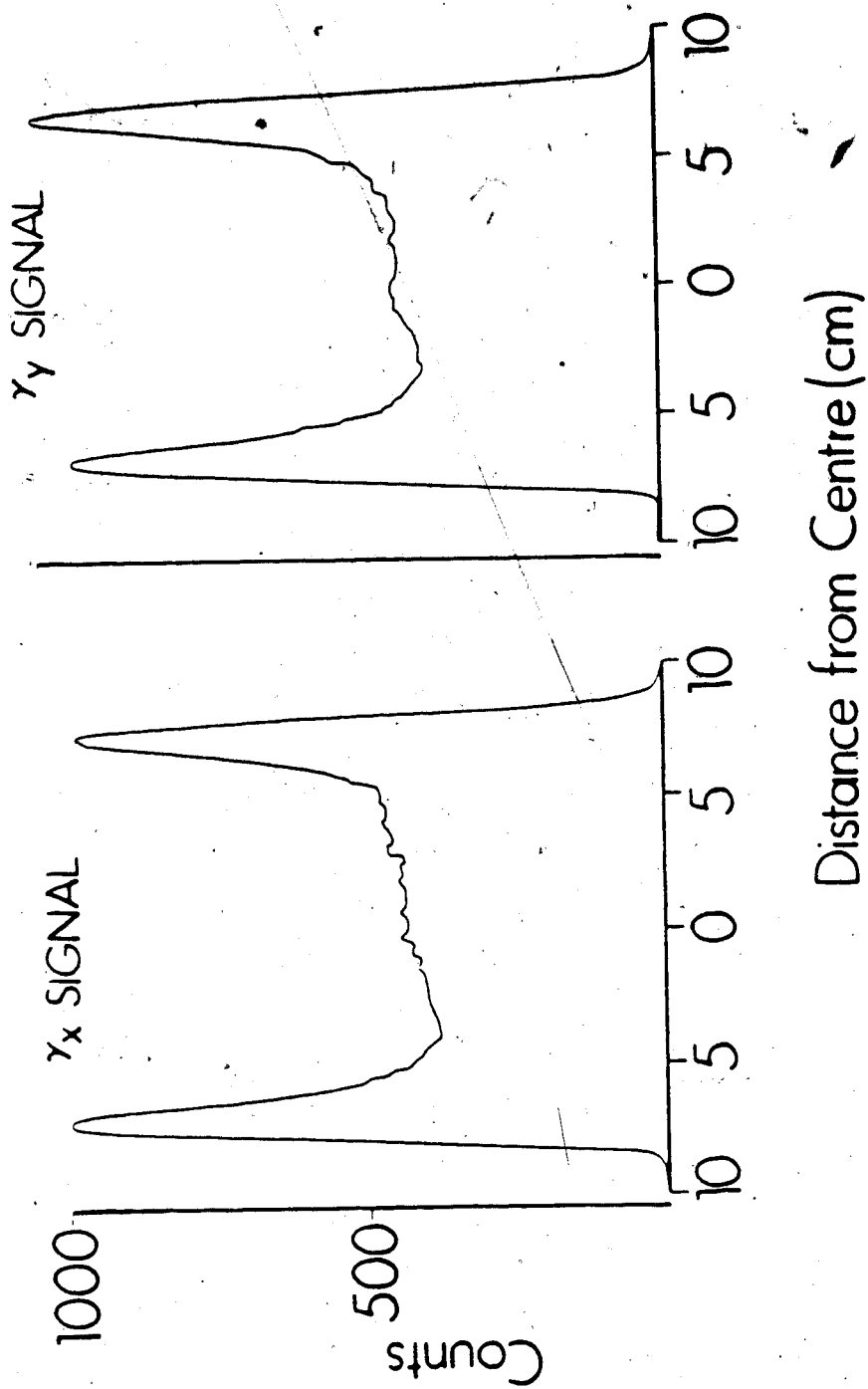


Fig. 5.15 x and y count profiles through the center of the P40/Con Anger camera.

- a) Intrinsic spatial resolution
- b) Energy resolution
- c) Temporal resolution

These three parameters are not independent of one another, and consequently the procedure used to quantify them must account for their interdependence. As an example, in establishing spatial resolution, the count rate should be maintained low enough to avoid dead time losses. It has been shown (Budinger T.F 1977) that loss of counts due to dead time has a relatively larger impact on photopeak than Compton scattered events, thus degrading spatial resolution. Similarly, devices displaying good energy resolution are most likely to have good spatial resolution, since for a fixed energy window width, the better the energy resolution the higher the rejection of scattered radiation.

a) Intrinsic spatial resolution

The intrinsic resolution of the Pho/Con detector scintillator-phototube arrangement was measured by moving a well collimated source to various positions across the crystal face, through its geometrical center. The procedure adopted is consistent with that used to determine crystal spatial linearity. In such a measurement, from a series of calibration curves, it was possible to obtain a conversion of MCA channel number into centimeters. Figure 3.16 shows



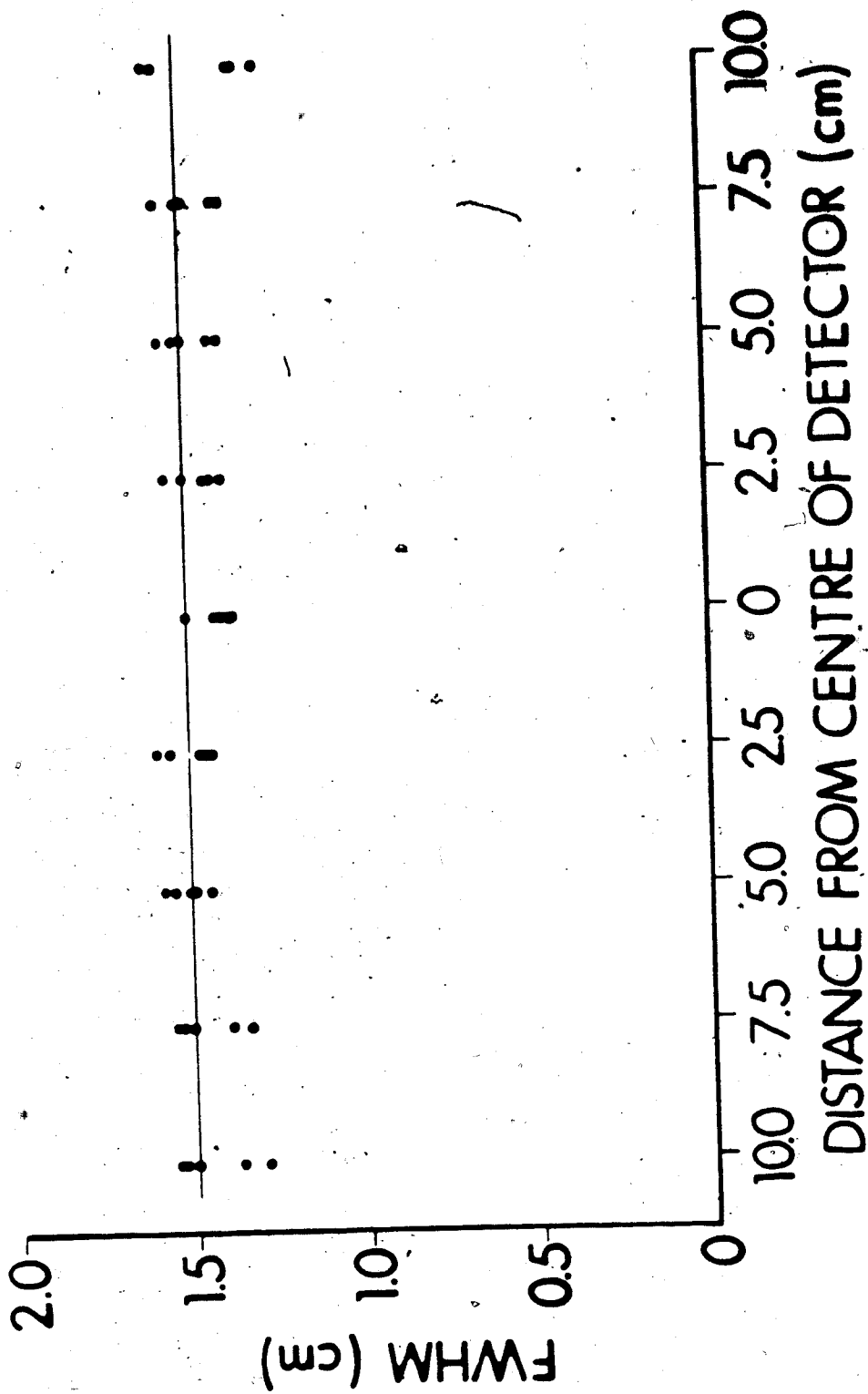


Fig. 5.16 Intrinsic resolution profile for a Pho/Con detector calculated

from the FWHM of the point spread function.

the distribution of the resolution values for the upper detector, with the solid line drawn at 1.5 cm, representing the average resolution value calculated from the set of measurements performed at various positions in the crystal.

b) Energy resolution

For imaging devices, energy discrimination plays an important role in determining the quality of the output image. The edge contours and consequently the resolution of details in the images, are degraded by scattered radiation, which is normally rejected by setting a narrow window centered at the maximum photon energy. For the energy range used in nuclear medicine, narrow window settings are required, since for shallow scattering angles the energy lost by the photons is negligible and they are, thus only minimally displaced down from the photopeak. For example, at 140 KeV a photon scattered through an angle of 60 degrees loses approximately 12% of its energy. The energy resolution is defined as the photopeak full-width-at-half-maximum (FWHM) in KeV divided by the photopeak energy. For the Pho/Con. gamma cameras the resolution was measured at 17% at 140 KeV for Tc-99m and 14% for a 320 Kev source (Cr-51). In general, for scintillation detectors, the better the energy resolution the higher the rejection of scattered radiation within a given energy window. The setting of the energy window to reduce the scattered component, also causes a reduction in the number

of photopeak events contributing to the formation of the image. For systems with good energy resolution one would expect that the ratio between the count within an energy window over the total count in the spectrum should be high even at narrow energy windows. As the window is increased this ratio should rise sharply to a maximum constant value. The ratio between the number of counts in the window and the total counts in the energy spectrum could be used to describe the quality of the detector. This is demonstrated in Figure 3.17 using Tc-99m with a photon energy of 140 Kev and resolution of 17% and Cr-51 with 320 Kev and resolution value of 14%. The curves for the two isotopes should be analysed by their shape since the total scattered component in the Cr-51 spectrum is obviously higher. As shown in Figure 3.17, the ratio for Cr-51 rises to its maximum value more rapidly than for Tc-99m, where the increase is gradual. Figure 3.17 shows also the window to total ratio in the presence of 10 cm of press-board absorber. With the scattering material the rise is less pronounced, particularly for Tc-99m.

#### c) Temporal resolution

Temporal resolution refers to the ability of the system to register pulses within a very short time interval as separate events. In many clinical applications modern imaging devices do not cause appreciable count losses and thus do not affect the statistical significance of a test.

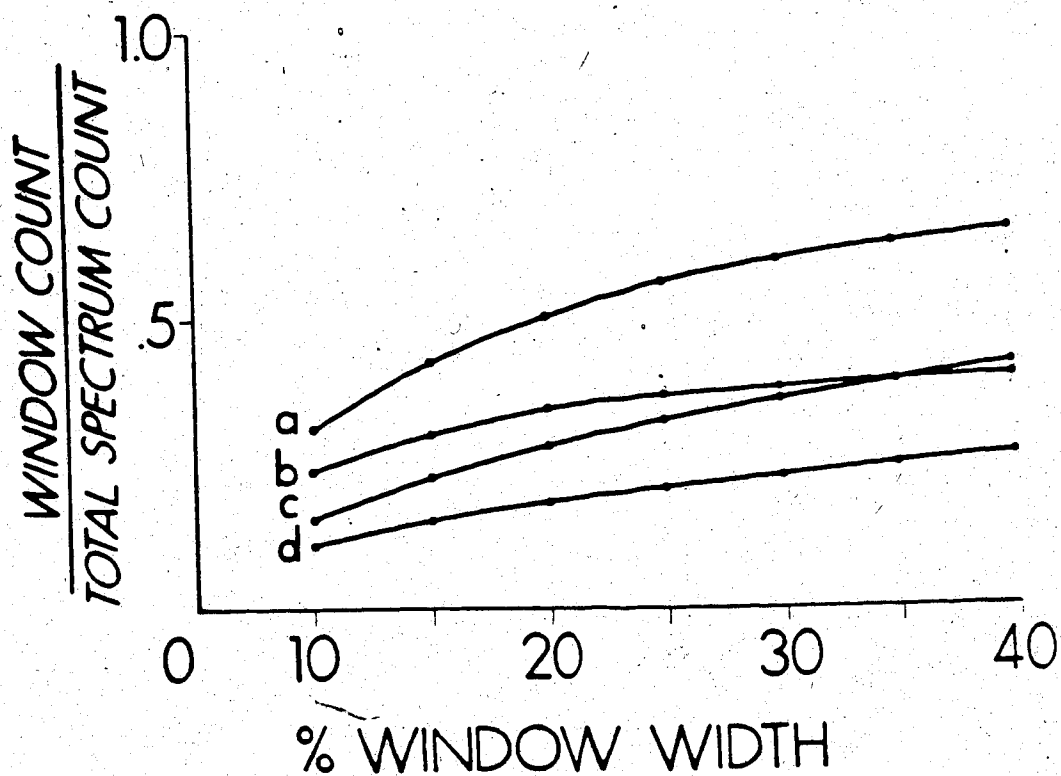


Fig 3.17 Ratio of the number of events detected in a preset energy window to the total number of counts in the energy spectrum. a) Tc-99m (140 Kev) in air, b) Cr-51 (320 Kev) in air. c) and d) are the respective curves in 10 cm of scattering material.

Knowledge of the system temporal resolution becomes essential when fast acquisition rates are needed as, for example, in cardiac imaging. Although imaging techniques might be different even for the same test, the essential requirement is that the amount and location of the activity be reliably determined. The statistical significance of a test is dependent on the number of counts detected, which in turn is related to the activity present in the subject. Limitations of the number of events contributing to the image formation often arises from count losses due to the device dead time. As a consequence, knowledge of the system dead time and the resulting count losses occurring at higher true count-rates helps to establish system limitations. In the case of the Pho/Con, the time limitation is set by the analogue image reconstruction, and image storage in the microdot imager. The time required to process an event and to produce the six point images in the microdot is  $60 \mu\text{sec}$ . This represents the system dead-time, since no other event can be added to the images during this time interval. This limitation can be overcome whenever an on line computer is used to acquire the data for digital reconstruction and display of the image. In this event, knowledge of the gamma camera dead-time becomes important in defining the Pho/Con computer interface time requirements.

The Pho/Con camera dead-time,  $T$ , was measured using the two point source technique and the relation (Adams et al 1973),

$$T = \frac{2(R_1 + R_2 - R_{12} - B_k)}{(R_1 + R_2 - 2B_k)(R_{12} - B_k)}$$

where  $R_1$  and  $R_2$  are the count rates of the two point sources,  $R_{12}$  is the count rate measured simultaneously with the two sources and  $B_k$  is the background count. The above relation is valid provided that count rate differences between the two sources is less than  $\pm 10\%$ . To include possible effects due to the analyzer window setting, the signal fed into the scaler was the unblank signal, which is formed following the detection of a photon of the appropriate energy. The dead-time with collimator removed was measured with analyzer window widths of 15% and 25%. The dead-time calculated using the above expression gave a value of 5.7  $\mu\text{sec}$  for the 15% window and a slightly lower value of 5.3  $\mu\text{sec}$  for the 25% window. These values are in essential agreement with those obtained using the formula for a paralyzable system as suggested by NEMA standards (NEMA measurement standard).

To give an indication of the count losses at higher count rates a Tc-99m point source with a half life of 6.05 hours was counted with the Pho/Con upper detector with collimator removed and again using the unblank signal. To determine the true count we assumed that at very low count rates the measured rate could be fitted to an exponentially decaying curve. This is a valid assumption provided that the count-rate is low enough to exclude possible losses due to the system dead-time. By projecting

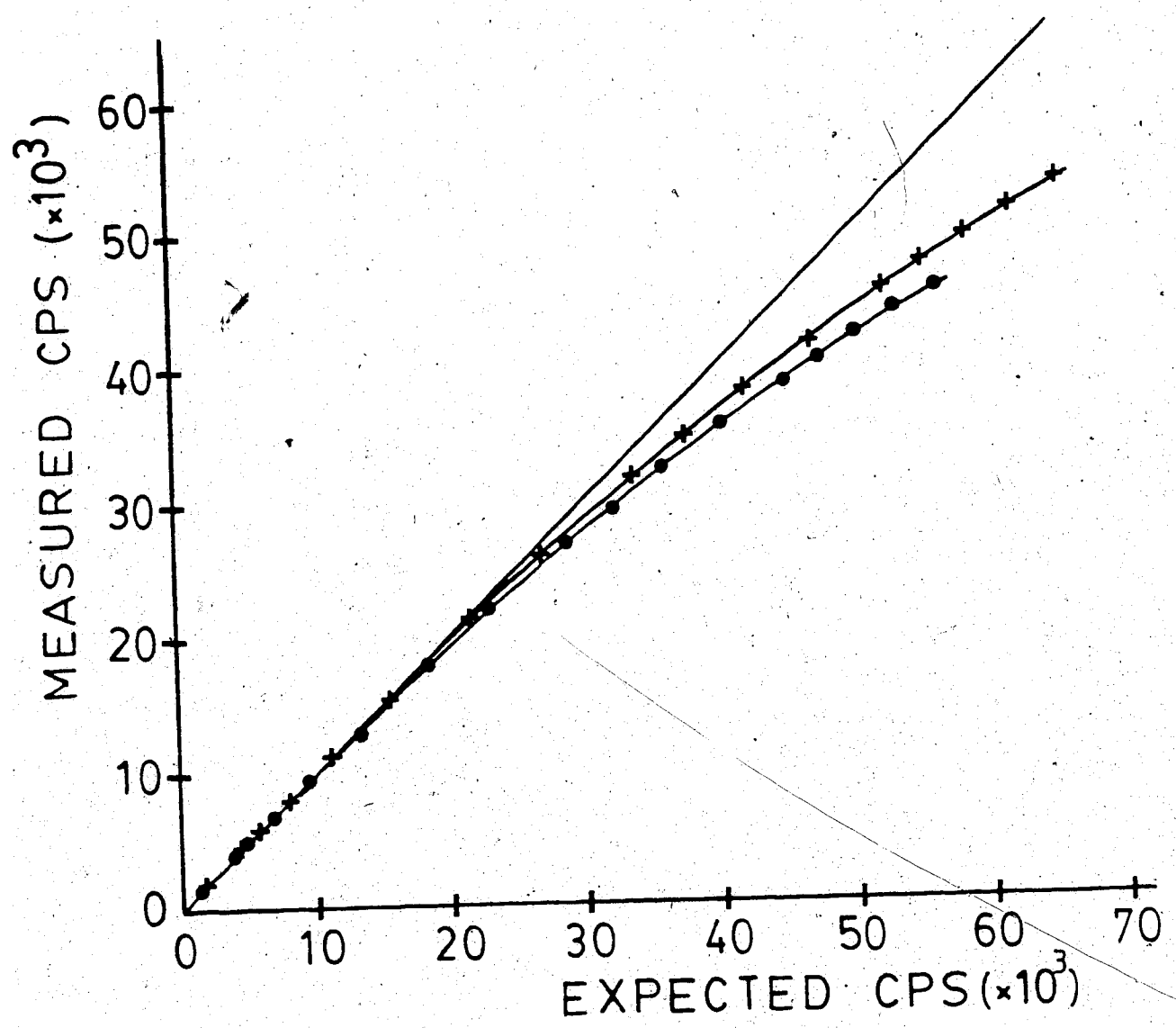


Fig. 3.18 Pho/Con count losses measured with the 15 (●) and 25 (+) of the analyzer window. The straight line represents zero count losses.

the curve at time  $t = 0$  one can determine the count-rate at the beginning of the measurement. Figure 3.18 shows a plot of measured versus true count obtained using the procedure just described. The input count-rate to give a 20% loss was calculated using the expression

$$R-20\% = 1/T \times \ln(10/8)$$

where T represents the dead-time of the system. From the expression, for a 15% window a 20% loss is encountered at a count-rate of 40.5 K cps. The same loss for a 25% window occurs at a count rate of 43.7 K cps. At the same rate the count loss measured using Figure 3.18 yielded values which are 8% and 9% lower respectively.

In any event, the camera dead-time will not cause count losses in most clinical applications, where the measured count rates are typically 10K count/sec for liver scans for an injected activity of 150 MBq. Lower count rates are normally observed for other clinical investigations appropriate for this device.

### 3.3 System performance

The ability of the Pho/Con to produce clinically useful images depends on the optimal performance of the reconstruction algorithm together with the proper selection of a number of input parameters. At the beginning of a



study the operator can select a number of Pho/Con settings to yield the best possible image for the particular clinical investigation. Examples of input parameters are speed and index width of the scan, maximum scan area, and separation of focussed planes (tomo-separation). The combination of the latter two defines the position and separation between the tomoplanes while the scan width and speed determine the imaging time required for the specified maximum scan area. In addition to selectable input variables, the system performance is determined by the intrinsic properties of the detector collimator and gamma camera, as discussed above. It is also possible that the spatial distortion measured for the camera head could degrade further the quality of the image. These concerns suggest that total system linearity and resolution should be investigated. The measurement of these parameters acquires a special significance in view of the possible conversion of the device to yield analogue and digital images. For this reason it was deemed necessary to investigate the system linearity and resolution both in the analogue and digital mode. The characterization of the system performance in terms of linearity and resolution serve also as the basis of comparison between the Pho/Con operating characteristics measured at the output of the microdot imager with what can be achieved using digital manipulation of the detector signals. Finally, such an investigation should allow comparison between analogue and digital reconstruction techniques, thus identifying potential limitations of the system in the two imaging

modalities.

### 3.3.1 System uniformity

The dynamic measurement of the system uniformity was performed by scanning a Co-57 flood source. The crystal non-uniformity appears to have no major effect on the ability of the system to reproduce a uniform distribution of activity, as shown in Figure 3.19. This image represents the third readout plane image obtained with the system microdot imager and with the source placed at the collimator focal depth.

### 3.3.2 System linearity

Spatial linearity is the ability of an imaging device to accurately reproduce the geometrical dimensions of a line, or an array of linear sources of activity (Hine et al 1978). Normally, images obtained with rectilinear scanners are relatively immune from spatial distortion which occurs more frequently with scintillation gamma cameras. For the Pho/Con, the relationship between the linearity of the system and that of the gamma camera was studied by scanning an orthogonal array of point sources. The assessment of the system linearity was then made by examining and measuring the spacing of the image point pattern from the film obtained with the microdot imager. The orthogonal array of

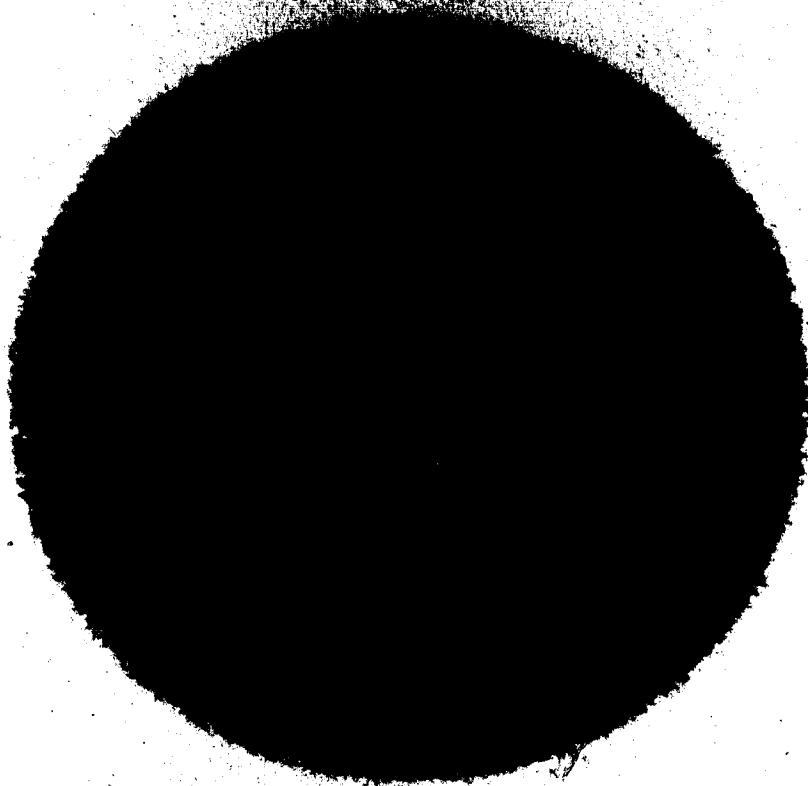


Fig. 3.19 System uniformity obtained by scanning a Co-57 flood source. Image of the flood obtained with the microdot imager.

point sources was produced by covering a flood source filled with 1850 MBq of Tc-99m with a lead mask, 6.4 mm thick, containing a regular array of holes 3 mm in diameter. The spacing between adjacent holes was set at 2 cm which exceeds the system resolution in the coronal plane. The actual measurement was performed by placing the test pattern at the collimator geometrical focal distance and subsequently at the position of the first and sixth tomoplanes for the appropriate Pho/Con settings. In the latter two cases the contribution of the camera signal is maximized according to the ratio  $D/H$ . Again,  $D$  is the distance of the activity from the geometrical focal depth and  $H$  represents the total distance of collimator thickness  $L$  and focal distance  $F$ . The system linearity was determined by measuring the separation regularity of the test pattern from the microdot images shown in Figure 3.20. The spatial separation between dots in the pattern is constant throughout the two images. The slight magnification difference between the two images is a characteristic of the microdot imager.

In parallel to the analogue reproduction of the test pattern the camera position signals were collected into a DEC 11/70, thus allowing reconstruction of the same data pattern using a simple back projection algorithm. By using the expression for the coordinates of the detected events, it was possible to produce coronal images of the test pattern in all respects equivalent to their analogue counterparts. The advantage of digital reconstruction lies

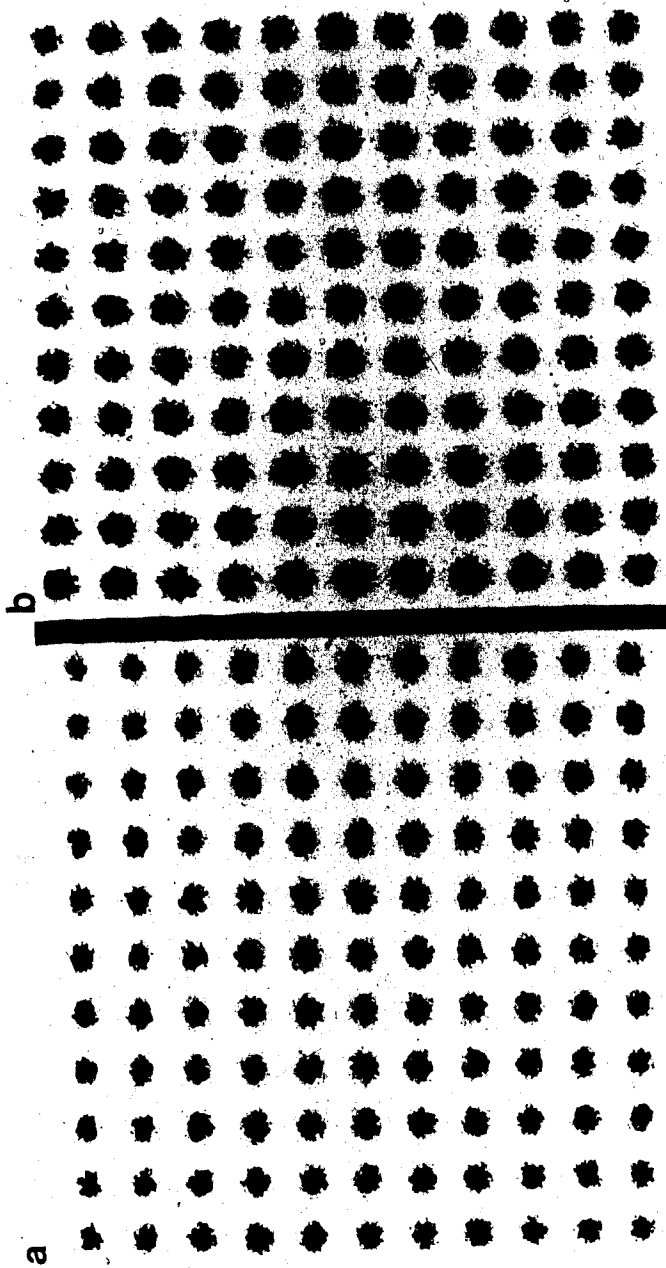


Fig. 3.20 Analogue images of the orthogonal test pattern obtained by scanning the source with a 25 cm x 25 cm maximum scan area. (a) image of the pattern in the first focal plane and (b) with the pattern in the third focal plane.

in the quantitative nature of the output. The linearity and uniformity of the test pattern image was obtained by identifying the center of the count density profiles of the array of points in the image. Figure 3.21 shows a two dimensional map of the measured peak position in the orthogonal test pattern included by the open circle. The test pattern is represented by the fine grid which is superimposed on the reconstructed array of point sources to better identify possible regions of non linearity. The system linearity is clearly demonstrated by the digital reconstruction of the orthogonal test pattern where the deviation of the measured pattern is within the displacement error of the size of one pixel.

### 3.3.3. System resolution

For position sensitive detectors, resolution refers to the ability of the system to spatially separate and image two point sources or two line sources. The smaller the distinguishable separation between the two sources of activity the better the resolution. Quantitatively, resolution can be expressed in terms of the full width at half maximum (FWHM) of the point spread function (PSF), or of the line spread function (LSF). Since each Pho/Con detector reproduces the activity distribution of six planes situated at different distances from the collimator, the system resolution must contain a depth dependence component.

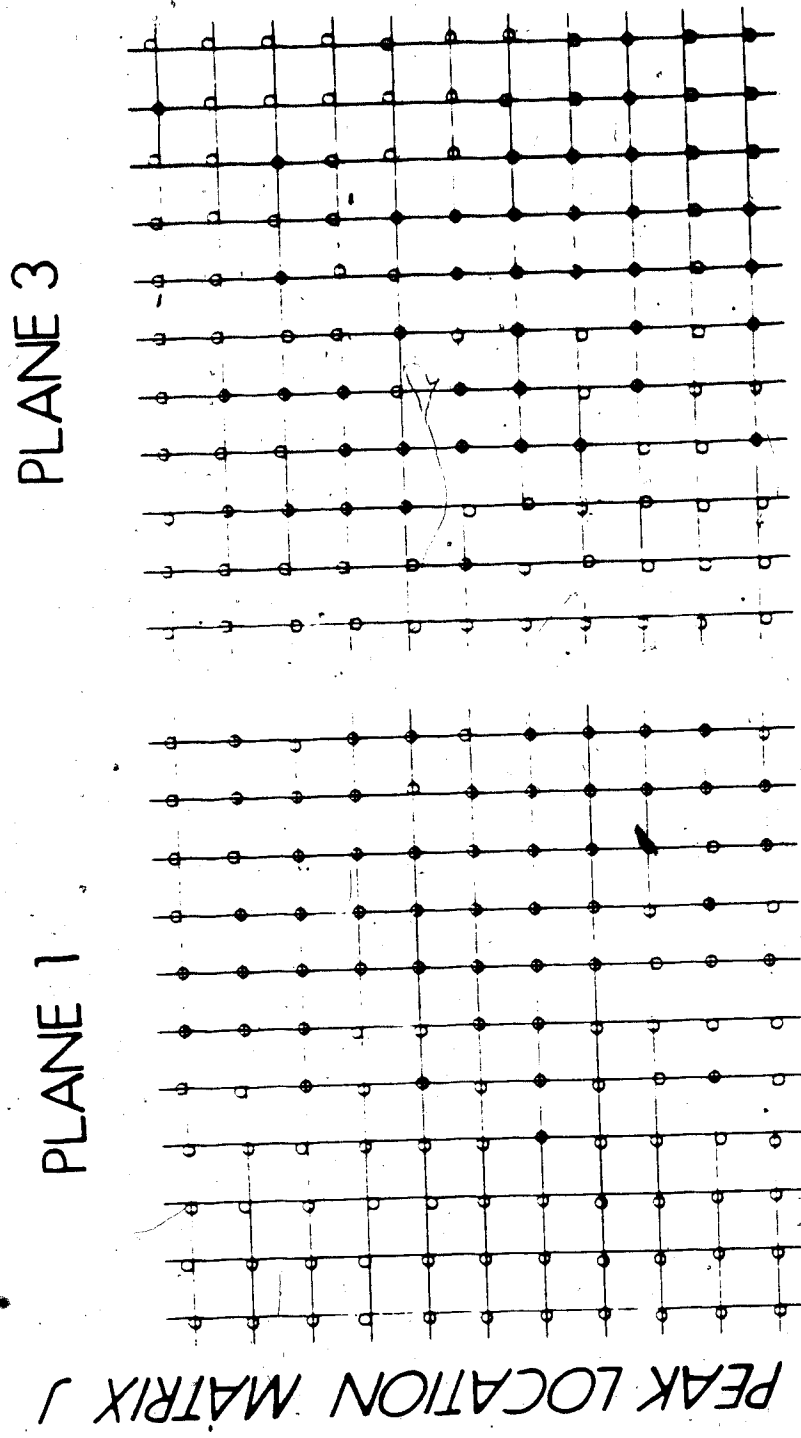


Fig. 3.24 Computer reconstructed orthogonal test pattern for the first and third readout planes. Circles indicate system reconstructed locations of points.

As shown in the discussion of the collimator characteristics, the resolution  $R_o$  is given by the sum in quadrature of the collimator components  $r_c$  and  $r_p$ , and the contribution to  $R_o$  due to the gamma camera  $r_g$ . Of the three resolution parameters, the dominant term is the parallax component given by:

$$r = \sqrt{2} |D-b| \tan \frac{\alpha}{2}$$

This term is non-zero for activity above and below the read-out plane situated at D. At the six focal-planes where  $D = b$  the system resolving distance reduces to the simple expression:

$$R_o^2 = r_c^2 + r_g^2$$

Experimentally, the system resolution was measured by imaging a line source of activity placed at 45 degrees with respect to the detector axis. Typical images of the line produced by the microdot imager are shown in Figure 3.22, together with the optical density profiles from the film. For each setting of the Pho/Con input parameters, the imager produces six images, each representing the reconstructed portion of the line at the various focal depths, with the blurring pattern from planes above and below superimposed. By suitable selection of scan input parameters, images of the line at increasing distances from the collimator allow the establishment of the dependence of resolution as a function of the source and collimator separation.



Normalized density profiles of the images of the line source through the sharpest region in the images, were obtained with a scanning densitometer (Scanditronix RFA 3). Preliminary measurements ensured that the images of the line count densities were within the linear region of the film characteristic curve. From the density plots shown in Figure 3.22, the system resolution was obtained as a measure of the full width at half maximum (FWHM). Figure 3.23 shows the calculated and measured resolution values of the three collimators presently available with our system. In the plot, the heavy solid lines are the calculated values for the three collimators.

The system resolution was measured using digital reconstruction of a point source by means of simple back-projection algorithm. The source was positioned at increasing distances from the collimator face. Each image was obtained by scanning the point source with a scan area of 25cm x 25cm and a scan index width of 0.3 cm. The scan speed was set to maintain count rates well within the analyser dead time. Coronal images of the point source were reconstructed using the coordinate equation shown earlier. In the reconstruction algorithm the volume element had dimensions of 0.2 cm x 0.2 cm x 0.2cm, which is somewhat smaller than the system resolution. The resolution values were determined by plotting the count density profiles of slices taken in the X, Y, and Z planes through the voxel with the highest count.

Figure 3.24 shows typical profiles of the three

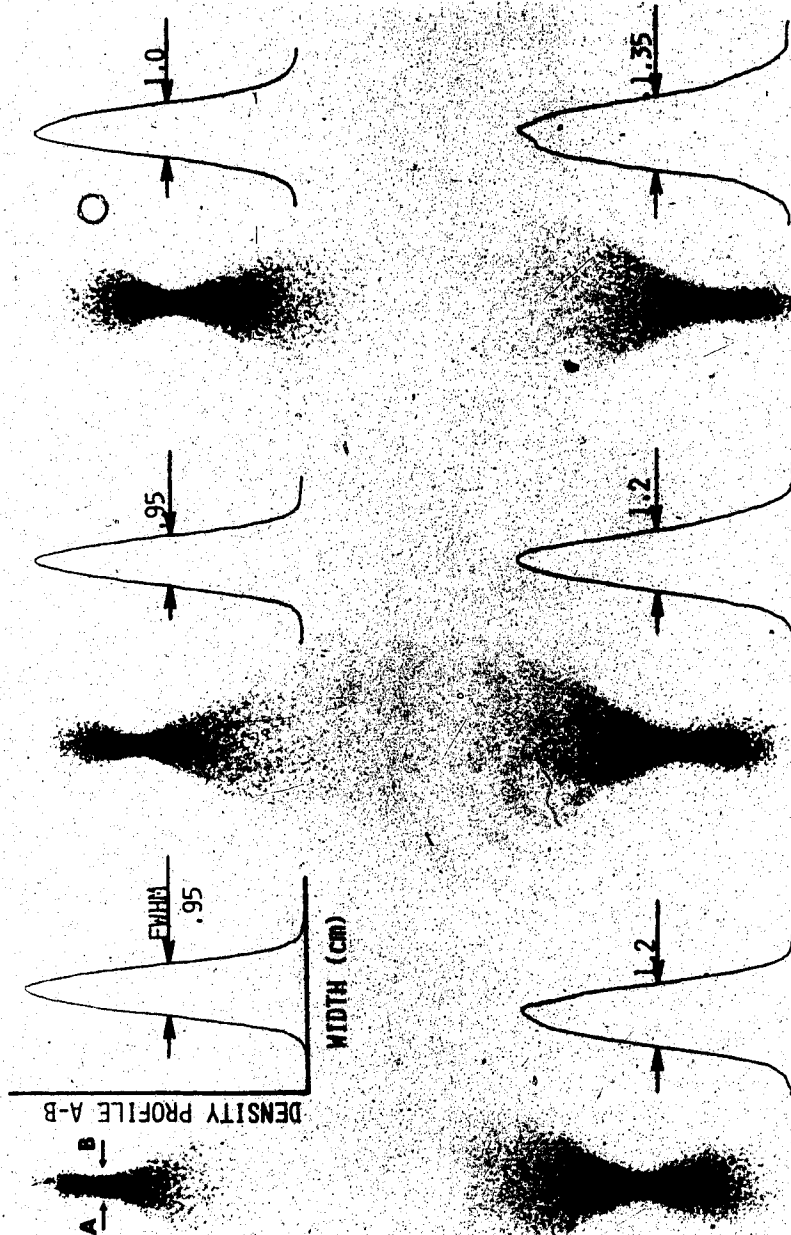


Fig. 3.22 Analogue images of the line source at 45 degrees relative to the detector axis together with the corresponding density profiles of the six readout planes.

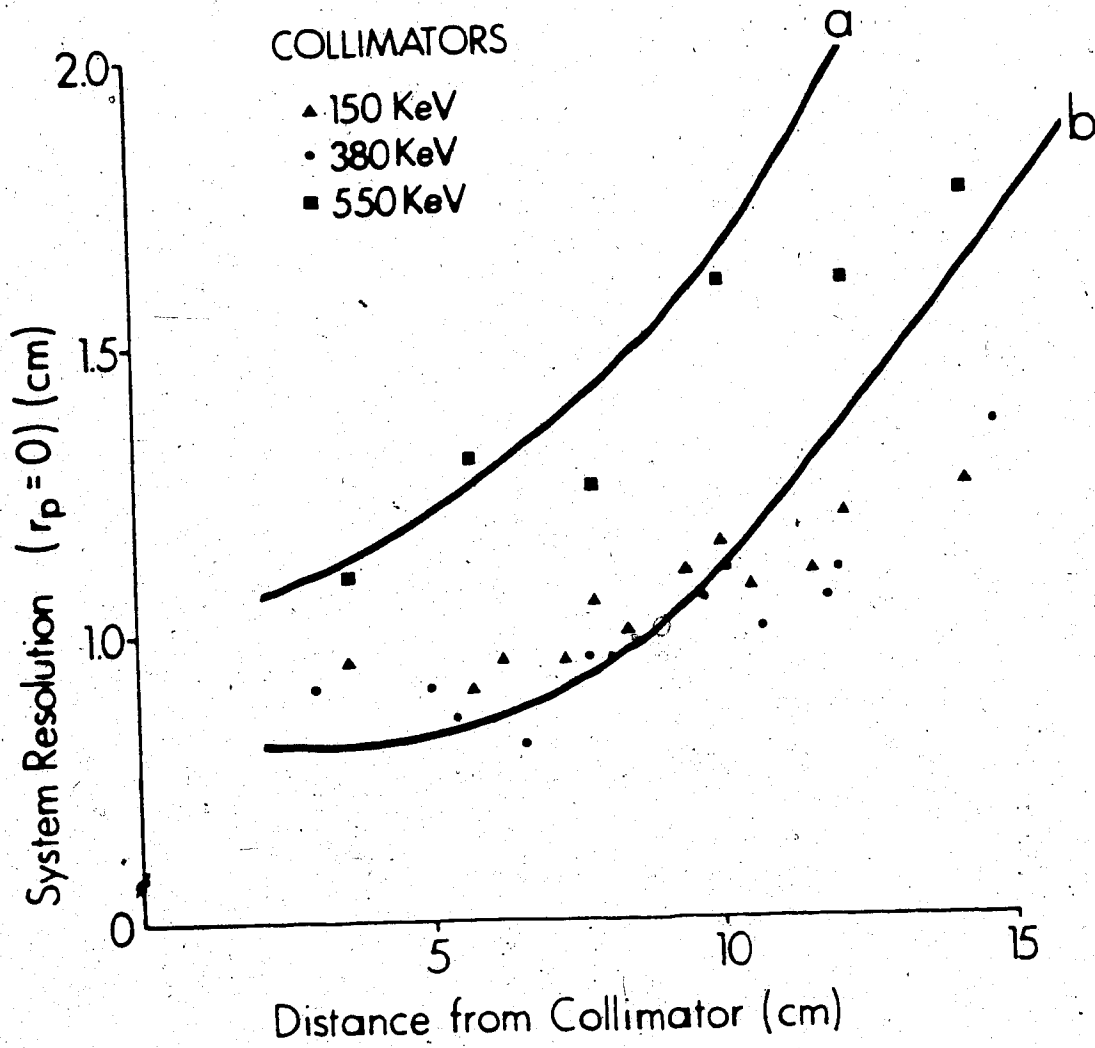


Fig. 5.23 Pho/Con resolution as a function of source distance from collimator for low, medium and high energy collimators. The solid lines are the calculated values for (a) the 550 KeV and (b) the 150 KeV and 380 KeV.

coordinates X, Y, Z where the solid curve represents the least square fit to the non-linear data using a Gaussian function. In the fitting, the minimization of the Chi square was done using the grid search method (Bevington P. R. 1969). Figure 3.25 shows a plot of the resolution along the Z axis obtained with the low energy collimator. The depth resolution together with the coronal resolution allows the definition of the voxel size as a function of distance from the collimator face. In digital deblurring one must contend with a resolution volume of 1 cm x 1 cm x 3.5cm with the Z component degrading rapidly with depth.

Figure 3.26 displays measured FWHM of the point spread function in X and Y, calculated from the fitted curve, as a function of distance from the collimator face. In Figure 3.26 data from the microdot images and calculated system resolution values were also included, to allow a closer comparison between the two imaging modalities. The resolution measured using analogue and digital methods give very similar results at small distances from the collimator. The slight change in the resolution values are probably associated with the uncertainty in the film density plots.

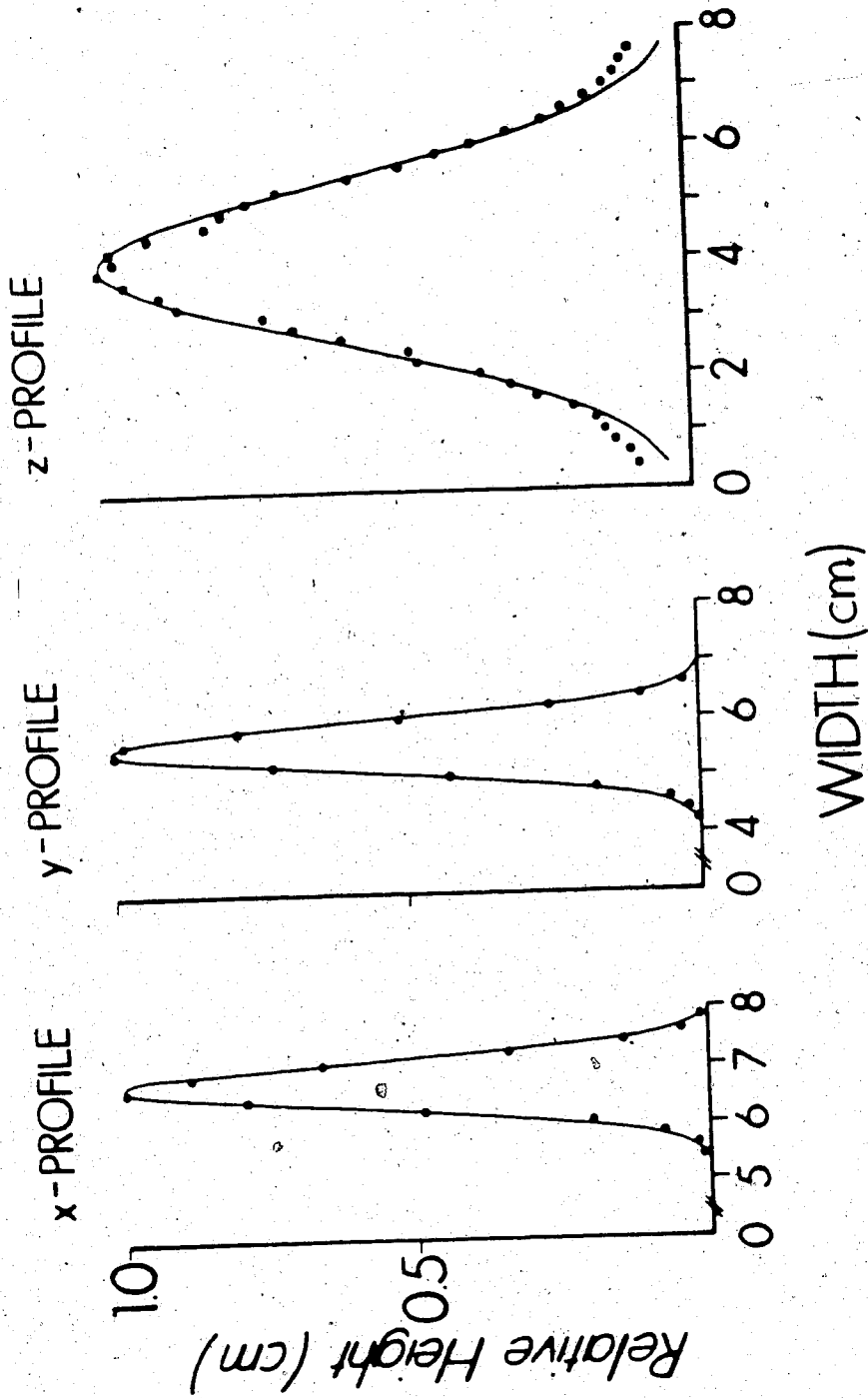


Fig. 3.24 Normalized x, y, and z profiles of a  $^{57}\text{Co}$  point source obtained with a simple back projection reconstruction algorithm.

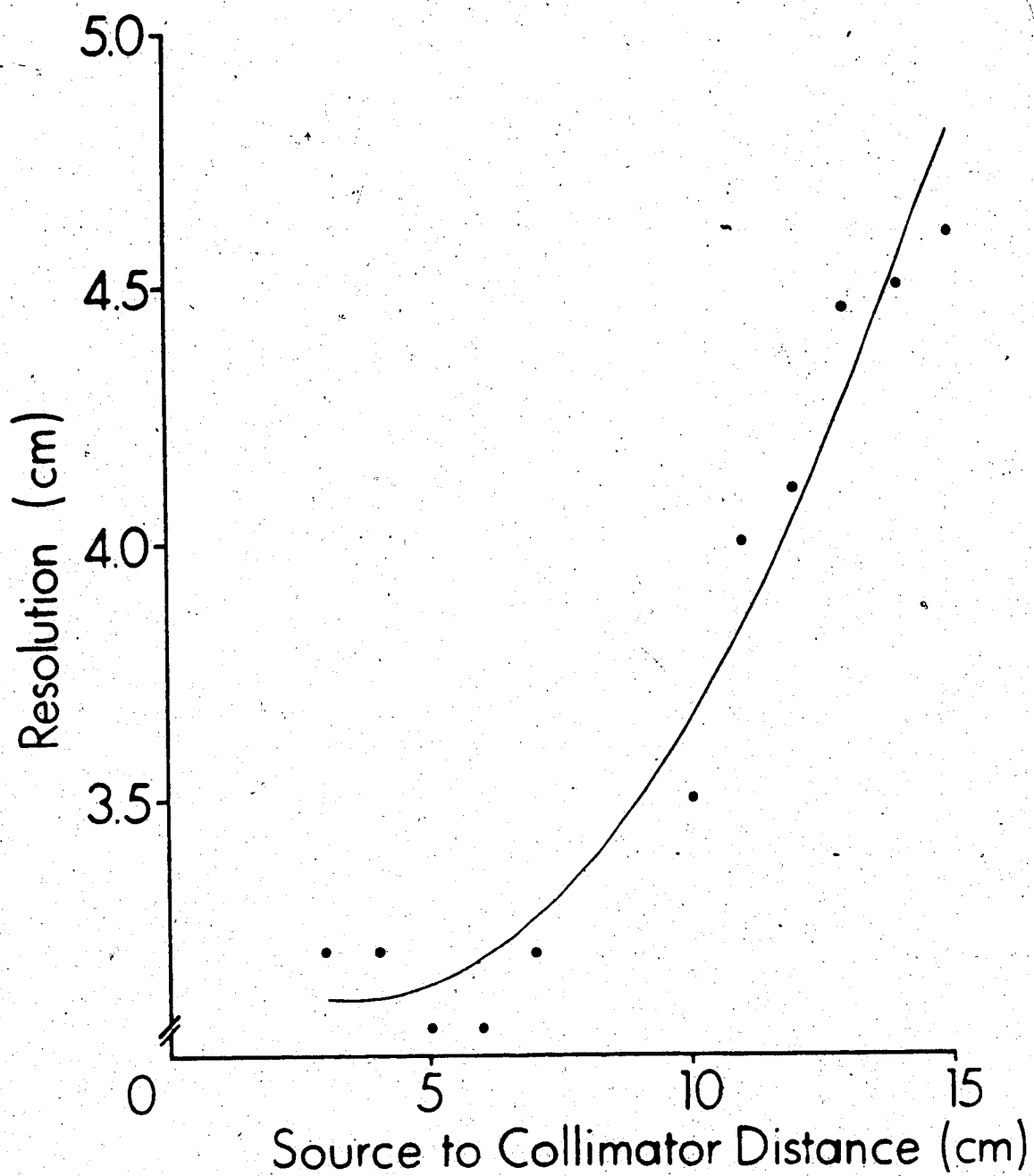


Fig. 3.25 Representation of the resolution along the  $Z$  axis.

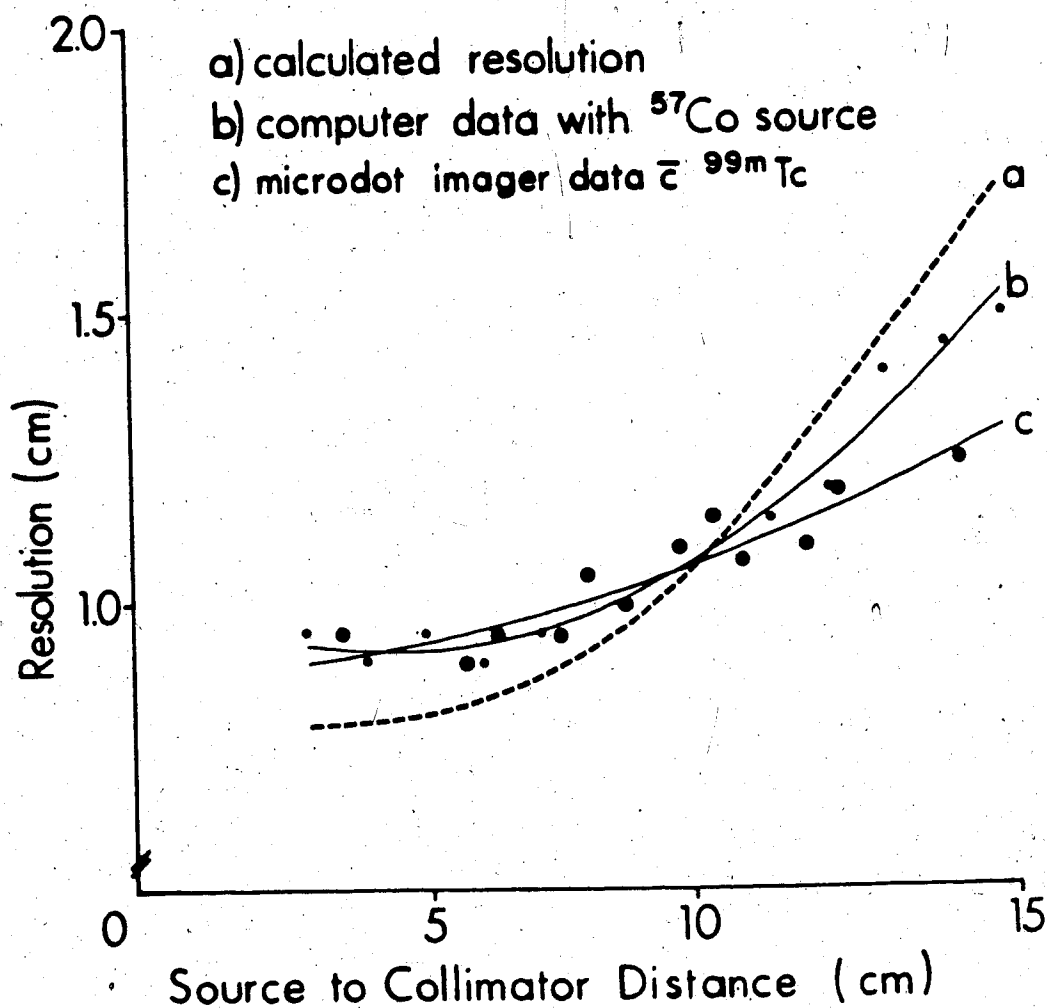


Fig. 3.26 System resolution measured with the 150 KeV collimator. (a) calculated resolution with  $r_p = 0$ , (b) computer data obtained imaging a Co-57 point source, (c) resolution measured using density profiles of analogue images of the line at  $45^\circ$ .

## CHAPTER 4

### 4.1 Focal plane tomography and the limited-sampling-angle technique.

The objective of a tomographic imaging system is to produce images of structures deep seated within the human body. This can be achieved by removing overlying and underlying structures from the wanted image plane by blurring the unwanted information. This type of imaging technique was first introduced in radiography by Bocage in the early twenties (1921). Although of limited sophistication compared to transmission CT, this technique was able to remove off-plane structures by moving the x-ray tube and film cassette in opposite directions at a predefined speed. This allowed one to select an image plane in which the structure would appear stationary, while overlying and underlying structures would be mispositioned and thus blurred.

In nuclear medicine the same principle was exploited by Anger (1968) to produce the first commercial longitudinal tomographic device. With such a system images were reconstructed by detecting the radiation emitted by an object source. In the Anger system the image of the radioisotope distribution is obtained using a position sensitive detector operated as a scanning device. Other



early focal plane tomographic techniques were 7-pinhole tomography (Vogel et al 1978) and coded aperture tomography based on the concept of imaging using Fresnel zone plates, the latter was first investigated in planar imaging by Barrett (1972) and Rogers et al (1972). The slant hole technique was introduced to overcome some of the problems encountered with the Anger tomographic scanner and the 7-pinhole system; that is to achieve a different compromise between sensitivity and resolution (Muehllehner G. 1971) and eliminate image distortion (Lin et al 1981).

The image reconstruction in focal plane tomography is most easily achieved by simple back projection. The disadvantage of this type of reconstruction is that each detected event is placed in the image including events whose origins lie outside the plane of focus. This unwanted off-plane information blurs the image according to the system blur function, which depends on the distance between the origin of the background activity and the plane being reconstructed. For the Pho/Con which employs multi-hole focussed collimators, the blur function has a bi-conical shape as shown in Figure 4.1. This represents the three dimensional point spread function reflected at its vertex. The added disadvantage of blurred tomography is the lack of quantitative information giving the true activity distribution in the object. From a qualitative point of view focal plane tomography has been shown to produce images of good diagnostic quality (Anger H.O. 1969, Winchell et al 1970, Volpe et al 1971, Turner et al 1976, Vogel et al

1978).

To improve the clinical usefulness of images obtained with this tomographic technique, methods have been developed to de-convolve these blurred patterns. The most common approach to the deblurring of images obtained with focal plane tomography has been to use mathematical methods (Chu et al 1977, Townsend et al 1978, Hooper et al 1979). The stimulus for the development of techniques capable of removing the out-of-focus contribution has originated from positron imaging performed with stationary multiwire proportional chambers (MWPC) (Chu et al 1977, Tam et al 1978, Townsend et al 1978, Tam et al 1979, Townsend et al 1980). The similarity between single- and dual-photon focal plane tomography is that both employ systems which have limited fields of view. In the single photon devices the field of view is defined by the collimators. For the dual photon technique employing either gamma cameras (Muehlechner 1975) or multiwire chambers (Lim et al 1975, Hattner et al 1976) both coincident events must be detected. This determines the path along which the positron electron annihilation has taken place and limits the camera field-of-view of the detector system. This complicates further the reconstruction problem since the reconstructed section becomes sensitive to the object's configuration, the geometrical characteristics of the particular viewing system, and the number of counts in the image (Budinger T.F. 1980). Of the focal plane tomographic systems the Pho/Con is unique, since this device performs an analogue single



Fig. 4.1 Characteristic blur pattern produced by the Pho/Con and obtained by imaging a line source at  $45^\circ$  with respect to the collimator central axis.

back projection reconstruction with the final image display on x-ray film. It was soon realized by many workers (Garcia et al 1980, Pickens et al 1980, 1981, Garcia et al 1981) that the instrument could be considerably augmented by being interfaced to a digital computer. The processing of the raw image data by means of a computer increases the clinical utility of the Pho/Con images by removing the off-plane activity. Digital manipulation of the data has the advantage that it allows one to display the usual coronal images and additional sagittal and axial planes. The digital handling of the raw data also allows a certain degree of image processing, such as background subtraction, smoothing and more sophisticated filtering. Finally digital techniques are suitable to multi-isotope imaging for the improvement of depth information by correcting for distortion due to attenuation.

#### 4.1.1 Pho/Con interface to a Dec 11/70 computer

The system to interface the Pho/Con multiplane scanner to a PDP-11 computer was designed by the BEC Company (Bay Engineering Company 1979). The Pho/Con analogue and digital signals are presented to the computer upon a request command which is produced either by the interface or by the computer itself.

Upon request of data, the Pho/Con provides the computer interface with the gamma camera coordinate signals, the

energy strobe Z, and ~~the~~ scanner position signals. The interface assembles these signals into data words and scan position words and presents them to the computer in a form which can be analyzed by software. The x and y analogue signals from the Pho/Con gamma camera are digitized to 12 bit on command by the Z strobe which follows the detection of an event with the appropriate energy. The most significant seven bit from x and y-signals are then combined to the upper or lower detector and isotope analyzer bit to give a 16 bit data word. Bit 00/06 represents the x-signal, 07/13 the y-signal, 14 and 15 are the analyzer and detector identifier bits. The beginning of a scan is controlled by the camera which initiates a list mode transfer of the data to the computer where two blocks of memory are assigned as temporary buffers. The data and scan words are written into a first buffer until full at which time the software provides the address for the second buffer. The data from the first buffer is transferred into disk via Direct Memory Access (DMA) transfer. The DMA transfer allows movement of variable length blocks of data to or from a specified location in the memory using the PDP-11 unibus (Digital Handbook). The detector position is monitored continuously in such a way that when the position has changed, a three word block is written into memory. The first word in the block is a flag word which identifies the start of a new scan block with new collimator coordinates. The remaining two words are the new detector position coordinates.

#### 4.2 Single back projection: Pho/Con reconstruction algorithm

The twelve images are reconstructed by means of analogue circuitry which combines the position of the detector  $(x_c, y_c)$  with the position of the scintillation in the gamma camera  $(x_g, y_g)$  relative to the origin of the scan. A detailed description of the system operation can be found in the original article by Anger (1968), and in the system operating manual (Searle 1976). As shown in Figure 4.2, the line of flight of each event, in a three dimensional configuration, is defined by the line joining the collimator geometrical focal point  $(x_c, y_c, z=H)$  and the scintillation point in the crystal  $(x_g = x_c + x_i, y_g = y_c + y_i, z=0)$ .  $x_i$  and  $y_i$  are the scintillation coordinates with respect to the centre of the crystal. Coronal images at a depth  $D$  are represented by those points with coordinates  $(x, y, z=H+D)$  satisfying the following linear equations:

$$\frac{x - x_g}{x_c - x_g} = \frac{y - y_g}{y_c - y_g} = \frac{z}{z_c}$$

Substituting for  $z=H+D$  and  $z_c=H$  the above relations reduce to the event coordinate equations:

$$x = x_c - x_i \left( \frac{D}{H} \right)$$

$$y = y_c - y_i \left( \frac{D}{H} \right)$$

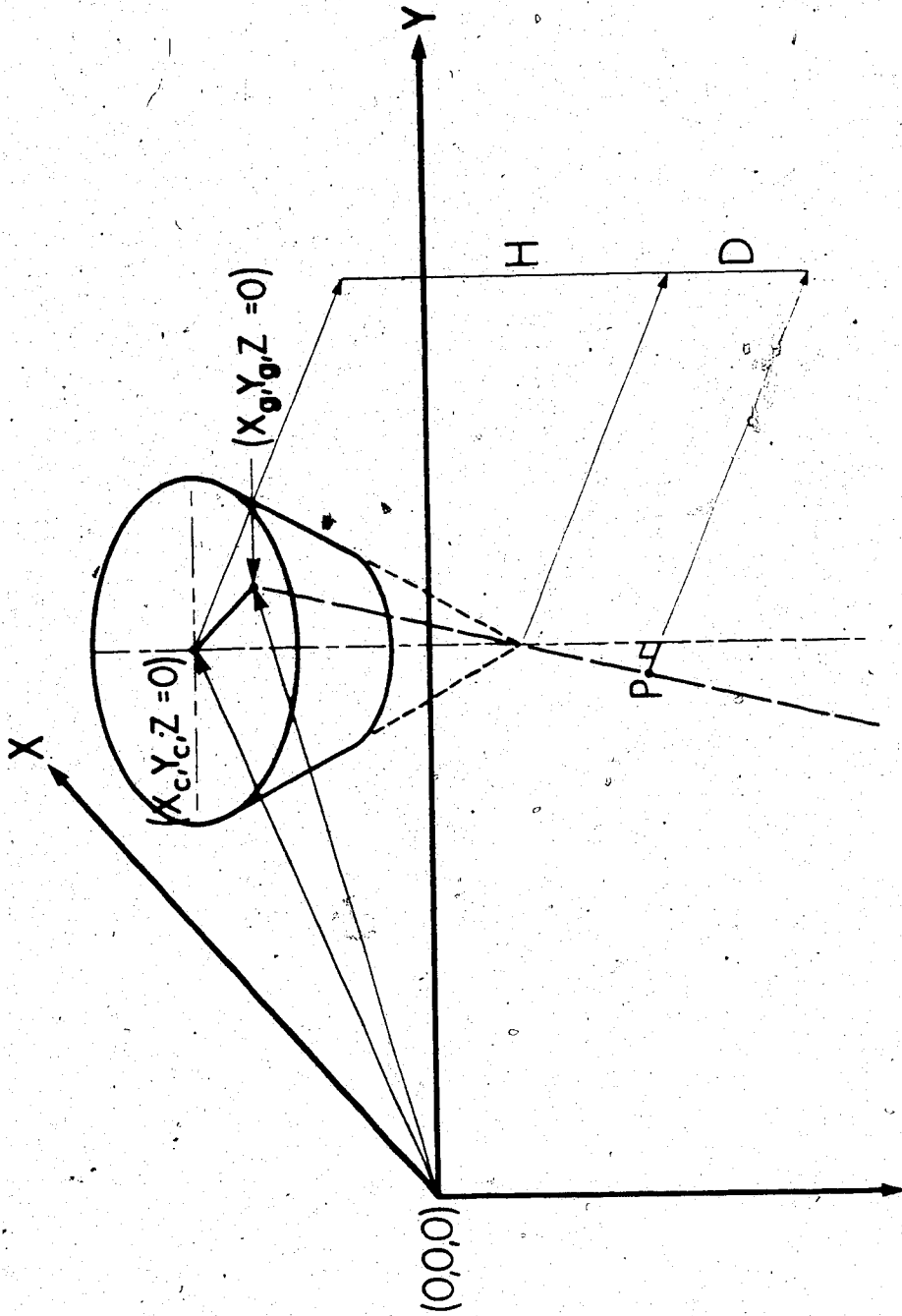


Fig. 4.2 Spatial localization of an event originating at P. Pho/Con detector coordinates  $(x_c, y_c, z_c = 0)$  and the point of interaction in the crystal  $(x, y, z = 0)$  are measured relative to the origin of the scan  $(0, 0, 0)$ . D is the vertical distance of P from the focal plane, and H represents the sum of the collimator thickness and focal depth.

Similarly, saggital and axial images can be obtained by replacing, in the linear equation,  $y=S$  and  $x=A$  where  $S$  and  $A$  are constants. This will result in the following equations:

$$x = \frac{x_i}{y_i} (S - y_c) + x_c$$

$$z = - \frac{H + F}{y_i} (S - y_c) + (H + F)$$

for the saggital images, and

$$y = \frac{y_i}{x_i} (A - x_c) + y_c$$

$$z = - \frac{H + F}{x_i} (A - x_c) + (H + F)$$

for the axial images. These expressions describe the location of events in the coronal, saggital and axial planes. In the specific case of coronal images, which are equivalent to the analog output of the Pho/Con, the tomographic properties result from the addition to the detector signal of the fraction  $D/H$  of the crystal signal, thus creating the necessary blurring condition. Thus the activity at a given focal plane  $D$  will be in focus while activity above and below the plane of interest will be blurred. The amount of blurring will depend on the absolute depth separation between the focal plane at  $D$  and the out of plane activity at same depth  $D$ , with the degree of blurring proportional to  $|D-D|/H$ .

In recent years, some attempts have been made to use



the Pho/Con in single photon emission computed tomography (SPECT) (Garcia et al 1980, 1981, Pickens et al 1980, 1981). The improved flexibility of digital imaging combined with a whole body SPECT capability have encouraged the digital development of the Pho/Con. The digital reconstruction of images using the Pho/Con is subject to a limited sampling angle due to the constrained motion of the device and the physical dimensions of the gamma camera and focussed collimator. This limitation introduces a blurring artefact into the digitally reconstructed images. Despite this problem, new deblurring techniques have been developed (Chu et al 1977, Tam et al 1978, Townsend et al 1978, Tam et al 1979, Hooper et al 1979, Townsend et al 1980, Tam et al 1980, Garcia et al 1981) which make possible the reconstruction of images with improved signal-to-noise ratios.

The deblurring methods proposed here require an a-priori determination of the system response to a point source of activity. Knowledge of the point source response function allows for the correct definition of the system response to any type of input function.

#### 4.2.1 3-Dimensional reconstruction for limited-angle sampling

In focal plane tomography, the image of the activity distribution obtained with a simple back projection

reconstruction algorithm, represents a 3-dimensional reconstruction problem. This can be expressed as the convolution of true activity distribution described by the density function  $f(x,y,z)$  with the response function of the system detector defined by  $b(x,y,z)$ . In mathematical terms, the image  $g(x,y,z)$  can be expressed in the following way,

$$g(x,y,z) = f(x,y,z) * b(x,y,z)$$

where the symbol  $*$  represents a 3-D convolution operation. For the case of single photon imaging with the Pho/Con, as with positron imaging employing two large stationary position sensitive detectors (i.e. gamma camera, MWPC) the above expression can be simplified to a two dimensional convolution problem. This is done by observing that the distribution in each image plane results from the summation of the activity present in the plane of interest together with the blurred value resulting from the activity present in the remaining planes. In mathematical terms:

$$g_i(x,y) = \sum_j^n [f_j(x,y) * b_{|j-i|}(x,y)]$$

Where  $f_j$  and  $b_{|j-i|}$  are the two dimensional expressions representing the activity distribution and the blurred function. The chosen notation is convenient in the implementation of the deblurring algorithm described later. In formulating the convolution problem we required that the system blur function or the detector point source response function be spatially invariant. This is not true for the

Pho/Con as shown in Chapter 3. However, this simplifying assumption will not affect the following argument. The solution to the above problem requires the determination of that inverse filter  $b_{|j-i|}^{-1}(x,y)$  which, when convolved with the back projected image  $g(x,y)$ , yields the wanted  $f(x,y)$ . The solution is normally achieved by employing Fourier techniques and the convolution theorem, a technique which is now well established. The convolution expression can be written in a more concise form in the following way:

$$g_i(\bar{r}) = \sum_j^n [f_j(\bar{r}) * b_{|j-i|}(\bar{r})]$$

According to the convolution theorem the Fourier transform of  $g$  is equivalent to the product of the Fourier transforms of  $f$  and  $b$ , thus

$$G_i(\bar{p}) = \sum_j^n F_j(\bar{p}) B_{|j-i|}(\bar{p})$$

where  $G(\bar{p})$ ,  $F(\bar{p})$  and  $B(\bar{p})$  are the Fourier transforms and  $\bar{p}$  represents the two dimensional Fourier space. Solving for  $F_j(\bar{p})$

$$\sum_i^n G_i(\bar{p}) B_{|i-k|}^{-1}(\bar{p}) = \sum_i^n \sum_j^n F_j(\bar{p}) B_{|j-i|}(\bar{p}) B_{|i-k|}^{-1}(\bar{p})$$

$$F_k(\bar{p}) = \sum_i^n G_i(\bar{p}) B_{|i-k|}^{-1}(\bar{p})$$

where  $\sum_i^n B_{|j-i|} B_{|i-k|}^{-1} = \delta_{jk}$ . The inverse Fourier transform of  $F_k(\bar{p})$  yields the desired distribution  $f_k(x,y)$ . Various techniques

have been suggested which attempt to determine the filter function  $\bar{B}^{-1}(\bar{p})$  (Chu et al 1977, Tam et al 1978, Townsend et al 1978, Tam et al 1979, Hooper et al 1979, Pickens et al 1980, Tam et al 1980, Townsend et al 1980, Tam et al 1981). The success of these various techniques has been limited because of noise amplification which occurs in the inversion of the Fourier transform of the system transfer function. This is particularly pronounced when attempting to deblur images which are count limited. An additional complication, as a result of limited sampling angle, is that the spatial invariance of the system response function is only true for a limited region in space.

In recent years, iterative blur compensation techniques specific to the Pho/Con have also been investigated and proved to have some clinical use (Garcia et al 1980, Garcia et al 1981). Before describing our approach to the deblurring of Pho/Con images it is useful to briefly review some of the mathematical and numerical methods which have been thus far employed to deblur focal-plane tomographic images.

Chu and Tam (1977) have expressed the imaging process using Fredholm equations of the first kind. The convolution equation expressed in this way can be simplified provided that the kernel is space invariant. The spatial invariance of the scalar field representing the detector response function was preserved by defining a universal cone of detection whereby any photon emitted within the cone will be detected.

The convolution integral requires that the integration be carried out over all space. In this case one must measure  $g(\bar{r})$  over  $4\pi$  solid angle. This however, is not possible given the limited angular range of the detector system used. The computer simulation used a detector arrangement consisting of two planar multiwire chambers providing an opening angle of 90 degrees. This exceeds the allowed angular sampling of the Pho/Con which is limited to 60 degrees. In addition, the solution to the convolution equation is found to be unstable with respect to noise thus limiting the resolution of the reconstruction. The instability due to noise can be improved by selecting a scalar field sharply peaked (the ideal case being a delta function). For two plane detectors measuring coincident events this can be achieved by giving the greatest weight to the events which fall close to the edges of the acceptance cone rather than in the middle. The limitation in the sharpness of the response function is set by the reduction of available data resulting from further restricting the cone of detection. The authors attempted to remove the instability due to noise by modifying the scalar field (representing the PSF) to include an error function  $e(\bar{r})$ , which adds randomly to the measured data to give  $g(\bar{r}) + e(\bar{r})$  and imposing some restriction on the magnitude of  $e(\bar{r})$ . About the random nature of the error, it has been argued that with focal plane systems as described by the authors and similarly in the case of the Pho/Con, the noise is correlated rather than independent from point to point (R H

Hooper private communication). The Chu and Tam introduce a smoothness condition using the window

$$W(\bar{p}) = 1 / [ 1 + \lambda(2\pi)^2 \bar{p}^4 \times B(\bar{p})^{-2} ]$$

which depends on the filter itself. The Lagrange multiplier  $\lambda$  is chosen according to the noise in the measured data  $g(\bar{r})$ . The value of  $\lambda=0$  correspond to a sharp truncation of the filter.  $\lambda$  which determines the amount of smoothing in the solution  $f(\bar{r})$ , is obtained iteratively beginning with a small arbitrary value. After calculating an initial solution for the density distribution in momentum space the resulting error in the reconstruction is then compared to the total error due to statistical fluctuation in the data. The process is terminated according to a predetermined criterion.

The major points in the algorithm, after the selection is made of suitable reconstruction lattice spacing can be summarized in the following few points:

- 1) calculate of the point response function which minimize the instability in the solution
- 2) compute the Fourier transform of  $b(\bar{r})w(\bar{r})$  to give  $B(\bar{p})$ ;  $w(\bar{r})$  is a suitable window which minimizes leakage due to sharp cutoff in the response function
- 3) obtain  $G(\bar{p})$  from the Fourier transform of  $g(\bar{r})w(\bar{r})$
- 4) compute the solution in momentum space  $F(\bar{p})$  using the

smoothing filter to reduce the sensitivity to noise in the data

5) obtain  $f(\bar{r})$  from the inverse Fourier transform of  $F(\bar{p})$

The derivation of the distribution function in momentum space is limited to the region in space where both  $g(\bar{r})$  and  $b(\bar{r})$  exist. Discontinuities in the momentum space due to the vanishing value of  $B(\bar{p})$  makes the recovery of the distribution function  $f(\bar{r})$  impossible in the absence of a priori information. Tam et al (1979) make use of the fact that the extent of the object is finite to remove the indeterminacy in  $F(\bar{p})$ . According to the authors this can be done since the Fourier transform of a finite object is an entire function and as such it can be recovered in the complex plane by knowing the function in a finite continuous line segment. The value of  $F(\bar{p})$  can be extended to the missing cone using an iterative approach as described pointwise below:

- 1) from the limited value of  $F(\bar{p})$  obtained where  $B(\bar{p})$  is non zero produces an estimate of  $F(\bar{p})$
- 2) compute the inverse Fourier transform to yield an estimate of  $f(\bar{r})$  in the object space. The values outside the extent of the object are set to zero
- 3) the Fourier transform of the new estimate of  $f(\bar{r})$  gives a new  $F(\bar{p})$  whose value are set equal to the

original value of the distribution function in  $\bar{p}$  space.

4) repeat cycle

In the iterative process the object is manipulated back and forth between the object space and the Fourier space. In the simulation study in presence of noise the expression of  $F(\bar{p})$  is modified to include noise according to the method devised by Chu and Tam. According to these authors the main limitation results from noise in the data which degrade the quality of the image. This is a particularly serious problem when using detectors subtending a small solid angle. According to the authors adequate reconstruction is obtained with a solid angle of 4 steradians. The fidelity of reconstruction could be further improved if more a-priori information about the object was available.

In the techniques employed by Townsend et al (1978) and (1980) the problem of reconstruction for positron cameras with limited angular acceptance is again based on a Fourier deconvolution method. To reconstruct the three dimensional matrix of volume elements initially one takes the back-projection of the two-dimensional projection into the three dimensional object space. A three dimensional filtering is then applied to remove distortion caused by the missing projection data. This approach minimizes the noise amplification associated with filtering. In dealing with the problem of missing data due to the limited extent of the



acceptance angle, the authors in an early paper (Townsend et al 1978) represent the system response by a symmetric square matrix. The deconvolution process requires the inversion of such a matrix. At low spatial frequencies a complex coupling of the measured and missing frequencies produces a matrix such that not all the columns and rows are independent (low rank). The authors describe a generalized procedure employing eigenvalues and singular value decomposition of the transfer function. In the inversion of the transfer function large fluctuations near singularities, resulting from small eigenvalues, are removed by using only values which are above a certain lower bound. This allows them to set the lower bound in the numerical value of the elements of the inverse transfer function, thus controlling the noise propagation in the deblurred image.

A Fourier deconvolution approach followed in a second paper (Townsend et al 1980) was preferred since it allowed one to distinguish between measured and unmeasured frequencies. The basic assumption remained that the back-projection of events from a single point source yields a conical distribution which is space invariant. A close form derivation of the filter function can then be obtained by observing that within the acceptance cone the impulse response function varies as the inverse square of the distance from the point source. The filtering process is simplified and summarized into few steps as follows:

- 1) a simple back - projection reconstruction produces a

blurred image

- 2) the blurring is removed by filtering the distribution with a predetermined three dimensional filter function (similar in one dimension to a ramp filter)
- 3) use a Hanning filter to reduce the ringing caused by the sharp cutoff of the window in step 2

Hooper et al (1979) considered the removal of out-of-plane blurring, from computer simulated images, by combining smoothing with a linear differential operator. The point source response function was first smoothed in the x and y directions before the application of the differential operator. As suggested by the authors, the presence of noise in the real data can cause some difficulty in the calculation of the derivatives which are obtained numerically.

In the iterative technique implemented by Garcia and co-workers (1980, 1981) the deblurring is a post-processing approach which begins with the image obtained from a single back-projected image. The execution starts at any one plane with the count above a certain threshold assigned to that specific plane. From the location of the activity a blur pattern is then generated through the remaining planes with the blurred value subtracted from each of the neighbouring planes. Few details are given about the method.

The investigation of a deblurring algorithm suitable for our system, we preferred to follow a numerical iterative

approach. This is because Fourier methods used to define the filter function greatly magnify the noise due to the factor  $1/B(\bar{p})$ . In the case where the noise was filtered, as in the method put forward by Chu and Tam (1977), while the noise at high frequencies can be suppressed, the information becomes distorted at low frequencies. The recovery of the missing data using an iterative technique, as suggested by Tam et al (1979), reduces the problem of noise propagation and offers an adequate reconstruction provided that the detection system subtends a solid angle of 4 steradians. Each Pho/Con detector subtends a solid angle of approximately 3 steradians, which is lower than the minimum value required by the method proposed by Tam et al (1979).

We have investigated the use of a post-processing iterative deblurring algorithm for the removal of off-plane activity from the Pho/Con images. The approach used is substantially different from the technique employed by Garcia and co-workers. In our approach, from the single back projected images we determine a series of first estimates of the true activity distribution for each of the reconstructed planes. Using the measured point spread function (PSF) of the detector a new blurred image is then produced by taking the convolution of the first estimate with the system response function, PSF. A comparison with the original blurred image allows one to refine the first estimate. The procedure is then repeated in an iterative fashion. The difference square (DFSQ) between the initial blurred images and the new blurred distributions obtained at

each iteration is used to monitor the convergence.

#### 4.3 Iterative deblurring with pixel refinement of a first estimate

The algorithm described here is a post-processing deblurring approach which performs a pixel by pixel correction of an initial first estimate of the activity distribution for each image plane. In the implementation, the first step in the deblurring procedure requires the reconstruction of the activity distribution using simple back projection. These images are obtained using the expressions for the coronal images described in section 4.3. The number of reconstructed equally spaced planes is 31. For the deblurring of clinical images this number could be reduced to approximately 10 planes since the system resolution (3.5 cm) as a function of depth prevents the differentiation of structures at plane separation less than the full width at half maximum of the point spread function.

As indicated in Figure 4.3 the deblurring process begins with the initial estimate  $e_i^0(x,y)$  of the true activity distribution  $f_i(x,y)$  for all image planes  $i$ . This is obtained from the blurred images  $g_i(x,y)$  by setting a lower threshold at a level which would remove a large portion of the noise due to blurring and preserving much of the information with respect to the density distribution  $f_i(x,y)$ . The thresholding is purely arbitrary, and a way to

optimize the lower level cut off in the blurred images must be devised, since its value affects the difference square (DFSQ) conversion as shown later.

The 31 image planes, first estimates are subsequently blurred with the system point spread function. For simplicity it was assumed that the system response function is spatially invariant. For the Pho/Con this is not the case, as shown in the resolution measurements, where the PSF exhibits a strong dependence on the distance between the source and collimator. The new blurred images for the 31 planes obtained using the estimate can be expressed in the following way,

$$g_i^1(x,y) = \sum_j^n [e_j^0(x,y) * b_{|j-i|}(x,y)]$$

where  $i = 1, 2, \dots, 31$  and  $j = 1, \dots, 31$ . In the expression the superscripts represent the order in the iteration with 0 (zero) being the initial value. The blurred images thus obtained are then compared to the original simple back projected images  $g_i^0(x,y)$  to produce a pixel by pixel correction term to be applied to the initial estimate  $e_i^0(x,y)$ . In general, for the  $m$ th iteration the above expression can be written as

$$g_i^m(x,y) = \sum_j^n [e_j^{m-1}(x,y) * b_{|j-i|}(x,y)]$$

The first step in the calculation of the correction term requires the minimization of the square of the difference

between the two sets of images. This is done by considering the total number of image planes. The DFSQ value is given by,

$$(DFSQ) = \sum_i^n (g_i^o - c g_i^m)^2$$

for all pixels x,y in each image plane. c is a constant such that DFSQ is a minimum. This is equivalent to the statement that there exists a value for c such that

$$d(DFSQ)/dc = 0$$

It can be shown that DFSQ is a minimum when

$$c = \frac{\sum_i^n (g_i^m g_i^o)}{\sum_i^n (g_i^m)^2}$$

The value of c, which is calculated at each iteration, is used as a renormalization factor for the new blurred images. In addition it guarantees that the global DFSQ at each iteration is a minimum. The correction factor is then simply obtained in terms of the ratio between the pixel counts in the initial image  $g_i^o$  and the new counts  $cg_i^m$  for the mth iteration. The estimate of the activity distribution is then adjusted according to the following expression

$$e_j^{m+1}(x,y) = e_j^m(x,y) \frac{g_i^o(x,y)}{c g_i^m(x,y)} \frac{\sum_i^n g_i^o(x,y)}{\sum_i^n c g_i^m(x,y)}$$

In the equation  $\sum_i^n g_i^o(x,y) / (\sum_i^n c g_i^m(x,y))$  is an additional constraint which is introduced in order to renormalize the new set of images  $g_i^m$  to the total number of counts in the initial set  $g_i^o$ . The new set of estimates is then convoluted again with the system point spread function thus repeating the procedure in an iterative fashion. The procedure will continue until the DFSQ reaches a minimum value or a preset low value. The iterative deblurring process is summarized in Figure 4.3.

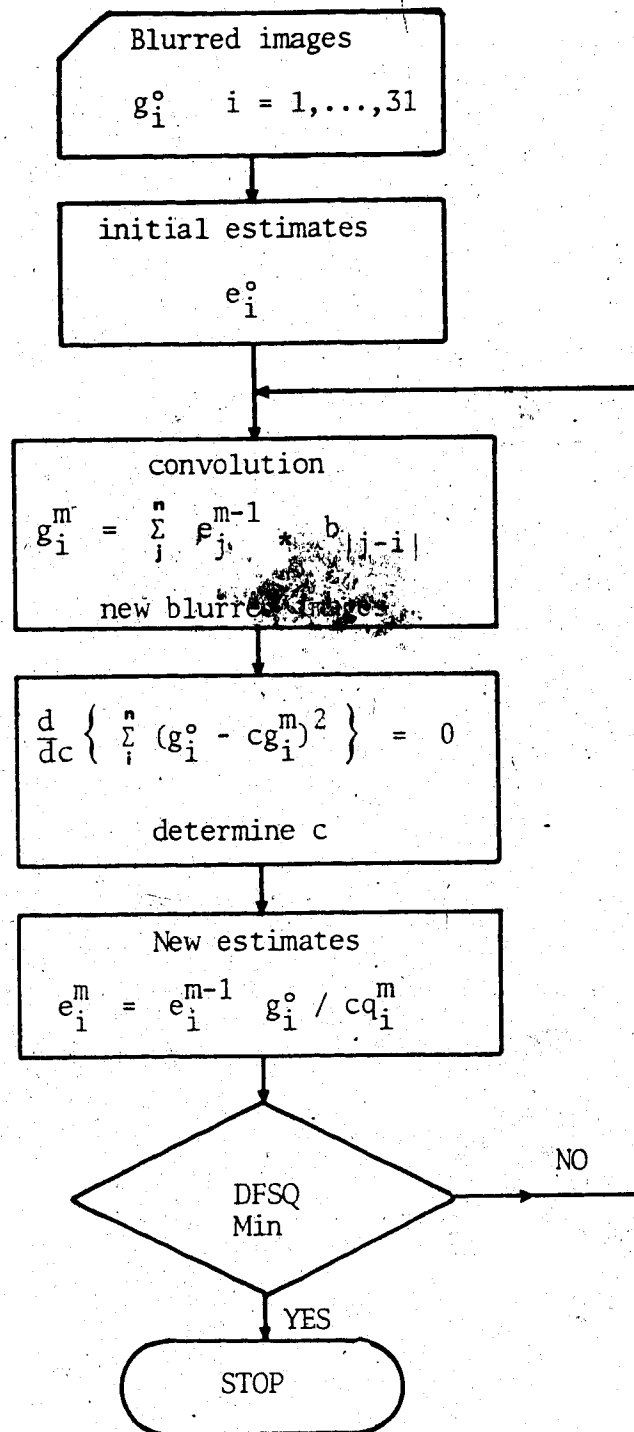


Fig. 4.3 Flow chart of the deblurring algorithm



## CHAPTER 5

### 5.1 Deblurring with a computer simulated noiseless phantom

The deblurring procedure was tested using a mathematical phantom consisting of an 8 x 8 pixel matrix within 8 of the 31 image planes, with each image consisting of 31 x 31 pixels. The central 8 x 8 x 8 elements of the simulated object volume were assigned a minimum intensity value of one. Within this volume, four planes with a 4 x 4 array of pixels, offset as shown in Figure 5.1 to avoid symmetry, were given the intensity value of two. In the computer simulation the blurred images were obtained by convolving the phantom shown in Figure 5.1 with the measured PSF of the Pho/Con detector. This PSF was measured at the focal distance of the collimator (i.e. 8.9 cm from the collimator face) and for convenience it was assumed to be independent of the distance from the detector (spatially invariant). Figure 5.2 shows images of planes 13 through 20 of the phantom, with intensity levels 1 and 2, as displayed by a Gamma-11 system using TOMDIS (Hooper R. 1982), a program designed to display 3-dimensional tomographic images. Figure 5.3 displays 16 of the 31 blurred image planes obtained from the convolution of the phantom with the system PSF. These images show clearly the negative effect of blurring which obscures the two activity levels in the

object. The blurring masks the original information and causes a contribution to the outlying planes which in turn could be misrepresented as true activity.

In testing the deblurring technique, the logarithm of the DFSQ value, calculated at each iteration, was plotted to show the speed of convergence. Again the DFSQ represents the sum of differences squared between the original blurred image and the new image obtained by blurring the estimated activity distribution. As shown in Figure 5.4, an initial fast decrease in the log of the DFSQ value is followed by a long tail with a small slope indicating a very slow convergence. It appears that beyond the 10th iteration very little is gained in recovering the original distribution function. Thus alternate correction factors should be introduced in order to speed up the DFSQ convergence after the first few iterations. In Figure 5.5 the phantom blurred images are shown with the lower count threshold set at 0.3 of the maximum pixel count in the image planes. These images represent the initial estimates which are used in the deblurring routine. Figure 5.6 through Figure 5.8 show the effect on the blurred images of the deblurring algorithm after 5, 10, 20 iterations. Noticeable in these images is the increased contrast between the two intensity levels in the original phantom which can be distinguished after only a few iterations. Also noticeable are streaking artifacts which occur at the corners of the images. These are probably caused by the sharp increase in the intensity levels after the first few iterations. This effect is slightly

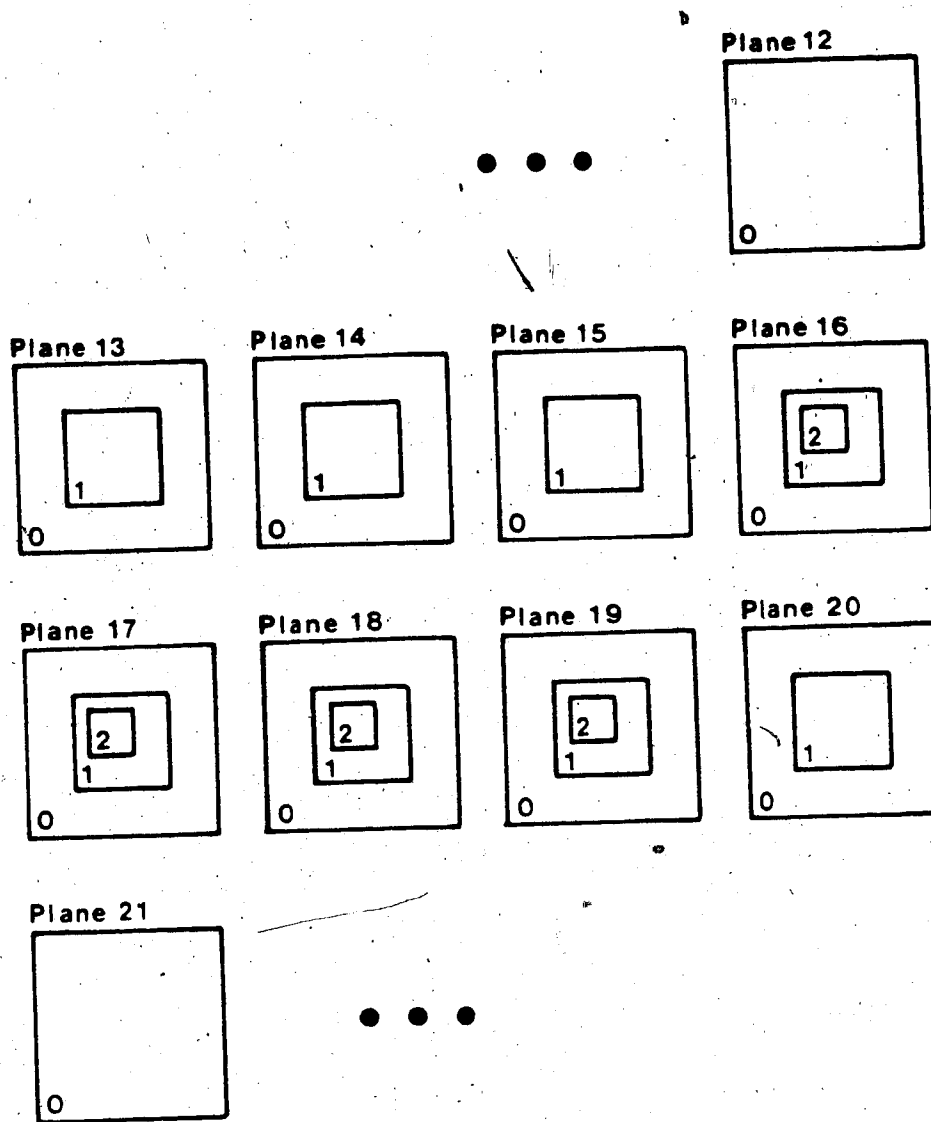


Fig. 5.1 Phantom image planes showing the intensity levels 0, 1, and 2.

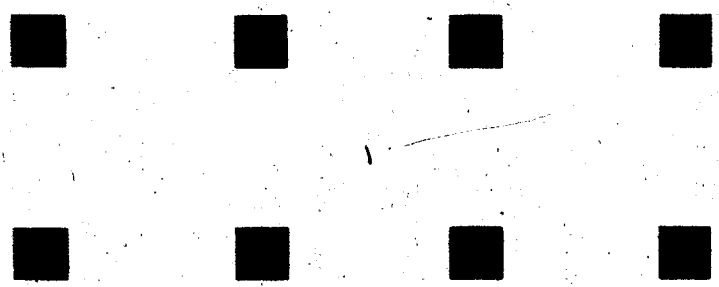


Fig. 5.2 Image planes 13 through 20 of the phantom as displayed by the Gamma-11 system.

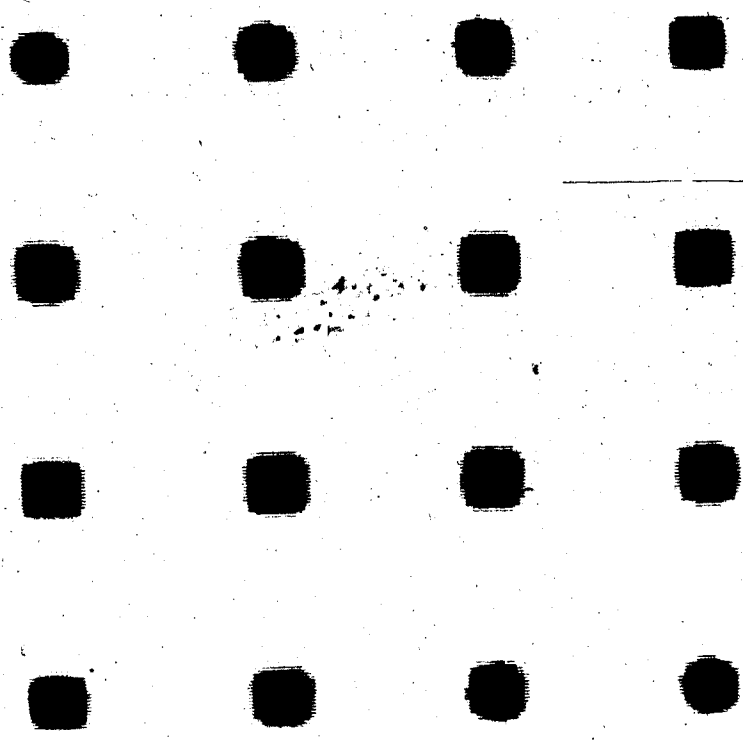


Fig. 5.3 Blurred image planes 9 to 24 scaled to the maximum pixel count in the set of images.

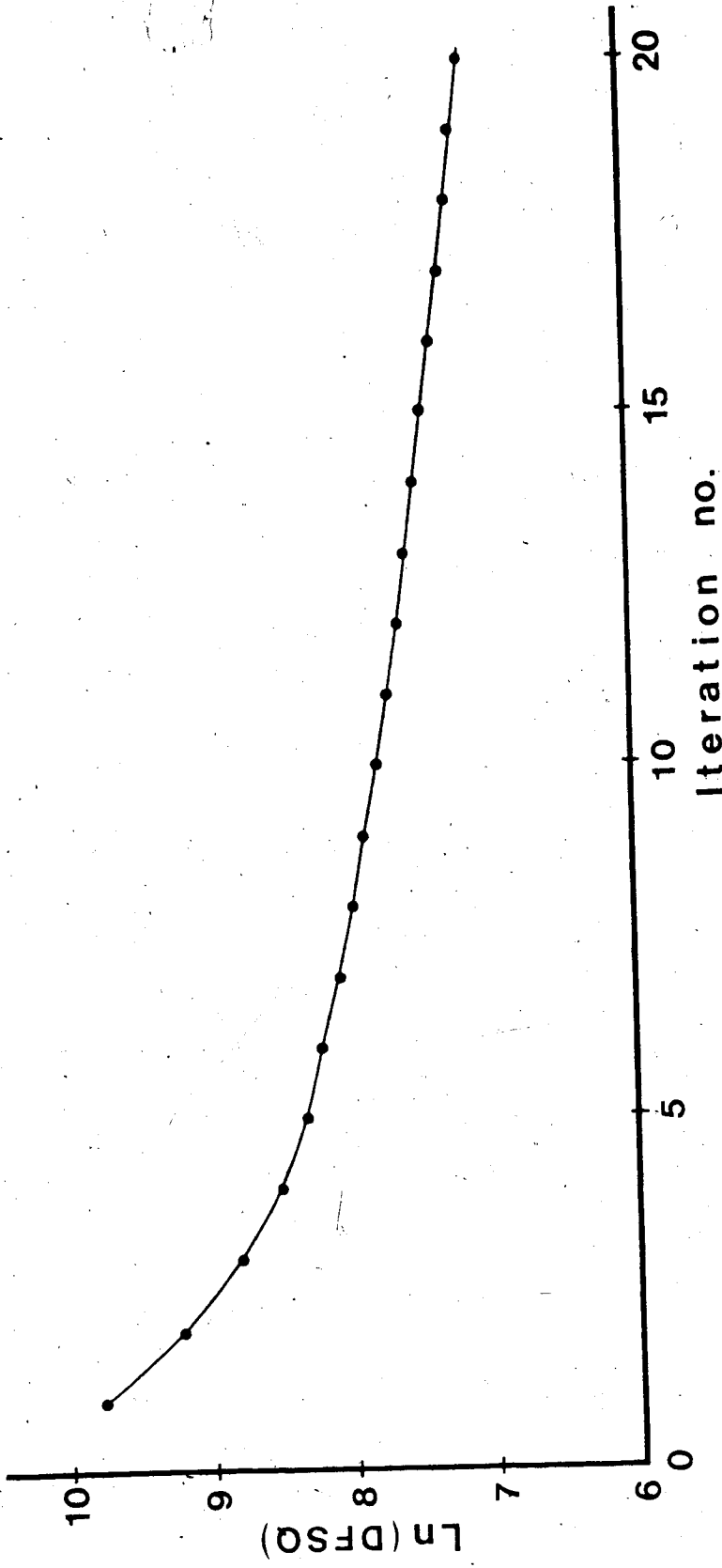


Fig 5.4 Change in the DFSQ value showing the convergence of the algorithm in the deblurring of a noiseless images.

diminished after a larger number of iterations, as shown in Figure 5.8.

To demonstrate the effect that the threshold level has on regaining the true distribution, two images were obtained using a cut-off level of 0.25 and 0.35 of the maximum count. Figures 5.9 and 5.10 show the deblurred images obtained with 0.25 and 0.35 threshold values respectively. The image obtained with the 0.25 value appears to be no different from the image obtained using the 0.3 threshold level and the same number of iterations. In the case of Figure 5.10 this is not true since some of the information has been lost at the edges of the image planes 13 to 15 and on plane 20. Figure 5.11 shows the effect of different thresholds on the DFSQ convergence. The higher threshold cut off appears to improve the convergence even after an initial higher value for the DFSQ.

## 5.2 Performance of the deblurring algorithm in the presence of noise

The performance of the deblurring technique in the presence of noise was tested using the same computer simulated phantom described in the above section and with a suitable test phantom, which was imaged with the Pho/Con, producing a set of 31 image planes. In the computer

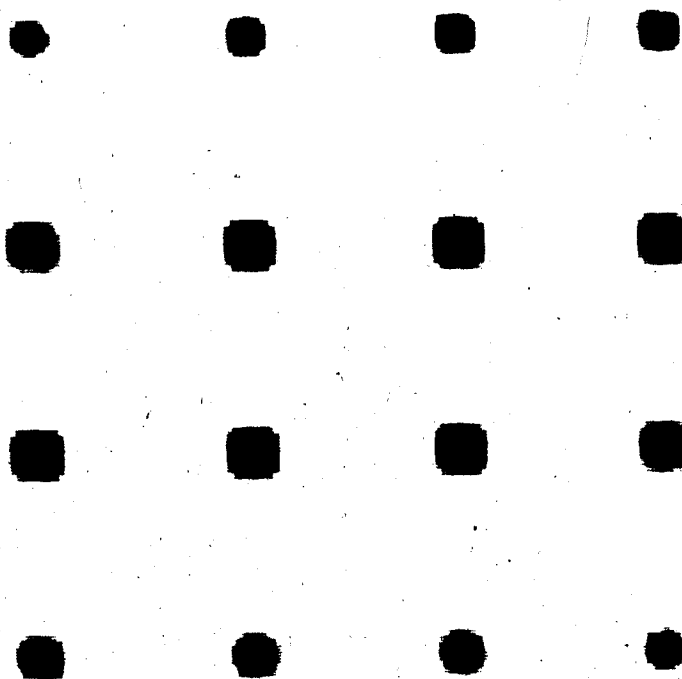


Fig. 5.5 Initial estimate of the blurred image for planes 9 through 24.

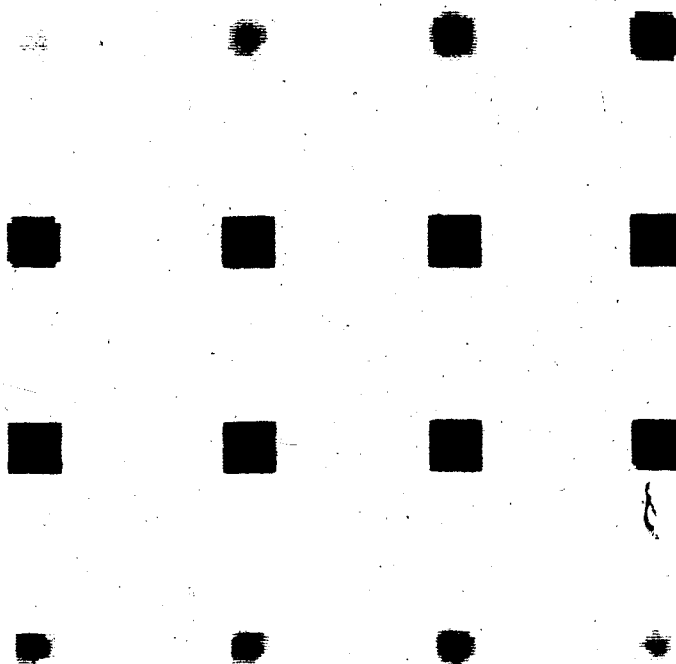


Fig. 5.6 Estimate after 5 iterations.

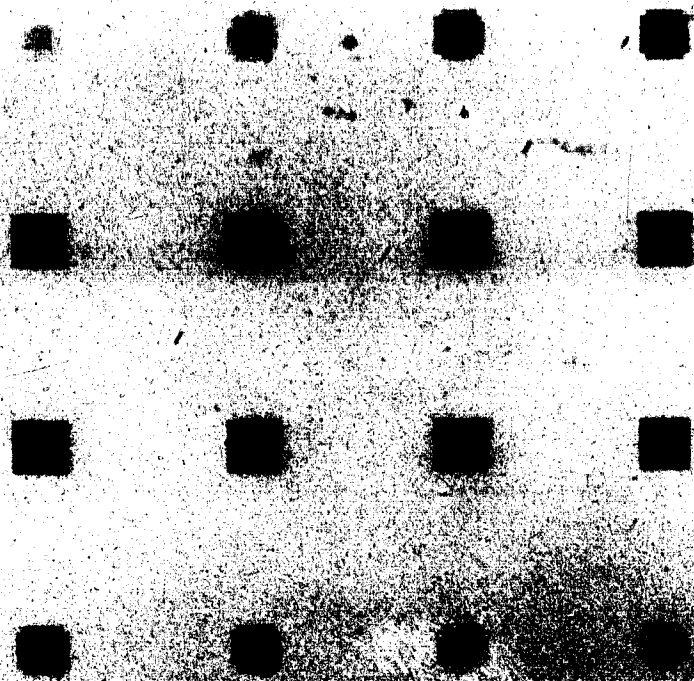


Fig. 5.7 Estimate after 10 iterations.

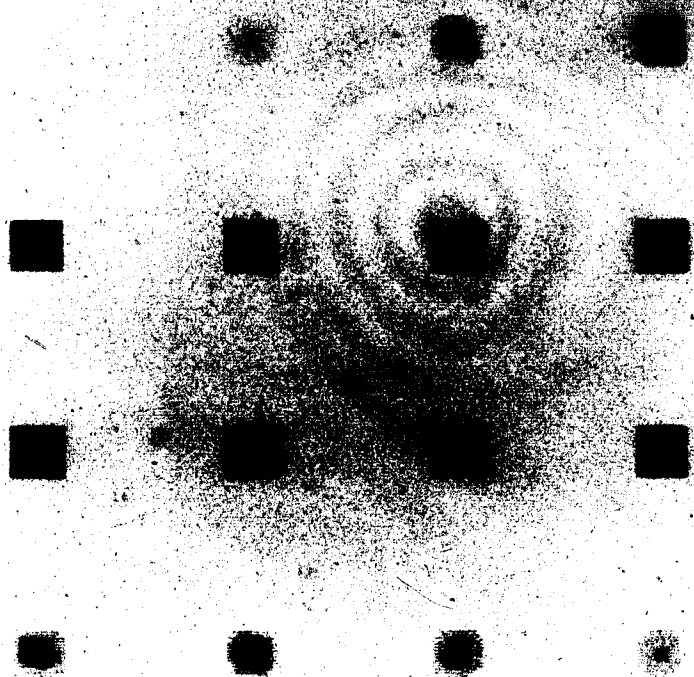


Fig. 5.8 Refined initial estimate after 20 iterations.



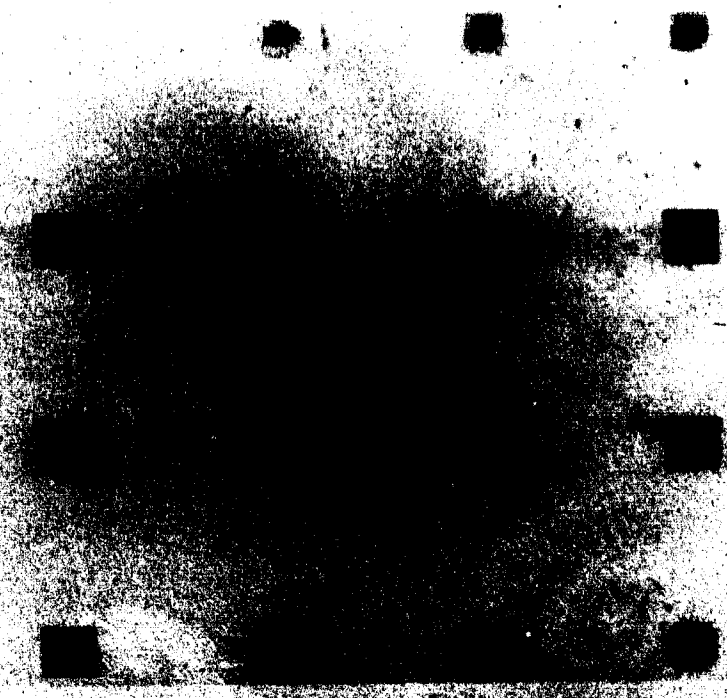


Fig. 5.9 Images of planes 9 through 26 after 10 iterations with a threshold of .35. The background has been cut off.



Fig. 5.10 Images of planes 9 through 26 after 10 iterations with a threshold of .35.

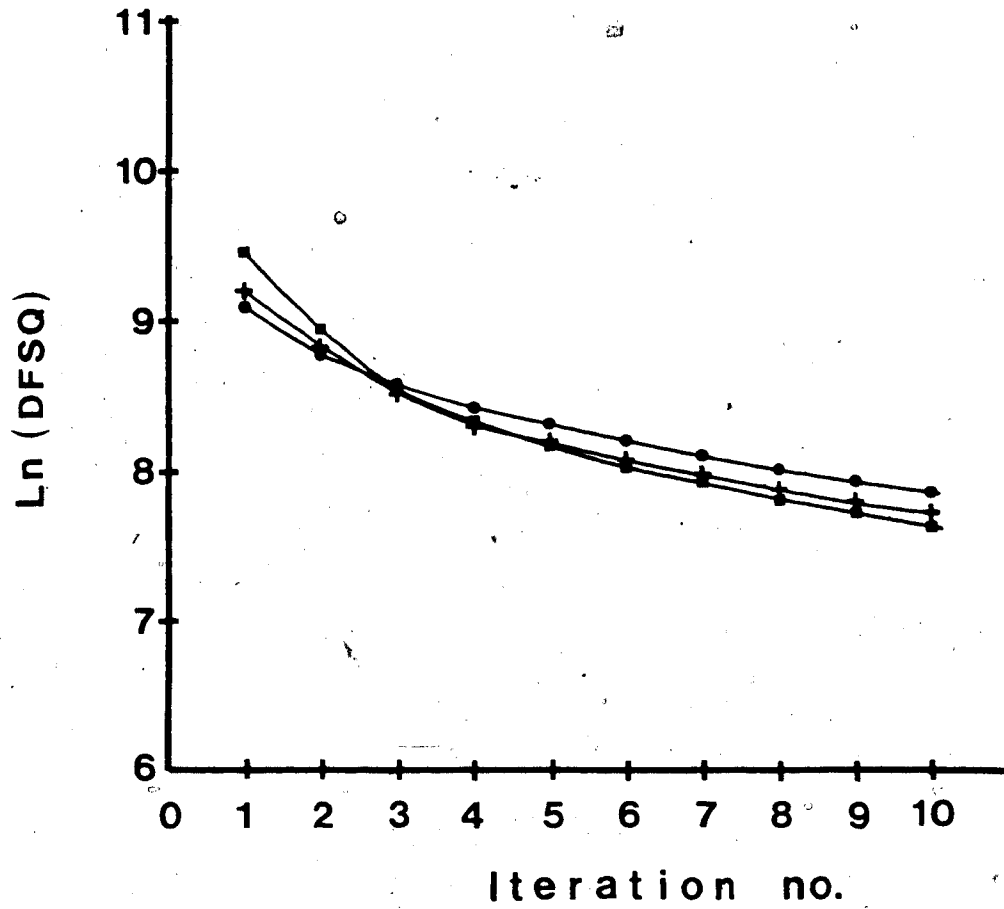


Fig 5.11 Convergence of the algorithm for the threshold values (●) 0.25, (+) 0.3, and (■) 0.35.

simulation, the noise in the image was considered to be spatially independent similar to the method of Chu and Tam (1977). With this approach, the various image planes are unaffected by the noise in the surrounding planes. This technique however, might not be consistent with the way true noise is introduced in Pho/Con images, where statistical fluctuations in the reconstructed planes are strongly correlated by the blur function.

The levels of noise considered were estimated from the maximum number of counts expected in typical Pho/Con imaging procedures. The three levels of noise considered varied from a low image count of 100 counts maximum in a single pixel, as one would expect in a Ga-67 scan to an intermediate value, slightly in excess of 1000 counts, which is likely to occur in bone imaging using agents labelled with Tc-99m. A third level of 10000 counts in a single pixel was also included in the analysis, although never observed clinically. The three count levels provided images with statistical error of 10%, 3%, and 1% respectively. The error function was calculated using the appropriate gaussian curves with the standard deviation defined by the above image counts. Each gaussian curve, extended to three standard deviations, was divided into 100 equal probability areas. The error in each pixel in the blurred image was assigned using a random number generator which was used to map the argument of the error function to the individual

pixel in the blurred image.

For the correlated noise study, images of a phantom consisting of two cylinders containing two levels of activity in the approximate ratio of 2:1 were obtained by imaging a test phantom with the Pho/Con. The smaller of the two cylinders, containing the higher level of activity, was placed off-center within the larger one, as indicated in Figure 5.12. Also indicated in the figure are the position of the reconstructed image planes, relative to the two cylinders. The separation between planes is constant at 0.81 cm. The matrix size of 31x31 pixels with a single pixel dimension of 0.54cm x 0.54cm, provides an adequate scan area to cover the entire size of the phantom. The phantom was scanned at three different scan speeds, thus yielding three different count rates. The digitized Pho/Con signals were stored on disk in list mode. From the list data files computer reconstruction using a simple back-projection allowed one to produce blurred images of the test phantom. In the reconstruction the point spread function of the system was kept constant, at its best value measured at the focal plane. These images allowed the deblurring algorithm to be tested in the presence of true noise.

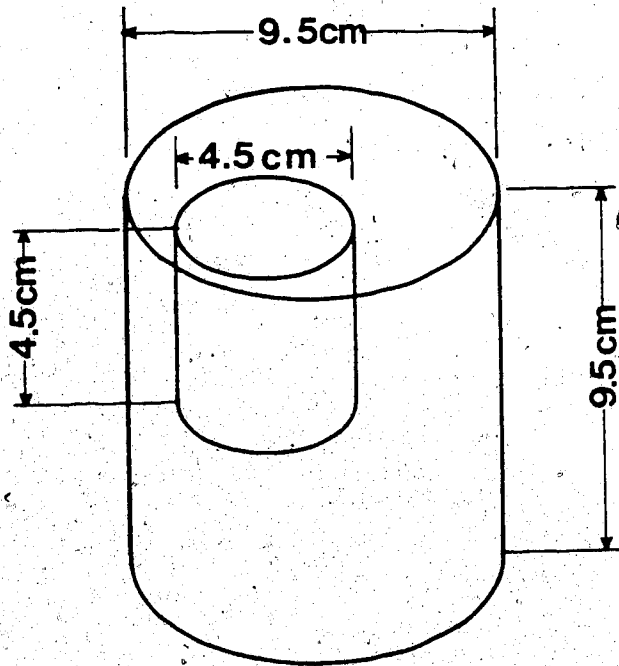


Fig 5.12 Simplified diagram of the real phantom used to test the deblurring routine. The graph shows dimensions and relative position of the two cylinders.

### 5.2.1 Deblurring of computer simulated phantom with noise

Using the deblurring algorithm described in Chapter 4, an attempt was made to deblur noisy images with statistical fluctuations varying from 1 to 10%. The performance of the algorithm was again tested using the convergence of the global difference square between the original set of blurred images and the new one obtained by blurring the adjusted estimate of the true activity distribution. Figure 5.13 shows a plot of DFSQ versus the number of iterations. For convenience the logarithm of DFSQ is used in order to accommodate a larger range of DFSQ values. As clearly shown in Figure 5.13, the increase in the non-correlated noise level in the image shifts the curves to higher values. This slow decrease in the logarithm of DFSQ can be attributed to the increased noise in the new estimate, introduced by the convolution operation at each iterative step. The higher the value of DFSQ the more likely the new estimate will lose all the information contained in the initial blurred image. Moreover, with increasing statistical noise, after few iterations very little is gained in the recovering of the original activity distribution.

Figure 5.14 shows the initial estimates of plane 17, which contains intensity levels 1 and 2 together with the final estimates of the distribution for the three selected noise levels in the images. The initial estimates were obtained using a lower threshold level which produced faster convergence in the values of DFSQ. In the case of the image

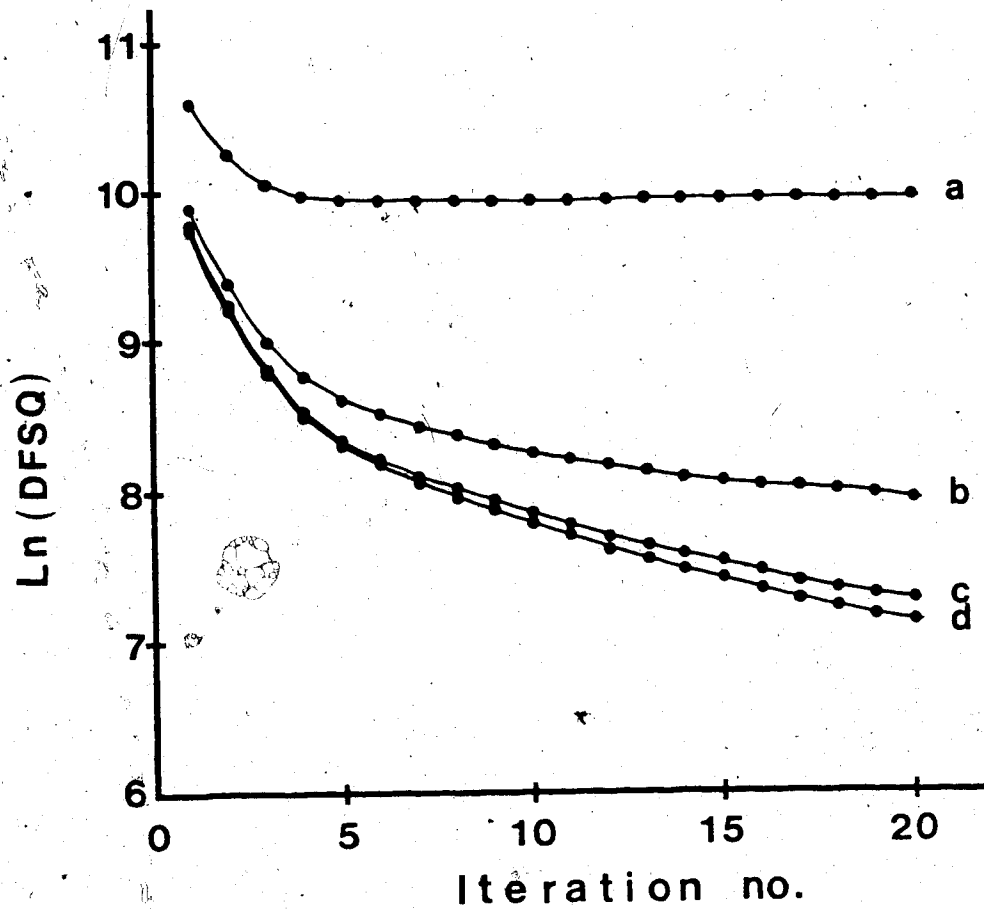


Fig 5.13 Convergence of the DFSQ value for blurred images of the computer simulated phantom with statistical count error of (a) 10%, (b) 3%, (c) 1%, and (d) no error.

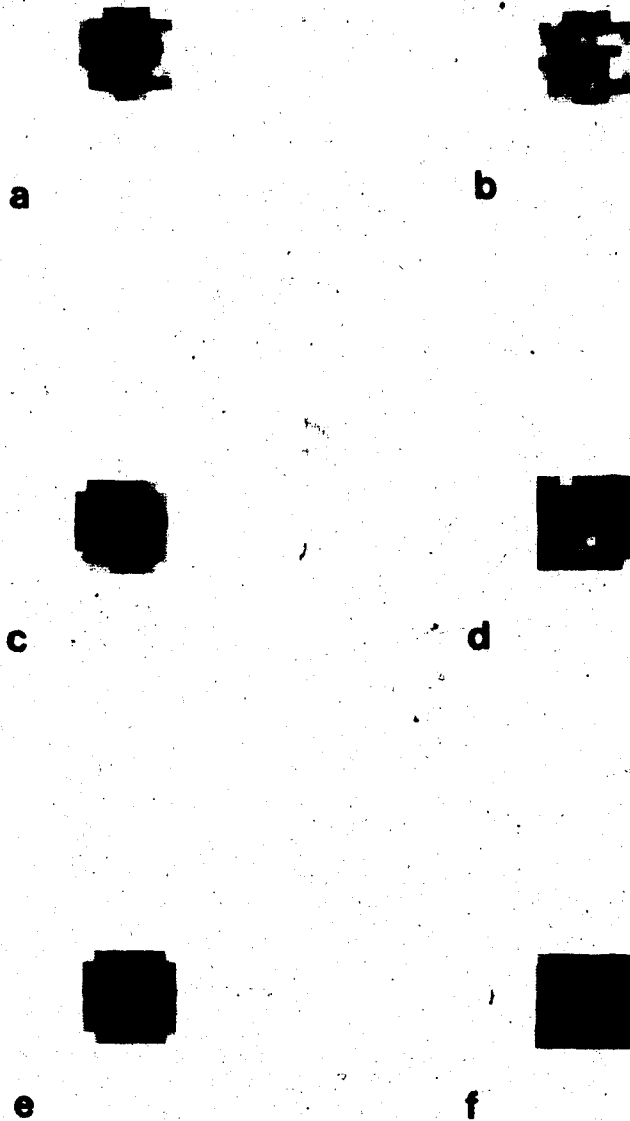


Fig. 5.14 Image of plane 17 of the computer simulation of phantom with varying uncorrelated statistical noise. 10% count statistics a) initial estimate, b) image after 4 iterations; 3% count statistics, c) initial estimate, d) image after 10 iterations; 1% count statistics, e) initial estimate, f) image after 10 iterations.



with the 10% statistical noise (Figure 5.14 a, b) the two levels of intensity present in the phantom are not easily identified on either the original blurred image nor with the estimate obtained after four iterations. For this image the deblurring process was terminated after four iterations since the DFSQ value would not change for increasing numbers of iterations. With improved statistics (Figure 5.14 c, d) the deblurring process appears to slightly improve the contrast between the two intensity regions. However the propagation of noise distorts the image by producing areas of high and low counts. As shown on the three estimates the increased amount of noise makes the deblurring process progressively more difficult. It appears that for images with counts lower than approximately 1000 counts per pixel the deblurring process fails to produce any improvement, leaving the original blurred images more suitable for the evaluation of Pho/Con tomographic planes.

It is evident that for non correlated noise the present deblurring algorithm fails to effectively remove the off-plane activity in the images. In addition, it tends to amplify the noise which arises purely from statistical fluctuation in counts, as clearly shown by the lower count images.

### 5.2.2 Deblurring phantom images with correlated noise

The clinical phantom employed to test the deblurring routine shown in Figure 5.12 was imaged with the Pho/Con using three different scan speeds allowing the maximum count in each of the reconstructed sets of coronal images to be varied. The maximum counts in a single pixel registered for the three sets of longitudinal planes were 327, 698, 1560. These are typical counts per pixel normally encountered in clinical studies suitable for the Pho/Con tomographic scanner. Figure 5.15 shows the variation of the DFSQ, on a logarithmic scale, versus the number of iterations. Evident in all three curves is a minimum value which is reached after only few iterations. The three curves are very similar in shape, but show different initial values dependent on the number of non zero pixels in the initial estimates. For these real phantom images the deblurring process was terminated whenever the value of DFSQ reached a minimum. Figure 5.16 through 5.18 show images of the initial test phantom with a lower threshold cutoff of 0.15 of the maximum count, together with the final estimate obtained after that number of iteration for which the DFSQ value is a minimum. The 16 planes displayed in these figures, image planes 7 through 22, cover the entire phantom volume. The higher activity volume occupies approximately 5 planes, including planes 12 to 16.

In the images with low counts the noise is enhanced as was in the case of uncorrelated noise. There is however

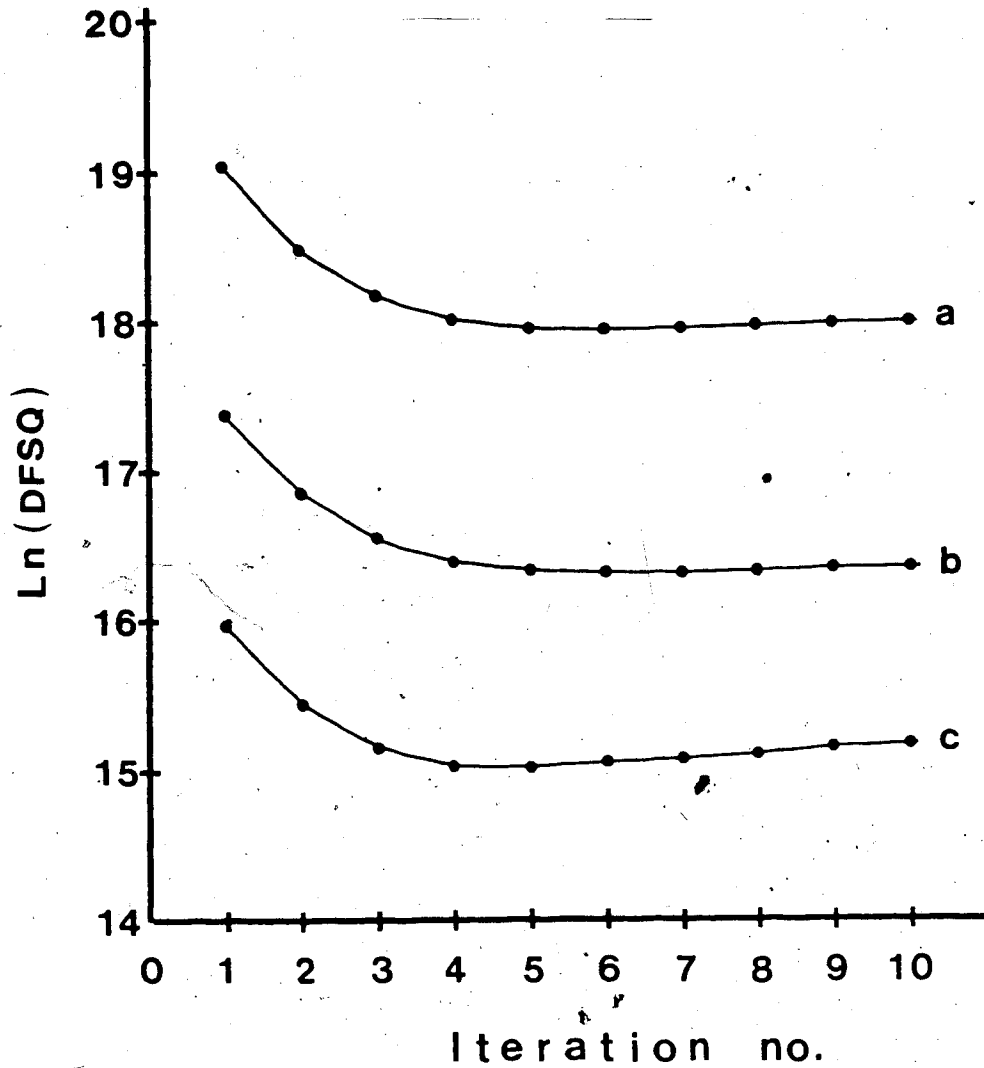


Fig 5.15 Change in the DFSQ value for images of the real phantom with maximum pixel count of (a) 1560 counts, (b) 698 counts, and (c) 327 counts.

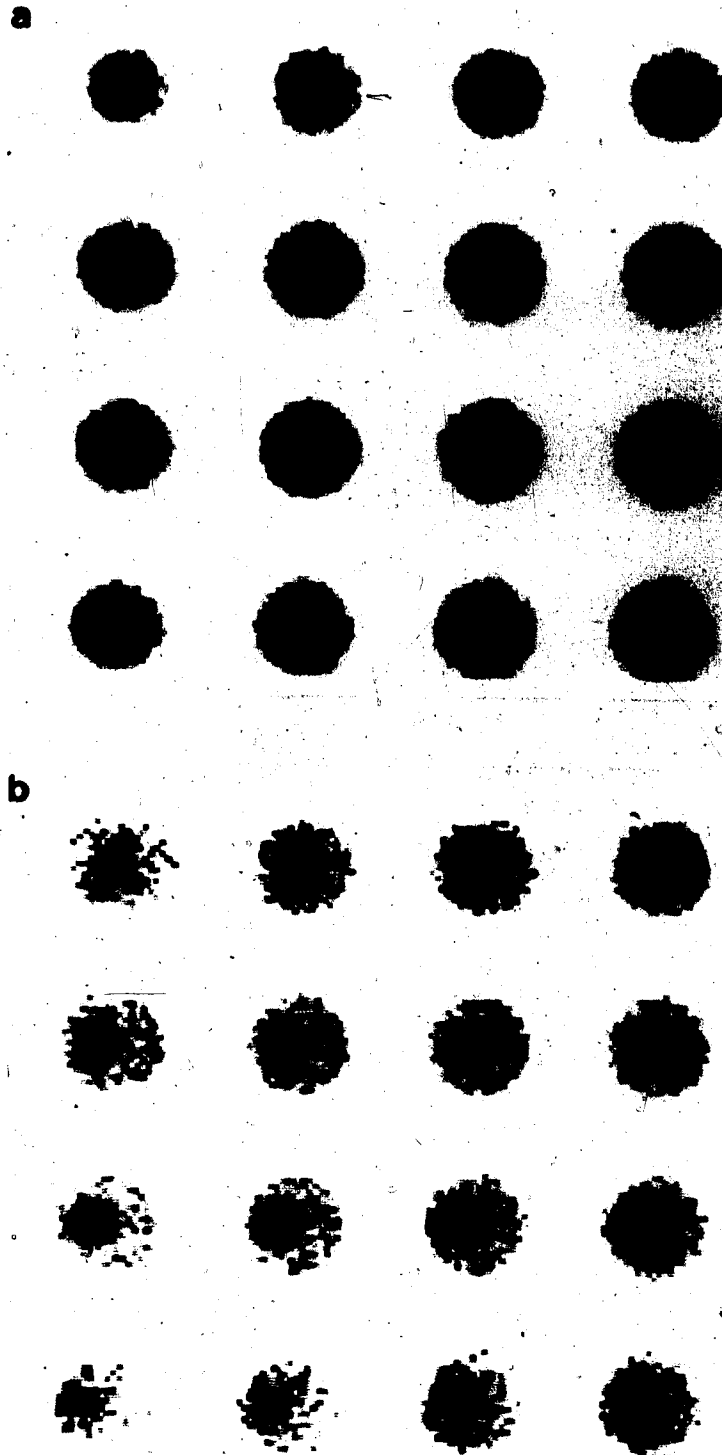


Fig. 5.16 Images of planes 7 through 22 of the test phantom with maximum pixel count of 327, a) initial estimates b) images after 5 iterations.

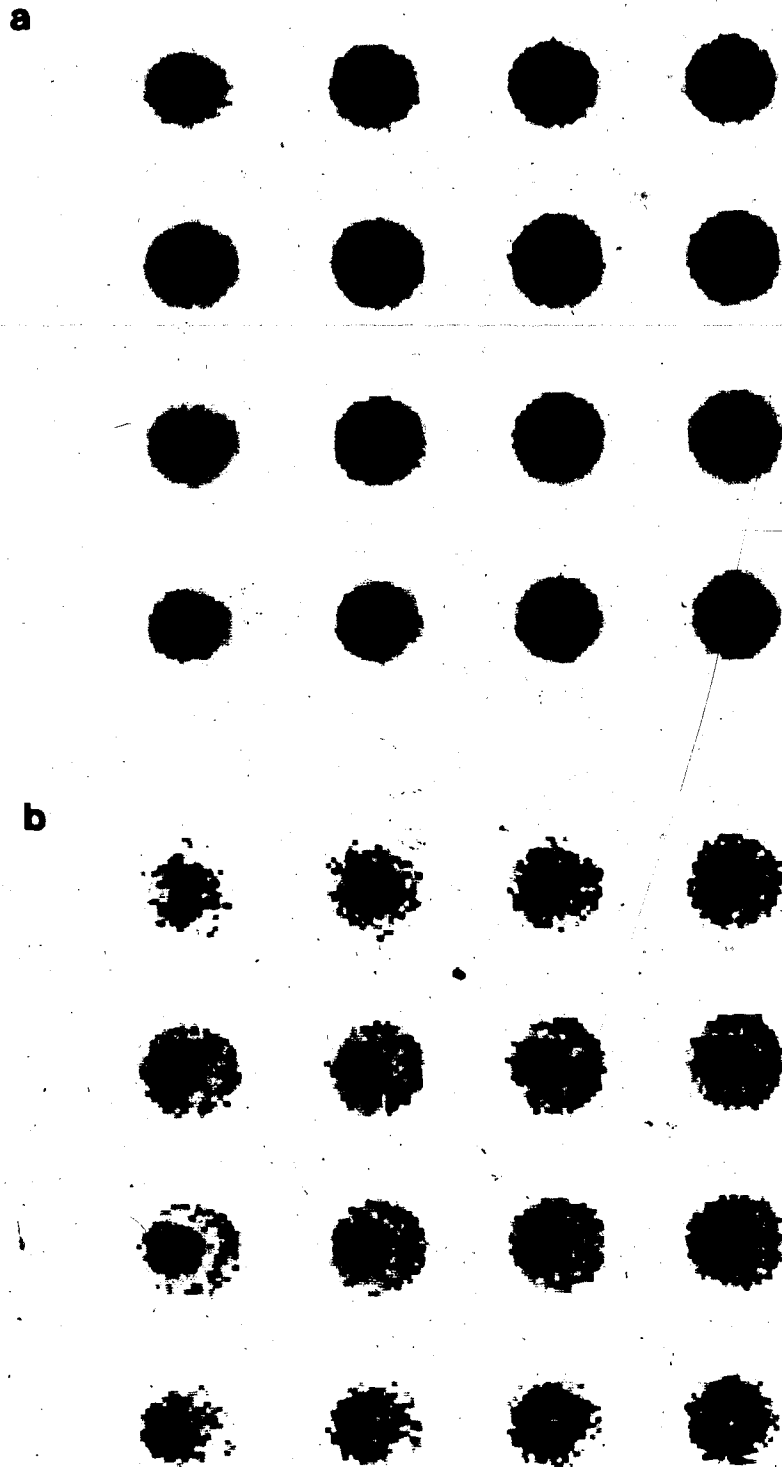


Fig. 5.17 Images of planes 7 through 22 of the test phantom with maximum pixel count of 698, a) initial estimates b) images after 6 iterations.

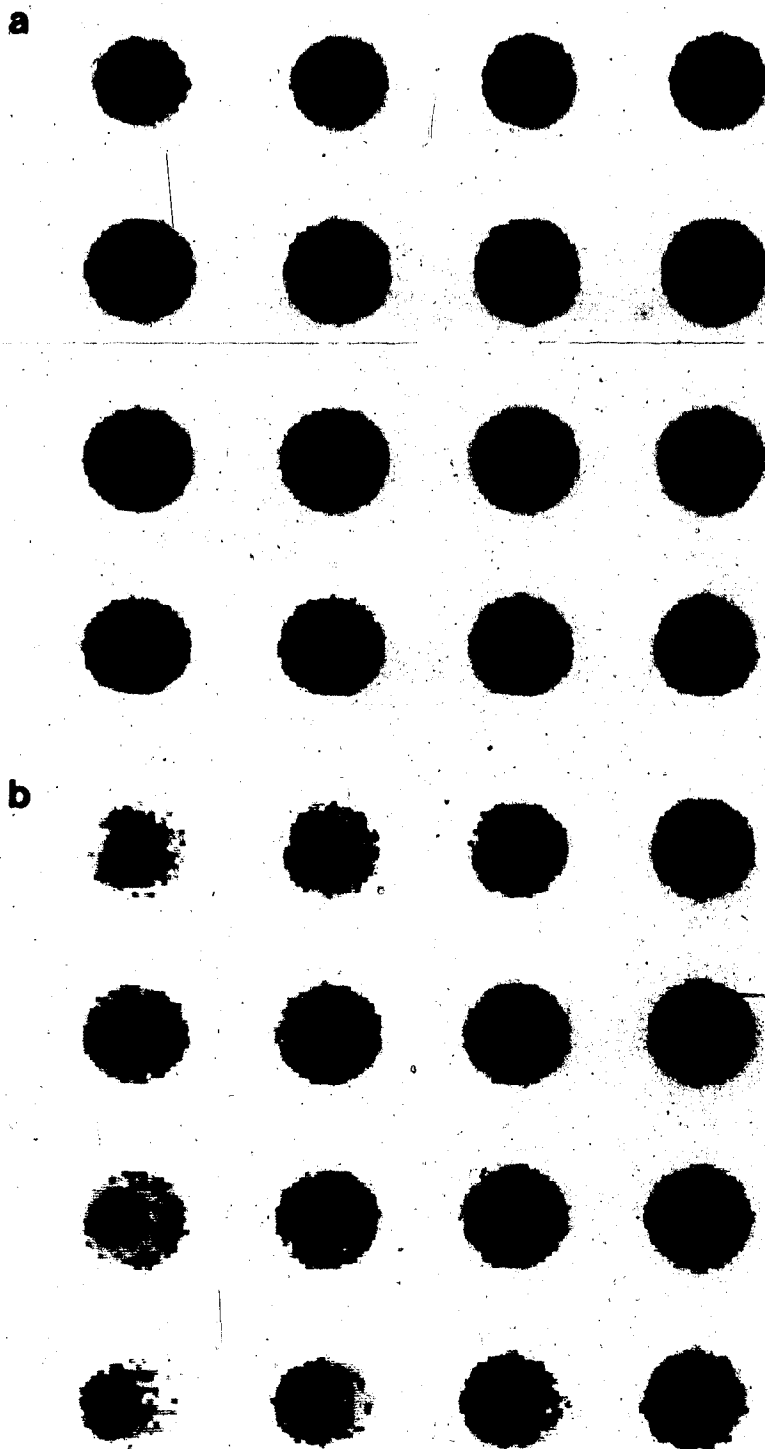


Fig. 5.18 Images of planes 7 through 22 of the test phantom with maximum pixel count of 1560, a) initial estimates b) images after 6 iterations.

some edge enhancement which helps to differentiate the two regions of high and low activity. In all of the images there is a decrease of blur distortions in the outer planes reducing the shadow of the higher activity region projected on these planes by the system blur function. The noise propagation appears to be less pronounced with improved statistics in the image as shown in Figures 5.17 and 5.18. Noticeable in these images, and particularly in the deblurred images, is a raster artifact which occurs at the focal plane of the detector. This artifact is due to the finite index width of the scan.

## CHAPTER 6

### 6.1 Conclusion And Discussion

Recent developments of tomographic techniques employing rotating gamma cameras has lessened some of the interest in the tomographic capabilities of the Pho/Con and other limited angle tomographic systems (for example the seven pinhole collimator or the slant-hole collimator). The demand for devices capable of performing reconstructions from projections has been recently stimulated by new camera technology capable of fulfilling some of the stringent requirements of  $\gamma$ -camera SPECT, namely linearity, uniformity and improved resolution.

Radionuclide tomographic systems can be classified according to the type of images which they produce. They can perform longitudinal tomography giving coronal sections in a plane parallel to the major axis of the body, or alternatively transverse tomography producing axial sections in a plane at right angle to the major axis of the body. With both these tomographic methods, one can have scanner based systems or gamma camera based systems. Table V lists common SPECT systems presently employed clinically in nuclear medicine.

The longitudinal tomographic systems include the Pho/Con multiplane imager and camera based systems employing special purpose collimators such as the seven pinhole and



TABLE V : Tomographic systems in nuclear medicine: A comparison

Tomographic Systems	Detect. type	max energy range (KeV)	clinical use	Func.nal Imaging	Spatial resolution (cm)		sensitivity	CPU needed	approx. cost \$
					coronal	axial			
Longitudinal Pho/Con Slant hole 7-Pinhole	scanner	551	WB	no	0.9-1.1 <sup>a</sup>	3.5 <sup>a</sup>	***	no	200K
	camera	200	C	yes	0.9-1.8 <sup>a</sup>	N/A <sup>a</sup>	**	yes	100K
	camera	200	C	yes	0.8-1.3 <sup>a</sup>	0.7-1.9 <sup>a</sup>	***	yes	100K
Transverse Cleon 7-Camera Positron	scanner	400	BF, H <sup>b</sup> , C	yes	2.0 <sup>f</sup>	1.7-1.9 <sup>g</sup>	***	yes	700K <sup>h</sup>
	camera	400	BF, H, C	yes	0.7-1.5 <sup>b</sup>	1.1-2.0 <sup>b</sup>	**	yes	200K <sup>i</sup>
	ring of detect.	551	BF, H, WB	yes	1.4 <sup>b</sup>	0.7-1.1 <sup>b</sup>	****	yes	600K <sup>i</sup>

H=Head imaging; BF=Body function; C=Cardiac imaging; WB=Whole body function  
 N/A=information not available; a) measured at the focal plane;  
 b) Jaszczak R.J. 1982; Larsson S.A. 1980; Jaszczak et al 1981.  
 c) Myers et al 1983; d) Le Free et al 1981;  
 e) Derenzo et al 1981; Ter-Pogossian M.M. 1981; f) Holman et al 1979  
 g) Cost without computer; h) Whole body scanner with computer  
 i) Head scanner with computer

rotating slant-hole collimators. Omitted from this group are the Fresnel zone plate and the time-coded multi-pinholes since these are largely experimental systems. Longitudinal tomographic devices reconstruct coronal images with data originating from a limited angle, thus using an incomplete set of angular samples. The limited angular range of the data makes the reconstruction sensitive to the object and systems geometry, noise in the signal and attenuation of photons in traversing the target organ and surrounding structures. In view of these limitations, systems which use a complete set of projections over the entire angular range are more advantageous in emission tomography. The advantage offered by these devices is that they eliminate the interference of surrounding tissue activity and thus avoid many of the problems associated with blur tomography. Of the transverse section imaging systems, the most widely used are the rotating gamma camera based systems. The added attraction of these latter devices is the ability of including, in the reconstruction, terms which will compensate for the following factors:

- a) gamma ray attenuation and scatter
- b) variability in the detector sensitivity
- c) system calibration and alignment
- d) patient motion and other physiological factors

Note that the above listed parameters also affect regular planar nuclear medicine which can be viewed as an extreme case of limited angular sampling with the planar image representing a single projection of the volume of activity.

Included in Table V are some of the operating characteristics for the listed tomographic systems as reported in the literature. The type of application of the given instrumentation reflects the most useful and common imaging procedure for which it is employed. The quantitation of the spatial resolution, divided into coronal and axial, is an attempt to identify the typical limiting values.

In the case of the sensitivity, a quantitative comparison was more difficult not only because of the variability in the experimental design, but more so because of the number of functional parameters employed, such as collimators, type of scintillators, signal handling etc. The qualitative classification employed in Table V ranges from poor(\*), average(\*\*), good(\*\*\*), and superior(\*\*\*\*). With respect to sensitivity, scanner type of SPECT systems have, in general, a higher sensitivity per reconstructed slice than equivalent camera based systems. However rotating gamma camera SPECT devices have an overall higher sensitivity since they are able to view the organ as a whole. Note that collection efficiency is dependent primarily on the detection solid angle which is roughly proportional to the size of the useful detector area. All the devices listed in Table V, with the exception of the

Pho/Con, require computer support to produce tomographic images. The cost shown in the final column refers only to the basic detection system.

From the tabulated data it appears that further developments in radionuclide tomography will most likely be oriented towards systems which perform transverse section imaging. The most useful are gamma camera based systems which can perform regular planar nuclear medicine imaging with the same instrumentation. The basic limitation in the use of positron imaging as a routine clinical investigation, is the accessibility of the required short lived positron emitters. This makes dual photon imaging practical only for those institutions able to produce the necessary radioisotopes on site.

For longitudinal section imaging devices, the main limitation associated with the reconstruction is the limited angular sampling. This results in an error propagation due to the forward and backward cross-talk by the image planes. The noise correlation between planes is caused by the activity in the surrounding tissue which is blurred throughout the reconstructed volume. The problem of blurring in limited angle emission tomography can in part be handled by resorting to some a-priori information such as the knowledge of the blur operator existing between planes, and knowledge of the geometry of the organ under investigation. For these reasons longitudinal section imaging systems are employed almost exclusively in very specialized imaging situations. As an example, cardiac

Imaging with the 7-pinhole uses advantageously a-priori information about the shape and orientation of the heart in order to reduce the interaction between the image planes. However, with such a system, the proper alignment of the detector with the heart major axis is essential in order to produce clinically significant images, since a slight misalignment, even of few degrees, can cause serious artifacts (Budinger T F 1980). For this reason this method has not been very successful. For the specific case of the Pho/Con, the deblurring of images has seen limited success with both analytical (Hooper et al 1979, Jenkins et al 1980) and iterative methods (Garcia et al 1981). The limitation in the size of the detector and consequent limitation in depth resolution alone, reduce the usefulness of this device and limit the type of application for which this system can be of clinical value. The Pho/Con is useful in the area of whole body imaging, particularly in the detection of highly localized radiotracers where it provides simultaneous anterior and posterior whole body views obtained under equivalent imaging conditions. The use of the Pho/Con is restricted to clinical investigations used, in conjunction with tumor seeking agents, to assess the extent of spread of malignancies. When applied to bone imaging the system can differentiate small, less active lesions from normal structures or it can enhance uptake visualization, helping to select the proper site for bone biopsy for example. In the detection of hot lesions the blurring caused by the surrounding structures is reduced considerably thus

providing for greater multiple depth information. The depth information is limited by the amount of correlated noise in the longitudinal planes. Images produced by the Pho/Con could be somewhat improved by upgrading some of the gamma camera physical characteristics and possibly by modifying the collimator specifications. These changes would improve the gamma camera performance in such areas as spatial and energy resolution thus increasing the system resolution and depth discrimination.

In analyzing the camera performance parameters, a number of changes could be suggested which would increase the intrinsic spatial resolution, energy resolution and the camera's linearity. To do this however, would be rather inappropriate since the new Pho/Con 192 model has altered the gamma camera to account for some of the limitations in the earlier model. The new camera configuration will be discussed briefly later. For now it is important to analyse the effect that the camera's lack of linearity and both spatial and energy resolution have on the overall system performance.

As demonstrated in Chapter 3, the spatial distortions of the gamma camera did not produce a noticeable effect on the system's linearity. That is, the spatial dimensions of pattern in phantom were not altered. This can be attributed to the fact that the crystal signal represents only a small portion of the overall position signal as indicated by the coordinate equations. However, the camera's non-linearity as observed, causes the displacement of events towards the

centre of the crystal. This will degrade the depth resolution and hence cause a reduction in the tomographic effect. As discussed above, the tomographic effect is produced by the quantities  $X_i(D/H)$  and  $Y_i(D/H)$  in the expression for the coronal images. Clearly for a fixed value of  $(D/H)$  a decrease in the value of  $(X_i, Y_i)$  due to camera non linearity will reduce the value of  $X_i(D/H)$  and  $Y_i(D/H)$ . By the same argument, the depth resolution of the system could be further increased by increasing the crystal size in the gamma camera.

The second parameter which needs to be improved, from the present 1.5 centimeters, is the camera's intrinsic spatial resolution. Current camera technology is now capable of intrinsic spatial resolutions which are approximately a third of that measured in our system. A three-fold reduction of the camera's intrinsic resolution should considerably improve the system's resolution. For example, at five centimeters distal from the collimator's geometrical focal point a 3-fold improvement of the intrinsic resolution could improve the Pho/Con resolution by approximately 8% from the present value; the improvement would be 10% for 5 centimeters proximal from the collimator focal point. According to the expression of  $R_o$  given in Chapter 3, at the focal depth the degradation of the system resolution due to the gamma camera's intrinsic resolution is negligible.

Improvement of the energy resolution from the present 17% at 140 KeV. is desirable. This would allow a greater

rejection of scattered events thus producing images with sharper detail.

With regard to collimator design, the changes should be directed at improving the depth resolution of the system. This can be done simply by increasing the size of the collimator to parallel the increase in size of the gamma camera. In addition one should look at the possibility of shielding the central portion of the collimator, and so altering the minimum value for the acceptance angle as demonstrated in Chapter 2.

One example of the improved depth discrimination which can be achieved by screening some of the central holes of the focussing collimator is shown in Figure 6.1. These curves represent the point source response, measured along the collimator axis using a Co-57 source for various minimal acceptance angles. The outer curve is the response measured without shielding followed by curves where the central hole and increasing number of hexagonal hole arrays have been shielded. Figure 6.2 shows the change in depth resolution versus the minimum acceptance angle. As shown in the graph the resolution is improved by 0.5 centimeters by reducing the minimum acceptance angle to 42 degrees. This corresponds to the shielding of the central hole together with 5 consecutive arrays of hexagonal holes. The improvement in the depth resolution however, is at the expense of counts, as indicated in the same Figure 6.2. In the example given, the loss is approximately 40%. This count loss can be partially recovered by improving the



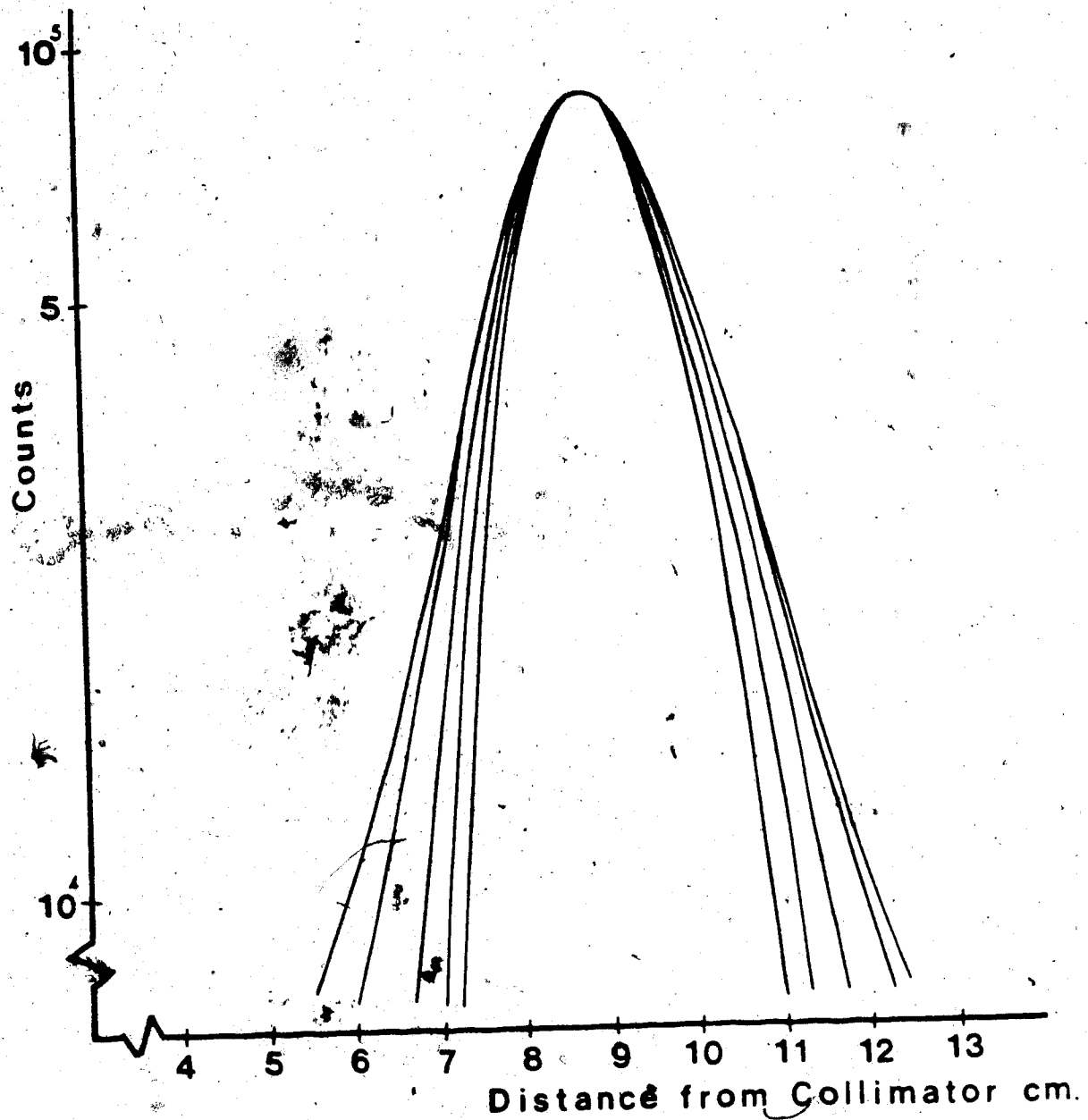


Fig. 6.1 Point source response as a function of distance from the collimator (380 KeV), measured with a minimum acceptance angle of  $0^\circ$ ,  $12.8^\circ$ ,  $27.8^\circ$ ,  $41.8^\circ$ ,  $54.6^\circ$  beginning with the outer curve.

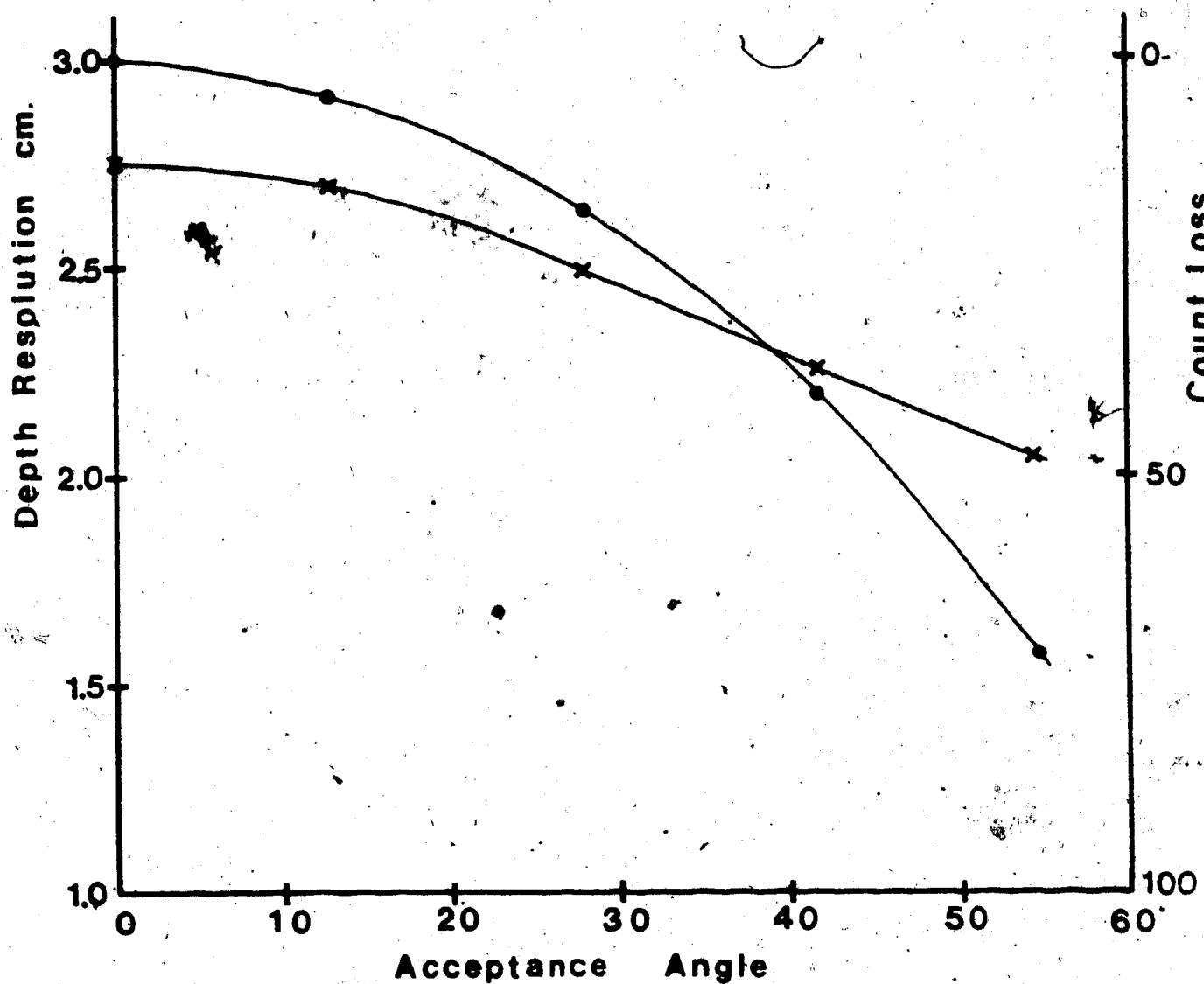


Fig. 6.2 Gain in the depth resolution obtained by confining the acceptance angle to a minimum of  $0^\circ$ ,  $17.8^\circ$ ,  $27.8^\circ$ ,  $41.8^\circ$ ,  $54.6^\circ$ . The same graph shows the loss of counts at the same angles.

camera energy resolution thus permitting use of a larger analyzer energy window (20-25%). Further counts can be regained by increasing the size of the detector. The improvement of the depth resolution using this method could cause artifacts in the reconstructed images. This however needs to be demonstrated. As stated earlier, the new and improved Pho/Con 192 has overcome some of the limitations of the old system's limitations. The intrinsic resolution and linearity of the gamma camera have been increased by increasing the number of PM tubes and reducing the photocathode diameter. The original 7 PM tubes with a diameter of 7.6 centimeters are changed in the new camera head which is now provided with 19 - 5.1 centimeter diameter phototubes. The increase in number of PM tubes coupled to a decrease in crystal thickness to 1.27 centimeters has improved the energy resolution from 17% to 14% for 140 KeV photon energy. This improvement is the result of the higher light collection efficiency in the new camera head. The size of the crystal was increased to 24 centimeters from the present 20 centimeters in diameter. With respect to the design of the collimators the only change made was to increase the geometric focal depth from 8.9 to 11.4 centimeters. This was done, it is assumed, to provide focal plane readout at greater depths in the subject.

Of more fundamental concern, however, is the overall function that the Pho/Con can play in a modern nuclear medicine department. In many respects its role has been

superseded since the onset of SPECT tomographic techniques employing rotating gamma cameras. Since the beginning of this study about the Pho/Con, emission tomography in nuclear medicine has made considerable technical advances alongside with the development of gamma camera SPECT systems. Because of this, SPECT systems employing gamma cameras have become the method of choice in emission tomography partly also for their ability to produce tomographic slices which are, in many respects, equivalent to transmission CT images. The progress made in gamma camera ECT has minimized the usefulness of the Pho/Con, limiting its use, almost exclusively, to whole body imaging procedures. This study has also shown some of the intrinsic limitations of the Pho/Con as a tomographic device, resulting from poor depth resolution and blur artifacts in the reconstructed images. It is anticipated that further developments in the limited angle reconstruction methods will only marginally remedy these fundamental limitations and an attempt at overcoming these limitations is worth-while, in view of the systems which are presently in operation. Even with marginal improvements in the resolution and the deblurring techniques, the future of the Pho/Con multiplane scanner appears to be marginal.

## 6.2 Deblurring algorithm: a critique

The deblurring algorithm presented in Chapter 4 has the advantage over other mathematical approaches in that it does not require the inversion of the blur function in order to recover the true activity distribution. It was anticipated that the use of iterative methods would reduce, in part, the problem of noise amplification which occurs in the inversion of the blur function. The preliminary results obtained in the deblurring of a noiseless computer simulated phantom were encouraging, since the algorithm appeared to be capable of removing the noise blur component from the outer planes which had no activity. In contrast to other deblurring techniques, noise is amplified by the convolution operation at each iteration. The propagation of noise is particularly pronounced for images with poor count statistics and in the presence of non-correlated noise. As stated earlier, the study of a simulated phantom with non-correlated noise is not a true representation of the way in which the Pho/Con propagates noise through the tomographic planes. The poisson noise associated with the measured scan data is projected throughout the tomographic planes in the reconstruction correlating the noise throughout the image planes as compared to non-correlated noise which is independent, from point to point, in all parts of the reconstructed volume. The deblurring of low count real phantom images, obtained by scanning a hot distributed source in a warm background, produces better results than

with simulated data. However, the problem of noise amplification still persists and methods of containing the propagation of noise should also be included in the algorithm. Smoothing in the final stage of the deblurring routine could provide a means to reduce the degradation in the image due to correlated noise. Smoothing, however, will likely produce a loss in resolution. Further investigation of the iterative deblurring technique should attempt to address the problem of noise propagation. The outcome will undoubtedly provide the final answer as to the true effectiveness of this deblurring method.

With the present technique the most critical decision one must make is the threshold cut off level in the initial estimate. Such thresholding could eliminate valid, needed information which it is not possible to recover with a simple multiplicative correction approach to deblurring. In the program, single isolated pixels with zero value, located within non zero regions in the image, are modified in the initial estimates.

In the development of the deblurring algorithm the variability of the system's point response function was ignored in order to simplify the computer implementation. More realistically one must include in the blur function dependence with depth. In the implementation, this could be achieved by storing a series of point images measured at increasing depths. In the blurring process each plane estimate would be matched to the appropriate blur function.

Quantitatively, to regain the initial activity

distribution, it would be necessary to include in the algorithm an attenuation compensation factor. A first order attenuation correction could be implemented using a dual energy window technique since the Pho/Con is provided with two analyzers for dual photopeak selection.

The present deblurring algorithm uses a FFT to perform the convolution. The time requirement for each iteration is approximately 5.6 minutes and total time of approximately 2 hours for the 20 iterations. It is possible that proper time optimization of the various programming stages could further reduce the time required for each iteration.

## REFERENCES

- Adams, R. and Zimmerman, D.: Methods for calculating the dead time of Anger camera systems. J. Nucl. Med. 14:496-498, (1973).
- Alavi, A., Reivich, M., Greenberg, J., et al: Mapping of functional activity in brain with 18F-fluoro-deoxyglucose. In Seminars in Nuclear Medicine Vol. XI:24, (1981).
- Alleman, R., Gresset, G., Vacher, J.: Potential advantages of cesium fluoride scintillators for a time of flight positron camera. J. Nucl. Med. 21:153, (1980).
- Andrew, E.R.: Nuclear Magnetic Resonance: Zeugmatography. In Medical Imaging. Edited by Kreef, L. and Steiner, R.E. pp. 38-43, (1979).
- Anger, H.O.: A new instrument for mapping gamma-ray emitters. Biology and Medicine Quarterly Report UCRL-3653, (1957).
- Anger, H.O.: Tomographic gamma-ray scanner with simultaneous readout of several planes. In Fundamental Problems in Scanning. Edited by Gottschalk, E. and Beck, R.N., pp. 195-211, (1968).
- Anger, H.O.: Multiplane tomographic gamma-scanner. In Medical Radioisotope Scintigraphy. I, IAEA, Vienna, pp. 203-216, (1969).
- Anger, H.O., Davis, D.H.: Gamma-ray detection efficiency and image resolution in sodium iodide. Rev. Sci. Instr. 35:693-697, (1964).
- Bading, J.R.: Positron emission computed tomography. An emerging method for the study of physiology in vivo. Applied Radiology/NM. 89-105 Feb. (1983).
- Barrett, H.H.: Fresnel zone plate imaging. J. Nucl. Med. 13:382-385, (1972).
- Barrett, H.H., DeMeester, G.O., et al: Tomographic imaging with Fresnel zone plate system. In Tomographic Imaging in Nuclear Medicine. Edited by Freedman, G.S.. Soc. Nuc. Med. Inc., New York, p. 106, (1973).
- Bates, R.H.T., Peters, T.M.: Towards improvements in tomography. N. Z. J. Sci. 14:883-896, (1971).
- Bec: Bay Engineering Company, San Francisco, CA.
- Beck, R.N.: Collimator of gamma rays. In Fundamental



Problems in Scanning. Edited by Gottschalk, A. and Beck, R.N., pp. 71-92, (1968).

Bender, M.A., Blau, M.: The clinical use of the auto-fluoroscope. J. Nucl. Med. 3:202, (1962).

Bevington, P.R.: Data reduction and error analysis for the physical sciences. McGraw-Hill, New York, pp. 204-246, (1969).

Bocage, E.M.: Patent no. 536,464, Paris, France, (1921). (Quoted from Brooks, R.A. and DiChifo, G., Phys. Med. Biol. Vol. 21, No. 5:689-632, (1976).

Bowley, A.R., Taylor, C.G., Causer, D.A., et al: A radioisotope scanner for rectilinear, arc, transverse section and longitudinal section scanning. Br. J. Radiol. 46:262-271, (1973).

Boyd, D.P., Couch, J.L., Napel, S.A., et al: Highspeed, multislice, x-ray computed tomography. In Proceedings of International Workshop on Physics and Engineering in Medical Imaging. IEEE Comp. Soc. pp.139-150, (1982).

Bracewell, R.N.: The Fourier transform and its application. McGraw-Hill, New York, 1965.

Bracewell, R.N., Riddle A.C.: Inversion of fan-beam scans in radio astronomy. Astrophys. J. 150:427-434, (1967).

Bragg, D.G., Durney, C.H., Johnson, C.C., et al: Monitoring and diagnosis of pulmonary edema by microwave: a preliminary report. Invest. Radiol. 12:289-291, (1977).

Budinger, T.F.: Instrumentation trends in nuclear medicine. In Seminars in Nuclear Medicine. 7:285-297, (1977).

Budinger, T.F.: Physical attributes of single-photon tomography. J. Nucl. Med. 21:579-592, (1980).

Budinger, T.F.: Single photon emission tomography, Nucl. Med. Biol., Procc. Third World Congress, Paris, pp. 1159-1177, (1982).

Budinger, T.F., Derenzo, S.E., Huesman, R.H. and Cahoon, J.L.: Medical criteria for the design of a dynamic positron tomography for heart studies. IEEE TRANS. Nucl. Sci. NS-29:488, (1982).

Budinger, T.F., Gullberg, G.T., McRae, J. et al: Isotope distribution reconstruction from multiple gamma camera views. J. Nucl. Med. 15:480, (1974).

Byrom E.; Pavel D.G., Swiryn S., et al : Phase image gated

cardiac studies: a standard evaluation procedure. In Functional Mapping of Organ System and other computer topics. Edited by Esser P.D. pp.129-138,(1981)

Cassen, B., and Curtis, L.: The in vivo delineation of thyroid glands with an automatically scanning record. UCLA Report No. 130,(1951).

Chang, W., Lin, S.L., Henkin R.E.: A rotatable quadrant slant hole collimator for tomography (QSH): a stationary scintillation camera based SPECT system. In Single Photon Emission Computed Tomography and Other Selected Computer Topics. Edited by Sorenson, J.A., Society of Nuclear Medicine, New York, pp. 81-94, (1980).

Chang, W., Lin, S.L., Henkin, R.E.: N-Spot focal plane tomography in cardiac imaging. In Functional Mapping of Organ Systems and other computer topics. Edited by Esser, P.D. pp. 185-196,(1981).

Chiewitz, O., Hevesy, G.: Radioactive indicators in the study of Phosphorus metabolism in rats. Nature 136:754, (1935).

Cho, Z.H., Chan, J.K., Eriksson L.: Circular ring transverse axial positron camera for 3-dimensional reconstruction of radionuclides distribution. IEEE Trans. Nucl. Sci. NS-23:613-622,(1976).

Cho, Z.H., Farukhi, M.R.: New bismuth germanate scintillation crystal-A potential detector for the positron camera application. J. Nucl. Med. 18:840,(1977).

Chu, D. and Tam, K.: Three-dimensional imaging in the positron camera using Fourier techniques. Phys. Med. Biol. 22:245-265,(1977).

Chu, D., Tam, K., Perez-Mendez, V., et al: High efficiency gamma converters and their application in an MWPC positron camera. In Medical Radionuclide Imaging AIEA Vienna, Vol 1 pp. 171-193,(1977).

Cormack, A.M.: Representation of a function by its line integrals, with some radiological application, I. J. Applied Physics 34:2722-2727, (1963).

Cormack, A.M.: Representation of a function by its line integrals, with some radiological application, II. J. Applied Physics 35:2908-2913, (1964).

Cronin, M.P.: Microwave thermography. Appl. Radiol. 6:139, (1977).

Damadian, R.: Tumor detection by nuclear magnetic resonance.

Science 171:1151,(1971).

Derenzo, S.E., Budinger, T.F., Huesman, R.H., Cahoon, J.L., et al: Imaging properties of a positron tomograph with BGO crystals. IEEE Trans. Nucl. Sci. NS-28:81-89, (1981).

Freedman, G.: Tomography with gamma camera. J. Nucl. Med. 11:602-606,(1970).

Garcia, E.V., Aréda, J., Chapman, D., et al: Tomographic blur compensation algorithms for the Pho/Con 192 Scanner. J. Nucl. Med. 22:62,(1981).

Garcia, E.V., Diaz, J., Chapman, D., et al: Single photon emission computed body tomography using a multi-plane scanner. IEEE Trans. Nucl. Sci. NS-27:425-429, (1980).

Glasser, O.: Wilhelm Conrad Rontgen and the Early History of the Roentgen Rays. Springfield, Ill., Thomas,(1934).

Goitein, M.: Three-dimensional density reconstruction from a series of two-dimensional projections. Nucl. Inst. Meth. 101:509-518,(1972).

Goldstein, R.A., Klein, M.S., Welch, M.J., et al: External assessment of myocardial metabolism with G-11 palmitate in vivo. J. Nucl. Med. 21:342,(1980).

Graham, L.S., Perez-Mendez, V.: Special imaging devices. In Nuclear Medicine Physics, Instrumentation, and Agents. Edited by Rollo F.D. pp 271-321,(1977).

Hattner, R.S., Lim, C.B., Swann, S.J., et al: Cerebral imaging using Ga-68 DTPA and the U.C.S.F. multiwire proportional chamber positron camera. IEEE Trans. Nucl. Sci. NS-23:523-527,(1976).

Herschel, J.F.W.: On chemical action of rays of solar spectrum on preparation of silver and other substances both metallic and non-metallic on some photographic processes. Philos. Trans. R. Soc. London 130:1, (1840). (Quoted from Freundlich I.M.: Medical aspect of thermography. In Imaging For Medicine, Vol.1. Edited by Nudelman, S. and Patton, D.D., Plenum Press, New York,(1980).

Hevesy, G.: Radioactive indicators. Interscience, New York, (1948).

Hine, G.J., Paras, P. and Warr, C.P.: Measurements of the performance parameters of gamma cameras: Part 1. U.S. Department of Health, Education and Welfare. Public Health Service, Food and Drug Administration,

(1978).

- Hoffman, E.J., Phelps, M.E., Mullani, N.A., et al: Design and performance characteristics of a whole-body positron transaxial tomograph. J. Nucl. Med. 17:493-622, (1976).
- Hoffman, E.J., Phelps, M.E., Huang, S.C., et al: A new tomograph for quantitative positron emission computed tomography of the brain. IEEE Trans. Nucl. Sci. NS-28:99, (1981).
- Hoffman, E.J., Phelps, M.E., Weiss, E.S., et al: Transaxial tomographic imaging of canine myocardium with  $^{14}\text{C}$ -palmitic acid. J. Nucl. Med. 18:57, (1977).
- Holman, B.L., Hill, T.C., Wynne, J. et al: Single-photon transaxial emission computed tomography of the heart in normal subjects and in patients with infarction. J. Nucl. Med. 20:736-740, (1979).
- Hooper, H.R., Scrimger, J.W., Lentle, B.C.: Correction for out-of-focal plane blurring in a simulated multiplane tomographic scanner. J. Nucl. Med. 20:1194-1196, (1979).
- Hooper, H.R.: TOMDIS user's manual for the display of three dimensional images. Departement of Nuclear Medicine Cross Cancer Institute, Edmonton, Alberta, Canada.
- Huang H.K. and Ledley R.S.: Scanning methods and reconstruction algorithms for computerized tomography. In Medical Imaging Technique. Edited by Preston K.Jr., Taylor K.J.W., Johnson S.A., Ayers W.R. pp.313-327, (1979).
- James, A.E., Jr., Fleischer, A.C., Jones, T., et al: Ultrasound: certain considerations of equipment usage. In The Physical Basis of Medical Imaging. Edited by Coulam, C.M., Erickson, J.J., Rollo, F.D., James A.E.Jr. Appleton-Century-Crafts, New York, p. 169, (1981).
- Jaszczak, R.J., Chang, L.T., Stern, N.A., et al: Whole-body single-photon emission computed tomography using dual, large-field-of-view scintillation cameras. Phys. Med. Biol. 24:1123-1143, (1979).
- Jaszczak, R.J., Huard, D., Murphy, P. et al: Radionuclide emission computer tomography with a scintillation camera. J. Nucl. Med. 17:551, (1976).
- Jaszczak, R.J., Murphy, P., Huard, D., et al: Radionuclide emission computed tomography of the head with  $^{99\text{m}}\text{Tc}$  and  $^{137}\text{Cs}$  scintillation camera. J. Nucl. Med. 18:373-

-380,(1977).

- Jaszczak, R.J., Coleman, R.E., Whitehead, F.R.: Physical factors affecting quantitative measurements using camera-based single photon emission computed tomography (SPECT). IEEE Trans. Nucl. Sci. NS-28:69-80,(1981).
- Jaszczak, R.J.: Physical characteristics of SPECT systems. J. Comput. Assist. Tomog. 6:1205-1215, (1982).
- Johns, H.E. and Cunningham, J.J.: The Physics of Radiology. Charles C. Thomas 5
- Kaufman, L., Ewins, J., Rowan, W., et al: Semi-conductor gamma cameras in nuclear medicine. IEEE Trans. Nucl. Sci. NS-27:1073-1079,(1980).
- Kaufman, L., Shosa, D., Crooks, L., et al: Technology need in medical imaging. IEEE Trans. on Med. Imag. 2:11, (1982).
- Kereiakes, J.G., Thomas, S.R., Michael, J.G., et al: Dose evaluation in nuclear medicine. In Biological Risks of Medical Irradiation. Edited by Fullerton, G.D., Koop, D.T., Waggener, R.G., Webster, E.W. p. 125, (1980).
- Kereiakes, J.G., Thomas, S.R., Saenger, E.L.: Methods of risk reduction in nuclear medicine. In Biological Risks of Medical Irradiation. Edited by Fullerton, G.D., Koop, D.T., Waggener, R.G., Webster, E.W. p. 125, (1980).
- Keyes, J.W., Orlandea, N., Heetderks, W.J., et al: The humongotron-a scintillation camera transaxial tomograph. J. Nucl. Med. 18:381-387,(1977).
- Keyes, W.I.: A practical approach to transverse-section gamma-ray imaging. Br. J. Radiol. 49:62,(1976).
- King, M.A., Doherty P.W.: Color coded ejection fraction images for following regional function throughout the cardiac cycle: In Functional Mapping of Organ System and other computer topics. Edited by Esser P.D. pp.119-128,(1981).
- Kirch, D.L., Vogel, R.A., LeFree, M.T., et al: An Anger camera/computer system for myocardial perfusion tomography using a seven pinhole collimator. IEEE Trans. Nucl. Sci. NS-27:412-420, (1980).
- Knust, E.J., Kupfernagel, C.L., Stocklin, G.: Long Chain F-18 fatty acids for the study of regional metabolism in heart and liver. J. Nucl. Med. 20:1170,(1979).

- Kuhl, D.E., and Edwards, R.Q.: Image separation radioisotope scanning. *Radiology* 80:653-661, (1963).
- Kuhl, D.E., Edwards, R.Q., Ricci, A.R., et al: The Mark IV system for radionuclide computed tomography of the brain. *Radiology* 121:405-413, (1976).
- Larsen, L.E., Jacobi, J.H.: The use of orthogonal polarizations in microwave imagery of isolated canine kidney. *IEEE Trans. Nucl. Sci. NS-27:1184-1191*, (1980).
- Larsson, S.A.: Gamma camera emission tomography. *Acta Radiologica Supplement* 363, (1980).
- Lauterbur, P.C.: Image formation by induced local interactions: Example of employing nuclear magnetic resonance. *Nature (London)* 242:190, (1973).
- Lawson, R.N.: Implications of surface temperature the diagnosis of breast cancer. *Can. Med. Ass.* 75:309, (1956).
- Lédley, R.S.: Computerized transaxial x-ray tomography of the human body. *Science* 186:207-212, (1974).
- LeFree, M.T., Vogel, R.A., Kirch, D.L., et al: Seven-pin-hole tomography-a technical description. *J. Nucl. Med.* 22:48-54, (1981).
- Lenzi, G.S., Jones, T., McKenzie, C.G. et al.: Study of regional cerebral metabolism and blood flow relationships in man using the method of continuously inhaling oxygen-15 and oxygen-15 labelled carbon dioxide. *J. Neurol. Neurosurg. Psychiatry* 41:1, (1978).
- Lim, C.B., Chu, D., Kaufman, L. et al: Initial characterization of a multi-wire proportional chamber positron camera. *IEEE Trans. Nucl. Sci. NS-22:388-394*, (1975).
- Lin, S.L., Chang, W., Henkin, R.E.: Reduction of off-plane activities in slant hole tomography. In *Functional Mapping of Organ Systems and other computer topics*. Edited by Esser, P.D., pp. 197-204, (1981).
- Muehllehner, G.: Rotating collimator tomography. *J. Nucl. Med.* 11:347, (1970).
- Muehllehner, G.: A tomographic scintillation camera. *Phys. Med. Biol.* 16:87-96, (1971).
- Muehllehner, G.: Positron camera with extended counting plate capability. *J. Nucl. Med.* 16:653-657, (1975).

- Mullani, N.A., Ficke, D.C., Ter-Pogossian, M.M.: Cesium fluoride: A new detector for positron emission tomography. IEEE Trans. Nucl. Sci. NS-27:572, (1980).
- Myers, M.J., Busemann, S.E., De Bakker, J.: A comparison of rotating slant hole collimator and rotating camera for single photon emission tomography of the heart. Phys. Med. Biol. 28:581-588, (1983).
- Myers, W.G. and Wagner, H.N., Jr.: How it Began. In Nuclear Medicine. Edited by Wagner, H.N., Jr. pp. 3-14, (1975).
- Oldendorf, W.H.: Isolated flying spot detection of radio-density discontinuities displaying the internal structural pattern of a complex object. IRE Trans. Biomed. Elect. BME 8:68-72, (1961).
- Partain, C.L., Price, R.R., Erickson, J.J., et al: Nuclear magnetic resonance imaging. In The Physical Basis of Medical Imaging. Edited by Coulam, C.M., Erickson, J.J., Rollo, F.D., James, A.E., Jr., pp. 243-251, (1981).
- Partain, C.L., Price, R.R., Patton, J.A., et al: Nuclear magnetic resonance (NMR) imaging: physical principle and clinical potential. In Nucl. Med. Biol. Proc. 3rd World Congress, Paris, (1982).
- Phelps, M.E.: Positron computer tomography studies of cerebral glucose metabolism in Man: Theory and application in nuclear medicine. In Seminars in Nuclear Medicine, Vol. XI:32, (1981).
- Phelps, M.E., Hoffman, E.J., Mullani, N.A. et al: Application of annihilation coincidence detection to transaxial reconstruction tomography. J. Nucl. Med. 16:210-224, (1975).
- Pickens, D.R., Price, R.R., Patton, J.J., et al: Focal-plane tomography image reconstruction. IEEE Trans. Nucl. Sci. NS-27:489-492, (1980).
- Pickens, D.R., Price, R.R., Patton, J.J., et al: Transverse image reconstruction in Tl-201 myocardial scans. IEEE Trans. Nucl. Sci. NS-28:57-59, (1981).
- Popovic, S. and Mallard, J.R.: The longitudinal and lateral response of multichannel focussing collimators. Int. J. Appl. Rad. Isotopes 19:303-312, (1968).
- Ramachandran, G.N., Lakshminarayanan, A.V.: Three-dimensional reconstruction from radiographs and electron micrographs: Application of convolutions instead of Fourier

- transforms. Proc. Nat. Acad. Sci. 9:2236-2240, (1971).
- Rao, P.S., Sontosh, K., Gregg, E.C.: Computed tomography with microwaves. Radiology Vol. 135:769-770, (1980).
- Robertson, J.S.: Radiation absorbed dose calculations in diagnostic nuclear medicine. Int. J. Appl. Radiat. Isot. 33:981-990, (1982)
- Rogers, W.L., Han, K.S., Jones, L.W., et al: Application of a fresnel zone plate to gamma-ray imaging. J. Nucl. Med. 13:612-615, (1972).
- Rollo, F.D., Patton, J.A.: Nuclear medicine imaging devices. In The Physical Basis of Medical Imaging. Edited by Coulon, C.M., Erickson, J.J., Rollo, F.D., and James, A.E.. Appleton-Century-Crafts, New York, pp. 231-241, (1981).
- Rose, A.: Vision Human and Electronic. Plenum Press, New York, (1973).
- Sagel, S.: Early clinical experience with motionless whole-body computed tomography. J. Radiology 119:321-330, (1976).
- Searle Radiographics Inc. Pho/Con Service Manual.
- Shepp L.A., Logan B.F.: The Fourier reconstruction of a head section. IEEE Trans. Nucl. Sci, NS-21:21, (1974)
- Shosa, D. and Kaufman, L.: Methods of evaluation of diagnostic imaging instrumentation. Phys. Med. Biol. 26:101, (1981).
- Siemens Gammasonics, Inc.: Pho/Gamma ZLC-TM/37 Standard camera series 754.
- Siemens Gammasonic, Inc.: Pho/Con Multiplane Imager Service Manual. Section 5.
- Simpson, R.G. and Barrett, H.H.: Coded aperture imaging. In Imaging For Medicine. Edited by Nudelman, S. and Patton, D.D.. Plenum Press, 217-311, (1980).
- Stoddart, H.F. and Stoddart, H.A.: A new development in single gamma transaxial tomography Union Carbide focussed collimator scanner. IEEE Trans. Nucl. Sci. NS-26: 2710, (1979).
- Standard Publ. No. NUI-1980. Performance measurements of scintillation cameras. National Electrical Manufacturers Association, Washington, D.C. (1980).
- Tam, K.C., Chu, G., Perez-Mendez, V., et al :Three-dimensional



- reconstruction in planar positron cameras using Fourier deconvolution of generalized tomograms. IEEE Trans. Nucl. Sci. NS-25:152-159, (1978).
- Tam, K.C., Perez-Mendez, V., Macdonald, B.: 3-D object reconstruction in emission and transmission tomography with limited angular input. IEEE Trans. Nucl. Sci. NS-26:2797-2805, (1979).
- Tam, K.C., Perez-Mendez, V., Macdonald, B.: Limited 3-D reconstructions from continuous and pinhole projections. IEEE Trans. Nucl. Sci. NS-27:445-458, (1980).
- Tam, K.C., Perez-Mendez, V.: Limits to image reconstruction from restricted angular input. IEEE Trans. Nucl. Sci. NS-28:179-183, (1981).
- Ter-Pogossian, M.M., Mullani, N.A., Ficke, D.C., et al: Photon time-of-flight assisted positron emission tomography. J. Compt. Asst. Tomog. 5:2227, (1981).
- Ter-Pogossian M.M.: Special characteristics and potential for dynamic function studies with PET. Seminars in Nuclear Medicine Vol XI pp 13-23, (1981).
- Thompson, C.J., Yamamoto, Y.L., Meyer, E.: Positome II. A high efficiency positron imaging device for dynamic brain studies. IEEE Trans. Nucl. Sci. NS-26:584, (1979).
- Townsend, D., Piney, C., Jeavons, A.: Object reconstruction from focussed positron tomograph. Phys. Med. Biol. 23:235-244, (1978).
- Townsend, D., Schorr, B., Jeavons, A.: Three-dimensional image reconstruction for a positron camera with limited angular acceptance. IEEE Trans. Nucl. Sci. NS-27:463-470, (1980).
- Turner, D.A., Ramachandran P.C., Ali, A.A., et al: Brain scanning with the Anger multiplane tomographic scanner as a primary examination. Radiology 121: 125-129, (1976).
- Vogel, R.A., Kirch, D., LeFree, M., et al: A new method of multiplanar emission tomography using a seven pinhole collimator and an Anger scintillation camera. J. Nucl. Med. 19:648, (1978).
- Volpe, J.A., McRae J., Anger, H.O.: Clinical experience with the multiplane tomographic scanner. J. Nucl. Med. 21:101-106, (1971).
- Wild, J.J.: The use of ultrasonic pulses for the measurement of biologic tissues and the detection of time

density changes. *Surgery* 27:183,(1950).

Winchell, H.S., Sanchez, P.D., Watanabe, C.K., et al:  
Visualization of tumor in humans using Ga-67 citrate  
and the Anger whole body scanner, scintillation  
camera and tomographic scanner. *J. Nucl. Med.*  
11:459-465,(1970).

Wood, E.H., Kinsey, J.H., Robb, R.A. et al: Application of  
high temporal resolution, computerized tomography  
to physiology and medicine: In *Topics in Applied  
Physics*. Edited by Herman, G.T. Vol 32 pp.247-279,  
(1979).

Wunderlich, C.A.: Das Verhalten der Eigenwärme in Krankheiten  
(Quoted from Van Der Star, P.: The history of thermo-  
metry in medicine. In *Medical Thermography*. Edited  
by Heerma Van Vos, S.F.C. and Leiden, P.T., pp. 1-21,  
(1969).)